THE EUROTROCHILUS MECHANICUS

A ROBOTIC HUMMINGBIRD DRIVEN BY A RESONANT FLAPPING MECHANISM

Frederik LEYS

Supervisor:

Prof. D. Vandepitte

Co-Supervisor:

Prof. D. Reynaerts

Members of the Examination Committee:

Prof. J. Swevers

Prof. R. Puers

Prof. G. Dimitriadis

Prof. M.R. Vetrano

Dissertation presented in partial fulfilment of the requirements for the degree of Doctor of Engineering

March 2017

Uitgegeven in eigen beheer, LEYS FREDERIK, LEUVEN

PREFACE

…+ acknowledgements

ABSTRACT

The use of drones, or unmanned aerial vehicles (UAVs), is increasing every day. Although they were originally developed mainly for military purposes, commercial and personal applications start to emerge as they become smaller and more affordable.

Micro air vehicles (MAVs) are UAVs with limited size and weight; often designed for indoor use. Most of them use propellers as they can take off vertically and operate at low speeds or even hover. At small scales, MAVs propelled by flapping wings are a promising alternative as they could be able to mimic the exceptional flight capabilities of hummingbirds and insects.

The objective of this PhD. is to develop a robotic hummingbird; A tail-less flapping wing MAV that flies by flapping its wings and looks just like a hummingbird. To drive the wing motion a resonant flapping mechanism has been developed. To minimize the power consumption of this flapping mechanism, spring elements are added and the mechanism is tuned such that its damped resonance frequency is close to the desired flapping frequency.

The resonant flapping mechanism is able to generate asymmetric wing motions necessary for flight stabilization and steering. Because the robotic hummingbird is not passively stable a custom made on-board flight controller is designed and implemented that actively stabilizes flight. The flight controller consists of a wireless transceiver, motor drivers, motion sensors, encoders and a micro controller that contains the control algorithm.

The robotic hummingbird presented in this text is able to perform stable flight. The longest flight recorded so far lasted for 55 seconds.

In the framework of this research PIV (Particle Image Velocimetry) measurements are performed to study the flow and the aerodynamic phenomena around artificial hummingbird-like flapping wings. Also a parameter study is done to study the average thrust generated by a flapping wing and the power consumption of the flapping mechanism that drives the wing motion for a broad range of flapping frequencies, stroke amplitudes, angle of attacks and wing sizes.

GLOSSARY

List of abbreviations

aoa	angle of attack
COTS	Commercial-Off-The-Shelf
DARPA	Defense Advanced Research Projects Agency
DC	Direct Current
DEHS	Di-Ethyl-Hexyl-Sebacat
ETF	Eulerian Time Filtering
EMF	ElectroMotive Force
FMAV	Flapping wing Micro Aerial Vehicle
LED	Light Emitting Diode
LEV	Leading Edge Vortex
LiPo	Lithium Polymer (battery)
MEMS	Micro ElectroMechanical System
MCU	MicroController Unit
PCB	printed circuit board
PID	Proportional Integral Derivative
PIV	Particle Image Velocimetry
TEV	Trailing Edge Vortex
TR-PIV	Time-Resolved Particle Image Velocimetry
UAV	Unmanned Aerial Vehicle
µC	microcontroller

List of symbols

S	Wingspan
L	Wing length
m	Mass
A	Stroke Amplitude or Current
Ω	Stroke Amplitude
f	Flapping Frequency
AR	Aspect Ratio
C_{av}	Mean geometric chord
T	Flight Endurance
#C	Number of Components

P	Power
ϕ	Stroke Angle
θ	Stroke Angle
α	Angle of Attack
α'	Inclination Angle
β, δ	Deviation Angle
ϕ_0, ϕ	Mean Stroke Angle
α_0	Inclination Offset,
α_m	Geometric angle of attack at mid-stroke
φ_α , ζ	Phase shift between the stroke motion and the wing rotation
A_{max}	Stroke Amplitude under maximum load conditions
f_{max}	Flapping Frequency under maximum load conditions
m_{max}	Maximum Weight that can be lifted including self-weight
k_α	defines the shape of the inclination angle function
Ψ	Phase angle
T	Average Thrust
I	Inertia
U	Voltage
k	Spring Constant
D	Spring Diameter
d	Wire diameter of spring
τ	Amplitude of the driving torque
P_{av}	Average electric power
ω	Angular Velocity
c	Total Damping Coefficient
τ_R, τ_R, τ_R	Roll Torque, Pitch Torque, Yaw Torque
β_R, β_P, β_Y	Roll Angle, Pitch Angle, Yaw Angle
AD_L	Desired amplitude for the stroke of the left wing
A_L	stroke amplitude of the left wing

Contents

1 INTRODUCTION

1.1 AIM

The aim of this research is to develop a robotic hummingbird, a drone that flies by flapping its wings and looks just like a real hummingbird. The most recent prototype of the robotic hummingbird is described in the final chapter and is given the name 'Kulibrie' after the Dutch word for hummingbird 'Kolibrie' and the its alma mater, the KU Leuven.

It was pure academic curiosity that initially motivated us to develop a robotic hummingbird: would it be possible to make a robotic hummingbird? Like the mesmerizing robots often described in science fiction novels like *Changeling* **[Zelazny, 1980]** or described in fantasy books like the *Snitch* (Fig. 1B) in *Harry Potter* **[Rowling, 1997]** one that flies by flapping its wings and flies as swiftly and beautiful as a real hummingbird (Fig. 1)?

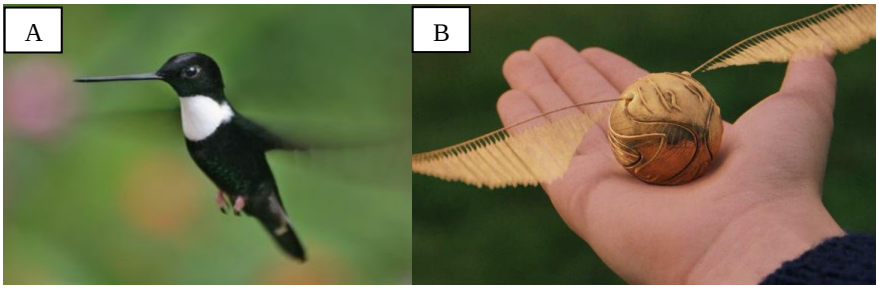

Fig. 1 Flapping wing inspiration: (A) Collared Inca Hummingbird **[Boniecki, 2017]** and (B) the Snitch from Harry Potter [Snitch, 2017]

Drones that fly by flapping their wings offer some practical advantages compared to rotor or fixed wing aircrafts that make it even more interesting to study them. These advantages are described in 1.3.2.

The reciprocating nature of the typical flapping wing motion of a hummingbird motivated us to study the possibility of using a tuned resonant flapping mechanism in order to improve its performance. Such a flapping mechanism elastically stores the kinematic energy at the end of each wing stroke so it can be used to accelerate the wing at the start of the next wing stroke.

In 2010, at the start of this research, no robotic hummingbird had yet been developed and the state of art was still far from a working prototype. This is no surprise taking in to account the challenging nature of developing a robotic hummingbird.

But after some innovations in MEMS sensors, electronics and material science a window of opportunity opened. The first robotic hummingbird, the *Nano Hummingbird* **[Keennon et al, 2012]** was presented in 2012. Since then other prototypes are developed in the framework of academic research, but the Nano Hummingbird is still the only one able to fly fully stable and controlled.

1.2 DRONES

1.2.1 HISTORY AND THE ONGOING TREND OF MINIMIZATION

Drones or unmanned aerial vehicles (UAV) are aircraft without an on-board pilot. They can be either autonomous or piloted remotely. Drones with a wingspan of several meters have been in uses since the previous century for military use (Fig. 2).

Fig. 2 Military drone, The RQ-1 PREDATOR with a wingspan of 16m [Predator, 2017]

Since then an ongoing trend of minimization has taken place, with much smaller drones as a result. Now, only 20 years later, portable drones are readily available and in widespread use for commercial and personal applications (Fig. 3) They are used in many applications: aerial photography, filming sport events, delivering packages, military operations and also for the mere joy of flying them.

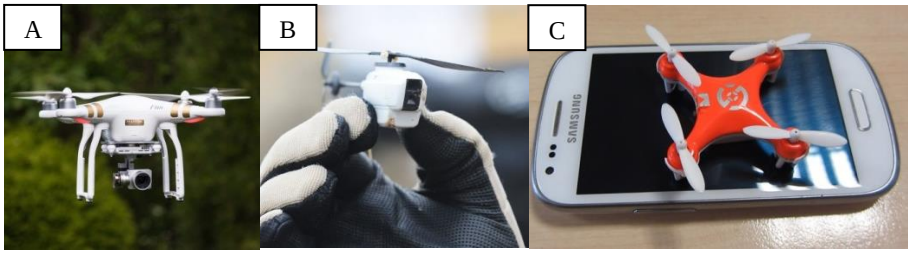

Fig. 3 Applications of Micro Air Vehicles: (A) a camera drone [Phantom, 2017], (B) a military surveillance drone **[Black Hornet, 2017]** and (C) a toy quad copter [Kii, 2017]

1.2.2 TYPES

The best known type of commercial and personal drones is the multi-copter and in particular the quadcopter that uses four rotors to fly (Fig. 3A & C). Besides rotor based drones, also fixed wing drones exist. These are more efficient for long range flights, but they lack the manoeuvring possibilities of rotor based drones and lack the ability to take-off vertically.

1.2.3 CRITERIA

Many criteria are important to evaluate the best drone for a certain application. Here we discuss only two of them that will be important for the comparison of flapping wing drones with rotor based drones and fixed wing drones.

The flight envelope and the manoeuvrability

The flight envelope of a drone is used to describe the cruise conditions and the set of distinct manoeuvers a drone can perform **[Lok et al, 2015]**. The more freedoms of motion that can be controlled independently during flight, the larger the flight envelope of a drone. The manoeuvrability is defined here as the speed with which flight manoeuvres can be performed.

A large flight envelope and a high manoeuvrability are advantages for drones that need to swiftly perform complex flight manoeuvres. For example drones that are used for indoor applications or drones that need to dodge fast moving obstacles.

The performance and flight time

The performance of a drone is defined here as the ratio of the thrust its propulsion system can generate to the power it needs to generate this thrust. The better the performance of a drone, the longer its flight time for the same battery.

1.3 FLAPPING WINGS

1.3.1 INSPIRED BY NATURE

Over 1000000 species of flying animals exist. Ranging from the smallest, a parasitic wasp, the *Dicopomorpha echmepterygis* (Fig. 4A) to the wandering albatross (*Diomedea exulans* Fig. 4B) the flying animal with the largest wing span that exist (on earth) **[Robertson, 2003].**

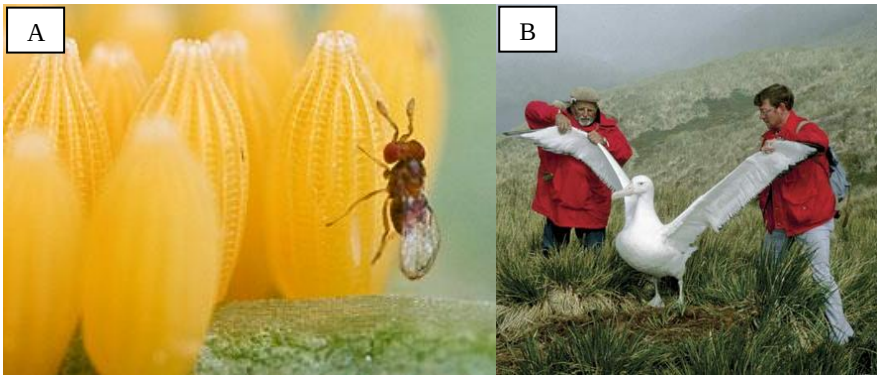

Fig. 4 Smallest and largest flying animal: (A) the smallest flying animal, a parasitic wasp, the Dicopomorpha echmepterygis [Wasp, 2017]. (B) The flying animal with the largest wingspan that exist, the wandering albatross **[Kaehler, 2017]**

Although they all share the same ability to fly, they can differ significantly in size, number of wings, wing motion, flight behaviour and many more characteristics. Two main types of biological flyers can be distinguished: the bird-like flying animals and the insect-like flying animals.

Bird-like flying animals, like most birds, but also bats, are relatively large and flap their wings, relatively slowly, up and down in order to generate enough forward thrust. It are the wing shape and the inclination of the wing relatively to the oncoming flow that result in an upwards force, much like conventional aircraft. They flex their wings inward during upstroke.

Insect-like flying animals, like most insects, but also hummingbirds, are relatively small and flap their wings relatively quickly horizontally (backwards and forwards) in order to generate enough upward thrust, in this sense their flight behaviour is more like conventional helicopters, because they can take-off vertically, without the need for a forward velocity. They do not flex their wings during flight.

Why we chose the hummingbird as an example

We took the hummingbird as an example for the flapping wing drone that is developed in the framework of this PhD because of its size and its flight abilities.
They are small enough to allow a performant insect-like flapping wing motion. But they are still large enough to mechanically mimic with the current state of technology in mind.
Furthermore they are the living proof of the large flight envelope and high manoeuvrability achievable by using flapping wings that allow them to swiftly perform amazing flight manoeuvres.

1.3.2 ADVANTAGES AND DISADVANTAGES

More thrust at insect scale
Four peculiar aerodynamic phenomena (chapter 3) enhance the thrust generated by small insect-like flapping wings. Without them, insects would not be able to fly. As a consequence, an insect-sized drone with flapping wings could carry a larger payload (battery, sensors…) than one with propellers.
At hummingbird-like scale however flapping wings generate considerably less thrust than propellers of the same size as will be shown in chapter three.

Better performance
The performance, defined as the thrust to power ratio, of a hummingbird-sized flapping wing is better than the performance of a propeller of the same size, as will be shown in chapter 4. Although the thrust generated by a hummingbird-sized flapping wing is just a fraction of the thrust generated by a propeller of the same size, its performance is still better because considerably less power is required to drive the flapping wing motion as long as a proper flapping mechanism is used as the one described in chapter 4.

Better manoeuvrability
A symmetric flapping wing does not generate a resultant gyroscopic effect as a fast rotating propeller does. The absence of a resulting gyroscopic effect makes it easier to swiftly perform flight manoeuvres that would otherwise have to overcome the gyroscopic effect

A robotic hummingbird does not need a tail for flight stabilisation and control as fixed wing drones do. Stability and control can be achieved with an asymmetric wing motion as will be discussed in chapter 5. The absence of a tail makes it easier to swiftly perform flight manoeuvres that would otherwise have to overcome the aerodynamic drag of the tail.

Less noise
The average wing tip speed of a flapping wing is considerably lower than the one of a rotating wing of the same size that generates the same amount of thrust. This gives a reason to believe that the noise made by a drone can be reduced by using flapping wings.

Stealth
One of the mean reasons for DARPA **[Darpa, 2017]** to fund the development of the *Nano Hummingbird* **[Keennon et al, 2012]** is that it can mistakenly be considered as a real hummingbird, which makes it valuable for military use.

1.3.3 ENGINEERING CHALLENGES
Three aspects of a robotic hummingbird make the development of one a challenging endeavour.

Generating the wing motion
The first challenge is to develop an artificial flapping mechanism (as the one discussed in chapter 4) that is able to convert the motion of the actuator(s) that drive(s) the wing motion to a hummingbird-like wing motion. As we will see in the next chapter, the hummingbird-like wing motion is a complex wing motion that has two degrees of freedom. This complex wing motion has to be performed in a predictable and reliable manner. The flapping mechanism has to be light enough and able to execute the wing motion fast enough (25-40 Hz) in order to generate enough thrust to lift off, as will be discussed in chapter 3. Furthermore, the flapping mechanism has to be robust enough to withstand over 100000 flapping cycles, which corresponds to about one hour of flight.

Enabling flight stability and control with an asymmetric wing motion
The second challenge is to implement the ability to alter the wing motion during flight in order to generate an asymmetric wing motion. The asymmetry may be one between the left and right wing, or between the forward and backward stroke, or a combination of the two. This asymmetric wing motion is necessary to stabilize flight and perform complex flight manoeuvres.
The implementation of an asymmetric wing motion has to comply with the issues raised in the previous paragraph about weight, speed and robustness.

Ensuring flight stability and control with an active feedback control of the wing motion and MEMS motion sensors.
A robotic hummingbird is not passively stable like a hot air balloon or a paper plane. It has no propellers that have a stabilizing effect as observed in multi-copters nor is it equipped with a stabilizing tail. A large tail is deliberately omitted to increase the manoeuvrability.

As a consequence, the wing motion has to be constantly adjusted (as described in the previous paragraph) to keep the robotic hummingbird from crashing. These adjustments to the wing motion have to be performed at a speed much higher than human pilot could follow. Therefore, the implementation of motion sensors is required. These sensors have to sense the orientation and the motion of the robotic hummingbird.

1.3.4 State of Art

Many different kinds of small drones or micro air vehicles already exist that use moving wings to stay aloft. We distinguish three main types: Clapping wing micro air vehicles, bird-like flapping wing micro air vehicles and hummingbird-like flapping wing micro air vehicles or robotic hummingbirds. With the exception of some, most of these small drones are in development at universities in the framework of academic research.

Clapping wing micro air vehicles

Clapping wing micro air vehicles use two pairs of wings that clap up and down against each other (Fig. 5) and take advantage of the so called 'clap and fling' effect **[Weis-Fogh, 1973].** Probably the best known example is the Delfly **[Delfly, 2017]** shown in Fig. 5. Clapping wing micro air vehicles are usually passively stable, tailed and have wings with low aspect ratio. Like butterflies they are unable to perform the swift flight manoeuvres of hummingbirds and are easily influenced by wind gusts because of their relative large wings and tail.

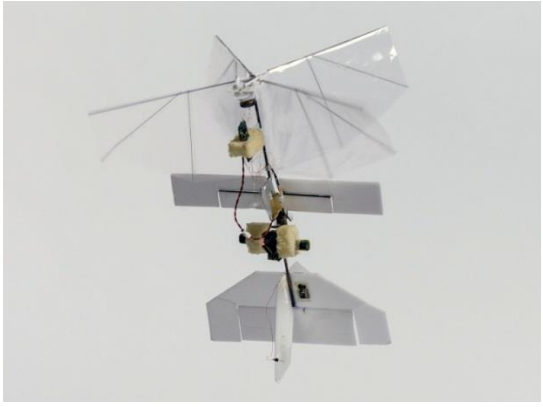

Fig. 5 The Delfly 2 with a wing span of 30cm [Delfly, 2017]

Bird-like flapping wing micro air vehicles

Bird-like flapping wing micro air vehicles use only one pair of wings that are flapped up and down, like large birds do. They need a forward flight velocity and a tail for flight stabilization and control, limiting their manoeuvrability. Some of them flex their wings during the upstroke like the *Smartbird* of *Festo* **[Smartbird, 2017]** (shown in Fig. 6A) while others use a thin wing which is not flexed during the wing motion like the *Microbat* (which was the first in its kind) developed by *Aerovironment* in 1998 **[Pornsin-Sirirak et al, 2001]**.

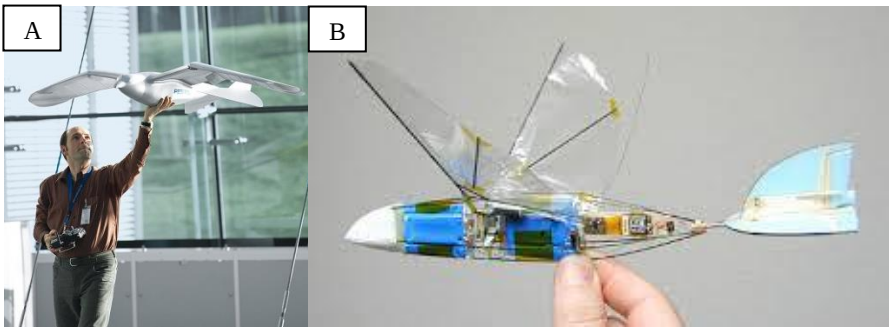

Fig. 6 Bird-like flapping wing micro air vehicles: **(A) The Smartbird [Smartbird, 2017] and (B) the Microbat [Microbat, 2017]**

Hummingbird-like flapping wing micro air vehicles

Table 1 gives an overview of the few Hummingbird-like (or insect-like) flapping wing micro air vehicles that have been developed so far. They are all able to fly untethered except for the Harvard *Robobee* **[Ma Kevin et al, 2013]**, shown in Fig. 7A, which is much smaller than the others. They are all tailless and mimic the horizontal wing motion of hummingbirds (or insects) to stay aloft. The *Nano Hummingbird* from *Aerovironment* **[Keennon et al, 2012]**, shown in Fig. 7B and developed in 2011, was the first to fly untethered, is still the most stable and has the longest flight endurance (T). The *Harvard Robobee* is by far the smallest tethered flying drone in the world with a wingspan of only 3 cm and a mass of only 80mg. The *Kulibrie* will be discussed in detail in chapter 6.

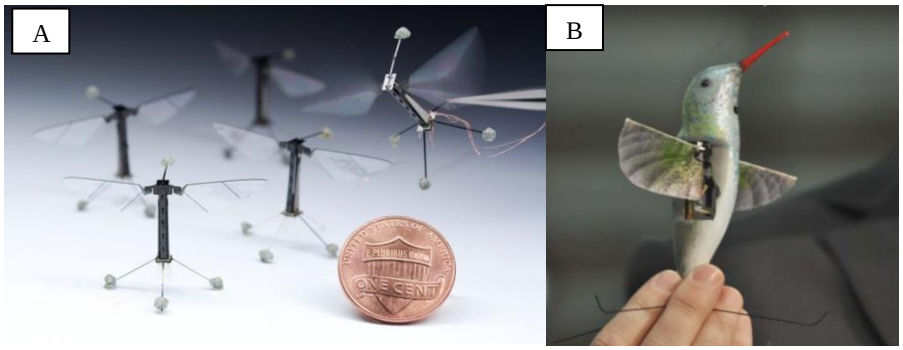

Fig. 7 Hummingbird-like flapping wing micro air vehicles: (A) The Harvard RoboBee with a wingspan of 30mm [Robobee, 2017] and (B) the Nano Hummingbird from Aerovironment with a wingspan of 165mm **[Keennon et al, 2012]**

	year	S (L) (mm)	m (g)	m wing (g)	A max (°)	f (Hz)	AR	c_{av} (mm)	T	# C	P (W)	Resonance
Nano Hummingbird Saturn prototype (Aerovironment, **[Keennon et al, 2012])**	2010	158 (68)	17,5	0.13 (0.8%)	>180	27.5	2.61	26	11m	> 60	3.27	no
Nano Hummingbird Final prototype (Aerovironment **[Keennon et al, 2012]))**	2011	165 (74)	19,0	not giver	>180	30	2.85	26	4m	> 60	?	no
Robobee (Harvard University **[Ma Kevin et al, 2013]**)	2013	30 (17)	0,08		110	120		NG	N	~12	0.019	yes
Robotic Beetle (Konkuk University**[Phan & Park , 2015]**)	2015	NG	18	not given	>180	26	NG	NG	30s	>40	?	no
Robotic Hummingbird (University of Maryland **[Coleman et al, 2015]**)	2015	305 (140)	62	0.85 (1.3%)	150	22	4.2	NG	5s	>50	>30W	no
Kulibrie (University of Leuven)	2015	186 (80)	14,0	0.15	>180	25	3.19	25	55s	12		yes
Robotic Hummingbird (Univeriste Libre de Bruxelles **[Altartouri et al, 2017]**)	2016	210	22,5	not given	NG	22	NG	NG	NG	NG	NG	no

Table 1 State of art of robotic hummingbirds: Currently six robotic hummingbirds have been developed that actively stabilise their flight by flapping their wings. They differ in wingspan (S), wing length (L), Stroke amplitude (A), flapping frequency (f), mean geometric chord (c_{av}), aspect ratio (AR), power consumption (P), flight endurance (T), amount of components (C) and whether or not they use a resonant flapping mechanism

Besides these three main categories of micro air vehicles with moving wings many others exist often using peculiar wing motions. Two examples are shown in Fig. 8: the Jellyfish like micro air vehicle **[Ristroph & Childres, 2014]** developed by *Ristroph* and the mono-copter **[Ulrich et al, 2010]** that is based on the seed of a maple tree and is developed by *Ulrich*.

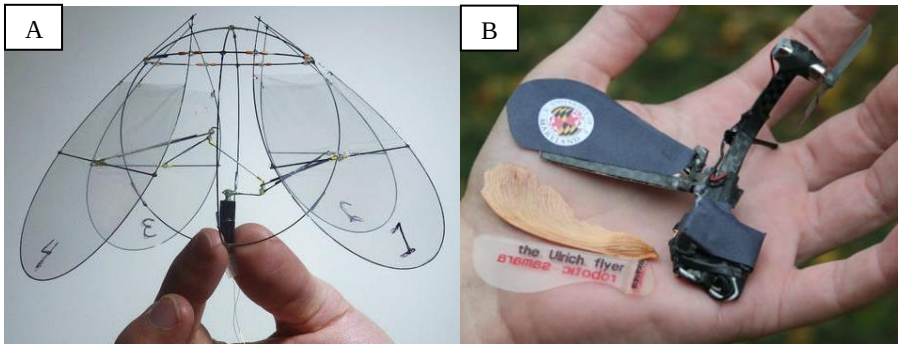

Fig. 8 Micro air vehicles with wings that make peculiar motions: (A) a jellyfish like micro air vehicle **[Ristroph & Childres, 2014]** and a mono-copter [Ulrich et al, 2010] that is based on the seed of a maple three.

How we can improve the state of art

At the moment, the Nano Hummingbird can be regarded as the state of art of robotic hummingbirds. Although it is an impressive achievement, its design can be improved on two points:

- The flapping mechanism of the Nano Hummingbird does not use resonance to improve its performance.
- The flapping mechanism of the Nano Hummingbird is very complex as Fig. 9 shows. It consists of more than 100 mechanical parts. The large amount of components increases the chance of failure and makes it cumbersome and expensive to build a prototype.

Fig. 9 The flapping mechanism of the Nano Hummingbird: A complex mechanism comprised of over 100 components.

1.4 RESONANCE

Many different flapping mechanisms for robotic hummingbirds have been proposed in literature. Most of them use a common pushrod mechanism that converts the rotational motion of an electromotor into a reciprocating hummingbird-like flapping wing motion. Such a flapping wing mechanism consumes energy during the whole wing motion; also during deceleration at the end of each wing stroke. The kinetic energy of the wing may however be stored in an elastic element during the deceleration phase of the wing motion. The energy that is stored in the elastic element may then be used to initiate the next wing beat in order to reduce the total power needed to drive the wing motion. Some insects are known to use their thorax to elastically store the kinetic energy of the wing during deceleration **[Schenato et al, 2003]**. The Harvard *RoboBee* also elastically stores the kinetic energy of the wing during deceleration **[Wood et al, 2003]**.

The addition of an elastic element to the flapping mechanism in order to store energy during the deceleration phase of the wing motion makes it a resonant flapping mechanism. The power consumption of a resonant flapping mechanism is optimized by tuning it such that its damped natural frequency matches the desired flapping frequency. Chapter 4 describes the resonant flapping mechanism that is designed in the framework of this research.

1.5 OVERVIEW

Chapter 2 describes the hummingbird-like wing motion and which aspects of it are important to take into account for the wing motion of a robotic hummingbird. Chapter 3 studies the influence of the wing size, the wing shape and the wing motion on the average thrust that it generates. In chapter four the resonant flapping mechanism is described and its power consumption and performance are studied. Chapter 5 studies how hummingbirds and insects are able to perform flight manoeuvres by performing an asymmetric wing motion and how these wing motions can be mimicked mechanically with the resonant flapping mechanism. Chapter 6 gives an overview of the development of the Kulibrie. And the final chapter gives an overview of the conclusions taken from this research and the proposed future research.

2 MECHANICAL RECONSTRUCTION OF THE HUMMINGBIRD WING MOTION

2.1 INTRODUCTION

Hummingbirds can be considered as good references in the design of small drones. They are small enough to take advantage of the peculiar thrust enhancing aerodynamic phenomena observed around insect wings. On the other hand they are large enough to be designed and manufactured with current mechanical technology. Furthermore they are the living proof of the large flight envelope that can result from using flapping wings, which allow them to swiftly perform amazing flight maneuvers.
Critical to the development of a robotic hummingbird is a thorough understanding of both the wing motion and the wings of hummingbirds.

Sections 2.2 and 2.4 describe the wing motion of hummingbirds and they also list the parameters of the hummingbird wing motion which are important to the design of a hummingbird-like flapping mechanism. The scope of this chapter is limited to the symmetric wing motion of hovering flight. The asymmetric wing motion used for flight control is studied in chapter 5. In order to make proper artificial hummingbird-like wings also the size, shape and structure of hummingbirds are studied in sections 2.3 and 2.5.

2.2 THE WING MOTION OF HUMMINGBIRDS

There are over 200 known species of hummingbirds (Trochilinae) **[Genera, 2017]**. All of them live in the Americas. Although some of them differ significantly in weight, size and flapping frequency, they all share the same typical wing motion. This wing motion is entirely different from the one of larger birds like pigeons, which flap their wings up and down and flex their wings during upstroke **[Berg & Biewener, 2008]**, but it is remarkably similar to the wing motion of many insects regardless of their size. Examples include hawkmoths (Agrius convolvuli), with wings of 48.3mm, Bumble Bees (Apis mellifera), with wings of 9.7mm or fruit flies (Drosophila melanogaster), with wings of 2.39mm **[Liu & Aono, 2009]**).

2.2.1 QUALITATIVE OBSERVATIONS

The wings of a hummingbird move so fast that their motion cannot be seen by the naked eye. To have a better understanding of the wing motion it is interesting to study high speed video images of hovering hummingbirds **[high speed, 2017]**. These high speed

video images reveal the basic characteristics of the hummingbird's wing motion. Fig. 10 shows the typical wing motion of hummingbirds.

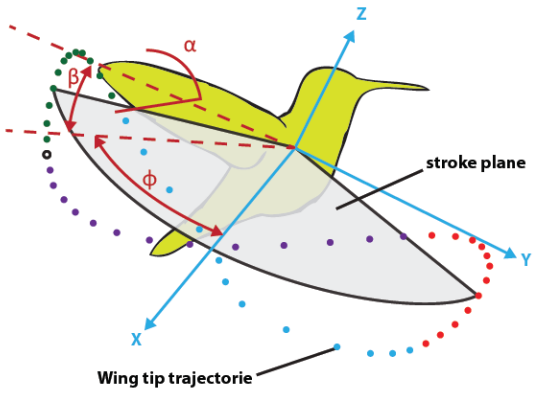

Fig. 10 Hummingbird-like wing kinematics: three angles are sufficient to fully describe the wing motion relative to the stroke plane. These angles are: The stroke angle ($\boldsymbol{\phi}$), the angle of attack ($\boldsymbol{\alpha}$) and the deviation angle ($\boldsymbol{\beta}$). The colored dots illustrate the forward stroke (blue), the pronation (red), backward stroke (purple) and supination (green). Taken and altered from [Phillips & Knowles, 2011]

Unlike larger birds which flap their wings up and down, hummingbirds and insects strike their wings back and forth in a stroke plane that is approximately horizontal. Therefore, the terms forward stroke and backward stroke are preferred over down-stroke and up-stroke, which are commonly used for the larger species.
Another difference between the wing motion of hummingbirds and the one of larger birds is that hummingbirds do not flex their wings during upstroke (backward stroke) like larger birds do.

Four phases in the wing motion can be distinguished (see Fig. 10). At the end of each wing stroke the wing rotates around its leading edge of the wing in order to maintain a suitable angle of attack during. In this work the term wing rotation is used for this aspect of the wing motion. The rotation just after the forward stroke is called the pronation and the rotation just after the backward stroke is called the supination. In addition to the stroke motion and the wing rotation, the wing deviates slightly up and down from the (horizontal) stroke plane **[Tobalske et al, 2007]**.

The wing motion of a hummingbird is almost symmetrical in backward and forward stroke during hovering flight. A closer study **[Tobalske et al, 2007]** however revealed small asymmetries between the forward and the backward stroke and a tilted (14°)

average stroke plane. Chapter 3 explains that a symmetric wing motion performs better than the asymmetric wing motion performed by hummingbirds.

2.2.2 FLAPPING FREQUENCY AND STROKE AMPLITUDE

The flapping frequency and the stroke amplitude have a large influence on the thrust generated by a hummingbird-like flapping wing (see chapter 3).

Table 2 is taken and adapted from **[Altshuler et al, 2010]**. It gives an overview of the flapping frequency (f) and the stroke amplitude (A) of a large set of hummingbirds during normal hovering flight mode. Altshuler et al. also measured the stroke amplitude (A_{max}) and stroke frequency (f_{max}) under maximum load conditions: when these hummingbirds lifted the maximum weight they could lift (m_{max}) including self-weight.

		m (g)	S_{fit} (mm)	L_{fit} (mm)	AR_{fit}	A(°)	f (hz)	f_{fit} (Hz)	m_{max} (g)	A_{max} (°)	f_{max} (Hz)	$F_{max-fit}$ (mm)
Klais	guimeti	2,6	95	40	7,4	160	33	40	7,4	187	40	50
Phaethornis	ruber	2,6	96	41	7,4	163	41	40	8	191	50	50
Microchera	albocoronata	2,6	96	41	7,4	180	37	40	5,3	203	44	50
Selasphorus	flammula	2,7	98	41	7,4	165	43	40	5,9	183	53	49
Phaethornis	longuemareus	2,7	98	42	7,4	175	43	39	5,8	193	53	49
Chlorostilbon	assimilis	2,7	98	42	7,4	183	31	39	5,7	188	38	49
Ocreatus	underwoodii	3,1	104	44	7,4	156	47	38	10	185	56	47
Chlorostilbon	mellisugus	3,1	106	45	7,4	155	37	37	8,8	191	43	46
Elvira	chionura	3,3	108	46	7,5	160	33	37	9,9	196	42	45
Selasphorus	platycercus	3,4	110	47	7,5	150	37	36	9,4	186	45	44
Adelomyia	melanogenys	3,5	111	47	7,5	157	32	36	10,7	195	37	44
Archilochus	colubris	3,7	115	49	7,5	151	44	35	6,5	184	52	43
Schistes	geoffroyi	3,7	115	49	7,5	152	33	35	10,9	181	41	43
Metallura	tyrianthina	3,8	116	50	7,5	159	31	34	9,8	189	36	42
Chalcostigma	ruficeps	3,8	117	50	7,5	141	30	34	9,9	177	35	42
Amazilia	amabilis	4,2	124	53	7,5	153	29	33	12,9	194	40	40
Lesbia	nuna	4,4	126	53	7,5	161	31	32	11,3	189	38	40
Amazilia	edward	4,4	127	54	7,5	160	31	32	12,6	196	40	40
Amazilia	saucerrottei	4,5	128	54	7,5	174	30	32	12,4	197	38	39
Eupherusa	eximia	4,5	128	54	7,5	149	28	32	12,8	190	36	39
Thalurania	furcata	4,5	128	55	7,5	147	32	32	13,6	187	39	39
Chrysuronia	oenone	4,6	129	55	7,5	156	33	32	13,8	186	42	39
Amazilia	decora	4,6	130	55	7,5	169	28	32	13,9	196	38	39
Aglaiocercus	kingi	4,7	130	55	7,5	155	32	31	12,9	185	34	39
Thalurania	columbica	4,7	130	55	7,5	158	31	31	13,3	192	41	39
Leucippus	chionogaster	5	134	57	7,5	146	35	31	13,8	183	38	38
Haplophaedia	assimilis	5,1	137	58	7,5	167	24	30	10,4	181	35	37

Heliothryx	barroti	5,1	137	58	7,5	172	23	30	13,5	199	30	37
Lafresnaya	lafresnayi	5,2	139	59	7,5	161	27	30	16,2	178	34	37
Phaethornis	koepckeae	5,3	139	59	7,5	158	27	30	14,9	183	33	37
Amazilia	tzacatl	5,3	140	59	7,5	166	26	30	15,3	192	36	36
Phaethornis	hispidus	5,3	140	59	7,5	155	30	30	15,2	178	35	36
Phaethornis	malaris	5,4	140	60	7,5	154	28	30	15,7	189	35	36
Phaethornis	guy	5,4	141	60	7,5	171	31	30	13,9	188	35	36
Doryfera	ludovicae	5,5	142	60	7,5	160	29	29	15,1	190	37	36
Colibri	thalassinus	5,6	143	61	7,5	161	25	29	17,9	192	33	36
Metallura	aeneocauda	5,6	143	61	7,5	164	30	29	14,2	190	34	36
Lampornis	cinereicauda	5,7	144	61	7,5	165	27	29	18,2	192	37	35
Heliangelus	amethysticollis	5,9	147	63	7,5	155	29	29	14,6	189	33	35
Glaucis	aenea	5,9	148	63	7,5	167	28	28	13,3	188	37	35
Threnetes	ruckeri	5,9	148	63	7,5	162	30	28	16	187	39	35
Panterpe	insignis	6	149	63	7,5	167	23	28	16	192	31	35
Chalcostigma	stanleyi	6	149	63	7,5	162	29	28	18,4	202	31	35
Threnetes	niger	6,1	150	64	7,5	160	28	28	16,3	184	36	34
Heliodoxa	aurescens	6,2	151	64	7,6	152	30	28	23,7	195	38	34
Heliodoxa	branickii	6,6	156	66	7,6	159	31	27	24,8	187	34	33
Phaethornis	superciliosus	6,6	157	67	7,6	165	26	27	16,8	193	33	33
Florisuga	mellivora	6,8	160	68	7,6	142	29	27	22,7	183	36	33
Oreonympha	nobilis	6,9	160	68	7,6	160	23	27	16,5	184	26	33
Chalybura	urochrysia	6,9	160	68	7,6	163	23	27	19,5	192	30	33
Eriocnemis	sapphiropygia	6,9	160	68	7,6	176	29	27	17,7	194	33	32
Aglaeactis	cupripennis	7,1	162	69	7,6	157	21	26	22,2	191	27	32
Taphrospilus	hypostictus	7,1	162	69	7,6	162	27	26	23,2	180	33	32
Glaucis	hirsuta	7,2	164	70	7,6	158	26	26	21,5	184	33	32
Heliodoxa	leadbeateri	7,4	166	71	7,6	162	30	26	25	190	34	32
Eugenes	fulgens	7,5	167	71	7,6	150	24	26	23	190	32	31
Aglaeactis	castelnaudii	7,5	168	71	7,6	169	23	26	19,9	192	27	31
Heliomaster	longirostris	7,6	169	72	7,6	178	30	26	17	195	37	31
Colibri	coruscans	7,7	170	72	7,6	148	24	26	20,1	183	29	31

Boissonneaua	matthewsii	7,9	172	73	7,6	161	26	25	19,7	195	30	31
Coeligena	violifer	8	174	74	7,6	155	25	25	20,7	191	29	30
Phaeochroa	cuvierii	8,1	174	74	7,6	167	25	25	22,3	193	33	30
Heliodoxa	jacula	8,1	174	74	7,6	163	28	25	21,9	194	33	30
Oreotrochilus	estella	8,1	174	74	7,6	155	29	25	18	180	33	30
Lampornis	clemenciae	8,4	178	76	7,6	151	23	25	24,6	185	31	30
Campylopterus	largipennis	8,7	181	77	7,6	156	21	24	34,1	188	29	29
Eugenes	fulgens	9,3	188	80	7,6	174	24	24	26,6	195	32	29
Eutoxeres	aquila	10,1	197	84	7,6	166	21	23	27,7	198	29	27
Campylopterus	hemileucurus	10,4	199	85	7,6	176	21	22	28,5	195	29	27
Eutoxeres	condamini	10,6	201	85	7,6	143	28	22	30,8	182	31	27
Patagona	gigas	22	296	126	7,7	154	15	16	45,9	180	18	

Table 2 Hummingbird characteristics: the mass (m), span width (S) estimated with expression 2.3, the wing length (L_{fit}) estimated as 42.5% of the wing span, the aspect ratio (AR_{fit}) estimated with expression 2.6, the peak to peak stroke amplitude (A), the flapping frequency (f) under normal load, the flapping frequency (f_{fit}) estimated with expression 2.1, the mass (m_{max}) under maximal load conditions (including body weight), the stroke amplitude (a_{max}) under maximal load conditions, the flapping frequency (f_{max}) under maximal load conditions and the flapping frequency ($f_{max\text{-}fit}$) under maximal load conditions estimated by expression 2.2 [Altshuler **et al**, 2010]

These measurements show that:

1) The **stroke amplitude is on average 160°** under normal load (self-weight of the bird only). As Fig. 11 (A) shows this value is not correlated to the mass nor the size of the hummingbird.
2) The **stroke frequency** for different type of hummingbirds is in de the range from about **21Hz to 47Hz, with the lower values for the larger species** (see Fig. 11 (B)). The data in Table 2 are relatively well approximated by the empirical formula 2.1 which relates the flapping frequency f_{fit} (in Hz) under normal flight conditions to the mass of the hummingbird (in g). (shown as the blue line in Fig. 11 (A)).

$$f_{fit} = 3.3 \cdot (0.001 \cdot m)^{-0.42} \qquad (2.1)$$

3) The stroke amplitude under maximum load is on average 189° under maximal loading. Stroke amplitude under maximal loading is not correlated to the mass nor the size of the hummingbird.

4) The stroke frequency under maximum load ranges from 25.9Hz to 55.5Hz, with the lower values for the larger species (see Fig. 11 (B)). The data in Table 2 are relatively well approximated by the following empirical formula which relates flapping frequency under maximum load conditions $f_{fit-max}$ (in Hz) in function of the mass of the hummingbird (in g). (shown as the red line in Fig. 11 (B)):

$$f_{fit-max} = 3.3 \cdot (0.0008 \cdot m)^{-0.44} \tag{2.2}$$

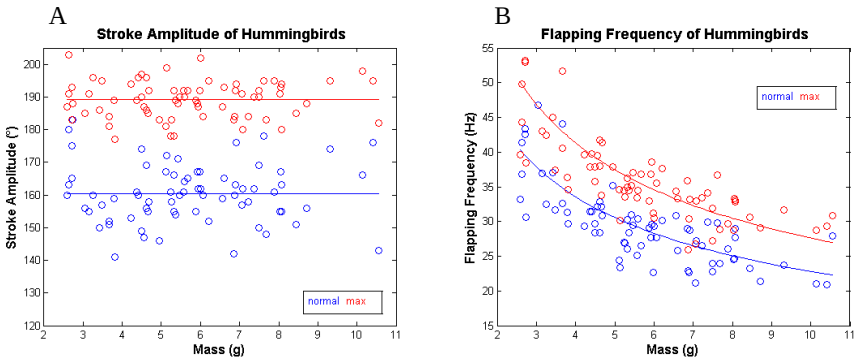

Fig. 11 Stroke amplitude and flapping frequency of hummingbirds: (A) shows a scatterplot of the stroke amplitudes from table 2 in function of the mass, (B) shows a scatterplot of the flapping frequencies from table 2 in function of the mass. The bleu dots represent the data under normal load conditions, while the red dots represent the data under conditions of maximal load. The full lines represent the average in A and the fits using expressions 2.1 and 2.2 in B

2.2.3 THE WING ROTATION AND THE ANGLE OF ATTACK FOR A HUMMINGBIRD-LIKE FLAPPING WING

For a fixed wing aircraft, the inclination of the wing relative to the flow is constant and described by the angle of attack (α). For a hummingbird-like flapping wing however, the inclination of the wing relative to the flow is variable during wing motion due to wing rotation and wing twist. Fig. 12 further shows that the wing of a hummingbird twists significantly under influence of inertial and aerodynamic loading. As a consequence the inclination of the wing decreases significantly from the root of the wing to the tip of the wing.

Fig. 12 Wing twist: the hummingbird twists considerably under influence of the inertial and aerodynamic load it experiences during flapping. Image taken at the start of the back stroke [Driver, 2017]

In this text we use a simplified measure for the wing inclination for a hummingbird-like flapping wing, based on the definition for the angle of attack for fixed wing aircraft. The angle of attack (α) for a hummingbird-like flapping wing is defined here as the angle between the wing cross-section at the wing root and the stroke plane during mid-stroke (see Fig. 13). This is a kinematic parameter that does not take into account the wing twist.

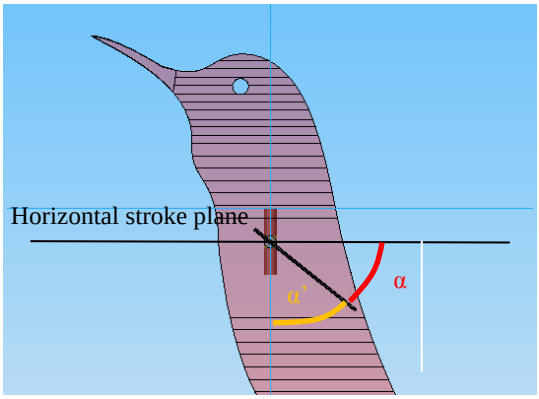

Fig. 13 Angle of attack (α) and Inclination angle (α') **as defined here for the hummingbird-like wing motion during forward stroke.**

Observations of high speed video images of hovering hummingbirds show that hummingbirds flap their wings with an angle of attack which is considerably larger than the angle of attack of fixed wing aircraft. The reason for this large angle of attack is explained in chapter 3.

An important consideration is whether the wing rotation is actively controlled by hummingbirds or it results passively from the interaction of the aerodynamic, inertial and elastic loads on the wing. It is known that some insects have small muscles that can

change the wing rotation while others do not have these muscles **[Schenato et al, 2003]**. One study indicates that passive wing rotation **[Sapir & Dudley, 2012]** is sufficient to control flight in the case of hummingbirds, but it does not rule out the possibility of an actively controlled wing rotation.

Many other parameters of the wing motion affect the level of thrust that is generated. The parameters which are most commonly referred to in the literature are:

- the figure of eight motion due to the wings' deviation from the average stroke plane **[Yang et al, 2009]**
- the speed of the wing rotation **[Sane, 2003]**
- the phase between the wing rotation and the wing stroke **[Dickinson, 1999**]

The influence of these parameters on the thrust generated by a flapping wing is less important than the influence of the flapping frequency, stroke amplitude and angle of attack and hence they are discussed further in depth here.

2.3 THE WING OF A HUMMINGBIRD

This section describes the most important aspects of hummingbird wings, their size (wing length), shape, structural stiffness and mass (section 2.3.1). The main focus is on the aspect ratio (section 2.3.2). The structural stiffness of hummingbird wings plays an important role in the performance of the nano-robot, but that is a subject for future research. Section 2.3.3 is merely a quick summary of the most basic observations concerning the structural stiffness of a hummingbird wing.

2.3.1 WINGSPAN AND WING LENGTH

Fig. 14 shows the wing span (S) of a hummingbird. It is defined as the distance between the two wing tips if they are in line with each other, while the wing length (L) is defined as the distance between the wing tip and the stroke axis, as shown in Fig. 14. The wing span is equal to the sum of twice the wing length and the distance between the two shoulders. Although in literature, the size of a hummingbird is usually marked by its wing span because it is easier to measure, the wing length is taken as a reference here for the size of a (robotic) hummingbird, because the distance between the shoulder joints is less critical for the design of a robotic hummingbird, and also because a number of experiments are performed with only one wing.

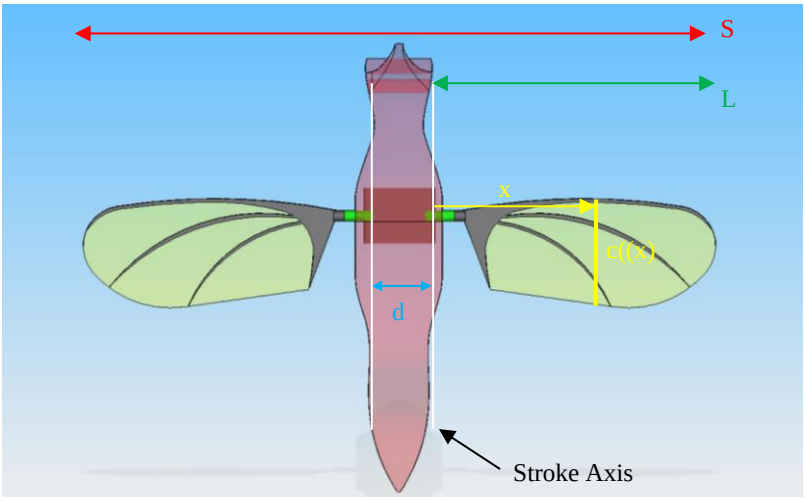

Fig. 14 Defining the size of a hummingbird: The wing span (S) defined as the distance between the two wing tips, wing length (L) defined as the distance between the stroke axis and the wing tip. The shoulder to shoulder distance (d), and the chord width c(x) at a distance x from the wing root.

Based on measurements **[Shyy et al, 2007]** derived an empirical expression for the wingspan (S) in mm of a hummingbird as a function of its mass (in g).

$$S = 2.24\, m^{0.53} \tag{2.3}$$

Table 2 shows the estimated wing span of many hummingbird species derived from expression 2.3. The wingspan increases with increasing mass from 95 mm for the *Klais guimeti* that only weighs 2.5g to 295mm for the *Patagona gigas* with a mass of 22.0g.

To estimate the wing length from the wing span the distance between the two shoulders is estimated to be 15% of the wing span. Table 2 shows the estimated wing length of many hummingbird species. The wing length increases with increasing mass from 40mm for the *Klais guimeti* to 125mm for the *Patagona gigas*.

2.3.2 WING SHAPE AND ASPECT RATIO

Fig. 15 and Fig. 16 show the shape of a hummingbird wing. To fully describe the wing shape an expression for the chord length (c) as a function of the distance to the shoulder can be derived empirically from measurements **[Ellington, 1984]**.

Fig. 15 The hummingbird wing shape **[Kruyt et al, 2014]**

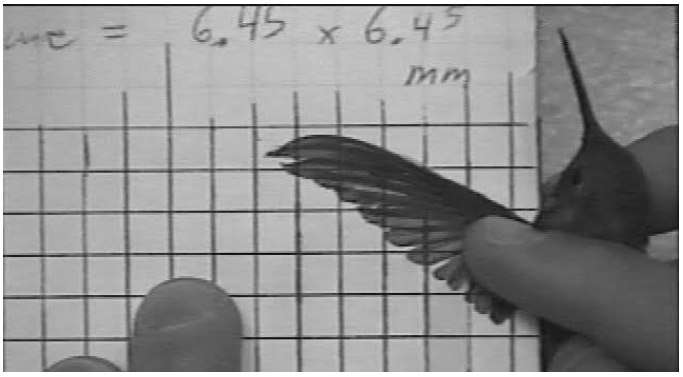

Fig. 16 The hummingbird wing shape and size of a Rufous Hummingbird **[by mail from prof. Altshuler]**

The aspect ratio of a wing is a dimensionless number that compares the span of an airplane to the mean geometric chord length of its wings. For a rectangular wing, the geometric chord length is a constant number and the aspect ratio can be defined as the ratio of the wingspan to the geometric chord length (c) of the wing. Hummingbird wings are not rectangular, they are tapered and the leading edge is curved towards the trailing edge near the wing tip (Fig. 15) as a consequence the geometric chord length varies along the span, it can be expressed as a function of the distance to the stroke axis (x) (see Fig. 14). The aspect ratio for hummingbird wings can be defined as follows:

$$AR = S/c_{mean} \tag{2.4}$$

With c_{mean} the mean geometric chord length defined as:

$$c_{mean} = \int_0^L c(x)dx \tag{2.5}$$

Based on measurements **[Shyy et al, 2007]** derived an empirical expression for the aspect ratio (AR) of a hummingbird in function of its mass (in g).

(2.6)

$$AR = 7.28\, m^{0.02}$$

Table 2 shows the estimated aspect ratio of many hummingbird species derived by expression 2.6. The aspect ratio increases slightly with increasing mass from 7.4 for the *Klais guimeti* to 7.7 for the *Patagona gigas*.

2.3.3 WING STRUCTURE AND STIFFNESS

The wings of hummingbird have a sharp (Fig. 16) and stiff leading edge. The wing planform is made of flight feathers resulting in a thin, highly flexible wing stiffened mainly by the shafts of the flight feathers which are called the rachis. This wing structure is similar to the wing structure of insects **[Jongerius & Lentink, 2010]** and **[Tanaka & Wood, 2010]**. This structure results in large wing twist during flight.

2.3.4 MASS

The mass of a hummingbird wing is about 3-5% of its body mass **[Chai & Millard, 1997]**. More important is the inertia of the wing around its stroke axis, for which no values could be found in literature.

2.4 MECHANICAL RECONSTRUCTION OF THE WING MOTION OF A HUMMINGBIRD

This section describes how the hummingbird's wing motion can be reconstructed in an artificial system using a flapping wing mechanism that converts the motion of one or several mechanical actuators into the complex wing motion of a hummingbird.

The requirements for such a flapping wing mechanism are listed first. Section 2.4.2 proposes a simplification of the hummingbirds' wing motion that reduces the complexity of the flapping wing mechanism considerably.

2.4.1 CRITICAL REQUIREMENTS AND CRITERIA

The mass and thrust-mass ratio

A flapping mechanism for a robotic hummingbird must meet several requirements and criteria. In order to ensure that a robotic hummingbird is able to take off, the thrust-to-weight ratio of a robotic hummingbird needs to be larger than one and preferably as high as possible. Table 2 shows estimates for the maximum mass of robotic hummingbirds of

different wing spans based on the assumption that they generate a wing motion at frequency f_{max} and amplitude A_{max}. These estimates are derived from the empirical data in Table 3 as 70% of m_{max}.

m (g)	5,4	7,3	8,3	9,4	10,5
S (mm)	141	165	177	188	200
L (mm)	60	70	75	80	85
A (°)	160				
Amax (°)	189				
α(°)			~45		
f (Hz)*	29	26	25	23	22
fmax (Hz)*	36	32	30	28	27
upper limit for the mass of robotic hummingbird (70% of mmax)(g)	10.4	15.1	17.2	18.6	20.7

Table 3 estimates for key parameters of a robotic hummingbird in function of its wing length. For the meaning of S, L, A, α, f, fmax we refer to Table 2. The upper limit for the weight is arbitrarily taken as 70% of the mass a hummingbird of the same size.

Mutable wing motion

In order to stabilise flight and perform flight manoeuvers the flapping mechanism should be able to alter (mute) the wing motion during flight as will be discussed in chapter five.

Besides these critical requirements other criteria like the power consumption, robustness, producibility and cost are important criteria to evaluate the flapping mechanism of a robotic hummingbird. These aspects are not discussed in detail.

The stroke amplitude

A maximum stroke amplitude is desired to maximise thrust (see chapter 3) but also to minimise power consumption (see chapter 4). The maximum stroke amplitude is limited to the value at which the wing tips would collide with each other. A maximum stroke amplitude of about 180° - 190° is expected. It may exceed 180° taking into account the shoulder width, and it depends on the geometry of the wing, the wing rotation and the distance between the shoulder joints of the robotic hummingbird.

Section 2.2 shows that hummingbirds are capable of generating such large stroke amplitudes, on average 188°, under conditions of maximal wing loading.
However under normal flight conditions (only lifting their self-weight) the average stroke amplitude of hummingbirds at 160° remains well below the maximum value. This

is necessary to leave some margin for the execution of flight maneuvers and rapid accelerations (see chapter 5).

As a consequence two requirements follow for the stroke amplitude of a robotic hummingbird flapping mechanism. First it should be possible to generate a maximum stroke amplitude of at least 180° and secondly the thrust generated by the flapping wing should be sufficient to lift the weight (thrust/weight ratio = 1) of the robotic hummingbird for a stroke amplitude of 160° or less. These requirements are summarised in Table 3.

The design of a mechanical lightweight mechanism that is capable of generating such large stroke amplitudes at high frequencies is not straightforward. Common crank rod mechanisms for examples are not able to generate such large stroke amplitudes and as a consequence some creativity is needed in designing a proper hummingbird-like flapping mechanism.

The flapping frequency

A flapping frequency as large as possible is desired to maximise thrust (see chapter 3). In practice however the flapping frequency is limited by the available power (battery mass) and by the maximum load the wings and the flapping mechanism can take.
The inspiration for the desired flapping frequency of a robotic hummingbird comes from the flapping frequencies of hummingbirds. Section 2.2 shows that the flapping frequency depends on the mass for hummingbirds. Table 3 shows the estimate of flapping frequency for different wing lengths. These values are derived using expression 2.1.

The angle of attack

The angle of attack for a hummingbird-like wing motion as defined above is governed by the wing rotation. The optimal angle of attack depends strongly on the wing twist and on the aspect ratio of the wing.

An important consideration is whether or not it is necessary to actively control the angle of attack in order to perform flight manoeuvers. Chapter 5 shows that an active wing rotation is not necessary to perform flight manoeuvers, but is it preferred to perform flight manoeuvers more efficiently and to enlarge the flight envelope. An actively controlled wing rotation however increases the mechanical complexity of a flapping mechanism, because a mechanism has to be developed that translates the motion of extra actuators to the wing rotation that is superposed onto the stroke motion.

None of the currently existing robotic hummingbirds is able to directly affect the wing rotation. The Nano hummingbird and the robotic hummingbird of the University of Maryland affect the wing inclination indirectly by respectively controlling the wing’s stiffness and the stroke plane. The Harvard Robobee is able to fully control flight without active control of the wing rotation.

2.4.2 THE SIMPLIFIED HUMMINGBIRD-LIKE WING MOTION

In order to considerably reduce the complexity of the flapping wing mechanism, the wing motion of the hummingbird can be much simplified without too drastic effect on the average thrust generated by the flapping wing. It is this simplified wing motion that is generated by all existing robotic hummingbirds (see Table 1) including the two flapping mechanisms that are developed in the framework of this PhD.

The simplified wing motion is based on the following assumptions:

- The wing's deviation from the stroke plane, which has a very small amplitude, has no significant effect on the average thrust generated by the flapping wing and it can therefore be omitted.
- The stroke plane is horizontal.
- The stroke motion may be assumed to vary harmonically in time.
- The only aspects of the wing rotation that have a significant influence on the average thrust generated are the angle of attack during forward and backward stroke, the speed of the wing rotation and the phase between wing rotation and the wing stroke.

By neglecting the wing deviation, the wing motion has two degrees of freedom with respect to the body: the stroke motion that can be described with the stroke angle (θ) (see Fig. 10) and the wing rotation that can be described with the inclination angle (α') (see Fig. 13).

Similar to **[Berman & Wang, 2007]** and **[Karasek & Preumont, 2014]** the stroke angle (ϕ) as shown in Fig. 10 and inclination angle (α') as shown in Fig. 13 can be parametrised as follows:

$$\phi = \phi_0(t) + \frac{A}{2}\cos(2\pi f t) \tag{2.7}$$

$$\alpha' = \alpha_0 + \frac{\frac{\pi}{2} - \alpha_m}{\tanh(k_\alpha)} \tanh[k_\alpha \sin(2\pi f t - \varphi_\alpha)] \tag{2.8}$$

In equation 2.7 ϕ_0 is the mean stroke angle, A is the stroke peak-to-peak amplitude and f is the flapping frequency. In equation 2.8, α_0 is the inclination offset, α_m is the geometric angle of attack around mid-stroke, φ_α the phase shift between the stroke and the inclination. The parameter k_α defines shape of the inclination angle function from harmonic ($k_\alpha = 0$) to square wave ($k_\alpha = \infty$).

The results of the experiments described in chapter 3 show that the average thrust generated by this simplified wing motion is larger than the average thrust generated by a hummingbird that performs the same wing motion.

2.5 CONCLUSION

The hummingbird-like wing motion

Unlike larger birds which flap their wings up and down, hummingbirds and insects strike their wings back and forth in a stroke plane that is approximately horizontal. At the end of each wing stroke the wing rotates around the leading edge of the wing to maintain a proper angle of attack during both forward and backward stroke. The most important parameters of the wing motion of a hummingbird are the flapping frequency, stroke amplitude and the angle of attack; they determine the thrust that can be generated by a flapping wing of a prescribed size. An estimate for these parameters and the maximum mass for a robotic hummingbird can be derived empirically by comparison with real hummingbirds. Table 4 shows the estimates for five different wing lengths.

m (g)	5,4	7,3	8,3	9,4	10,5
S (mm)	141	165	177	188	200
L (mm)	60	70	75	80	85
A (°)	160				
A_ max (°)	189				
α(°)			~45		
f (Hz)*	29	26	25	23	22
f_ max (Hz)*	36	32	30	28	27
maximum mass of robotic hummingbird (70% of m_max)(g)	10,4	15,1	17,2	18,6	20,7

Table 4 The main parameters for the design of a robotic hummingbird **for 5 different wing sizes**

In order to considerably reduce the complexity of the flapping wing mechanism, the wing motion of the hummingbird can be much simplified without too drastic effect on the average thrust generated by the flapping wing.. It is this simplified wing motion that is generated by all existing hummingbird-like flapping wing micro air vehicles including the two flapping mechanisms that are developed in the framework of this research.

A first flapping mechanism, the stroke-cam mechanism, translates the rotational motion of the driving shaft of a motor to a sinusoidal back and forth stroke motion by means of a cam. This mechanism drives the large stroke amplitude and large flapping frequencies needed to generate sufficient thrust. It was abandoned in favour of the resonant flapping

mechanism (chapter 4) because it is too fragile and the wing motion is not sufficiently predictable.

The hummingbird-like wing

The aspect ratio of a hummingbird wing is approximately 7 and it only slightly depends on its size. During this research project over 100 different artificial wings are made. Many different materials, sizes, shapes and structural compositions are tested experimentally. These qualitative tests resulted in the latest wing shown in Fig. 18. More research should be done to optimize the wings.

3 AERODYNAMICS OF A FLAPPING WING AND THRUST GENERATION

3.1 INTRODUCTION

The average thrust, which is defined as the resulting vertical and downward force generated by a hummingbird-like flapping wing, is one of the most important design considerations in the development of a robotic hummingbird. It limits the total mass of a robotic hummingbird, which in turn limits the size and the power of the actuators, the size and the energy capacity of the battery and the mass and sensing capability of the avionics. Furthermore, with a certain state of technology it sets a lower limit to the size of a robotic hummingbird or insect. Needless to say that it is of critical importance to maximise the average thrust that can be generated by a hummingbird-like flapping wing.

This chapter focusses on aerodynamic phenomena around flapping wings and the influence of the wing motion, shape and size on the average thrust that can be generated. First a literature study on the aerodynamic phenomena around flapping wings is presented. Without these phenomena insects would not be able to fly. Section 3.3 discusses the PIV measurements that are performed in the framework of this research to study if the aerodynamic phenomena also occur around artificial hummingbird-like flapping while executing the simplified wing motion. Section 3.4 presents an extensive experimental parameter study of 740 experiments, resulting in the largest data set which is currently available. The objective of this study is to identify the influence of the most important parameters of the wing morphology and wing motion on the average thrust that is generated. The result of this study is the selection of the most effective motion and shape for the robotic hummingbird which is described later in chapter 6.

3.2 THE AERODYNAMIC PHENOMENA AROUND FLAPPING WINGS: LITERATURE STUDY

According to classic aerodynamic wing theory, small insects, like bees, flies or fruit flies are unable to generate sufficient thrust to stay aloft. In the case of flapping wings, thrust is defined here as the vertical and upward component of the force which is generated by the flapping motion of a wing or a set of wings. Quasi-steady models which take into account the motion of the wing in the assumption of a steady flow around the wing systematically underestimate the amount of thrust generated by a flapping wing **[Ho et al, 2003], [Sane, 2003], [Wakeling & Ellington, 1997].**

This section discusses four peculiar aerodynamic phenomena that enhance the thrust generated by a flapping wing:

- the stabilization of the leading edge vortex (LEV)
- the Kramer effect
- wake-capture
- the added mass effect

These phenomena and in particular the stabilisation of the leading edge vortex explain why insects but also hummingbirds are able to generate more thrust with their tiny wings than calculated using the classic aerodynamic wing theory.

Most of the experimental studies concerning the aerodynamics around flapping wings are performed on models that dynamically scale up the flapping wings of very small insects like the tiny fruit fly or the large Manduca sexta **[Dickinson, 1999], [Ellington, 1997]**. As a result more information on flapping wing aerodynamics is available at insect scale than at hummingbird scale.

3.2.1 THE STABILIZATION OF THE LEADING EDGE VORTEX BY FLAPPING WINGS

The leading edge vortex

The leading edge vortex (LEV) is a strong vortex that is shed from the leading of an aerofoil when the angle of attack of the aerofoils rapidly changes **[Anderson & John, 2010].** This vortex (see Fig. 17), briefly increases the lift produced by the aerofoils as long as it travels backwards above the wing (dynamic stall). As soon as it passes behind the trailing edge, however, the lift reduces significantly, and the wing is in normal stall.
The sharper the leading edge and the higher the angle of attack, the easier a leading edge vortex initiates. To prevent normal stall from happening, conventional aircraft wings have blunt leading edges and their angle of attack is limited to about 12° **[Anderson & John, 2010]**.

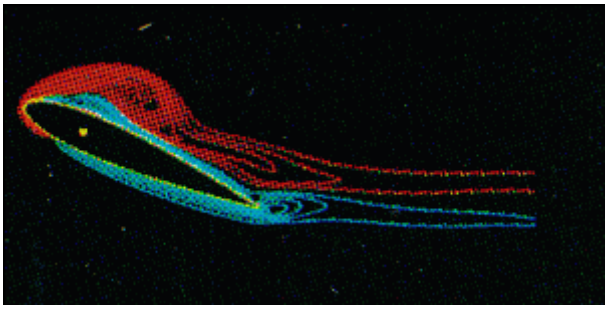

Fig. 17 The Leading Edge Vortex: Under certain conditions a leading edge vortex develops above the wing that results briefly in a zone of lower pressure. [Steiger **et al**, 2011]

The stabilisation of leading edge vortex by flapping wings

If the leading edge vortex can be stabilised so that it does not travel to the back of the wing or travels slowly to the back of the wing, the leading edge vortex generates an ongoing lift enhancement. This stabilisation of the leading edge vortex is exactly what happens at the flapping wings of fruit flies **[Dickinson, 1999**] and of the Rufous hummingbird **[Warrick et al, 2005]**. This principle is the main reason why a sharp leading edge and a relatively high angle of attacks are observed on insect and hummingbird wings.

Earlier studies **[Ellington, 1997]** observed a spiral shaped leading edge vortex over the wings of a Manduca sexta, in an analogy to the spiral shaped leading edge vortex generated by delta wings under a high angle of attack wing as shown in (Fig. 18) This analogy led to the assumption that the span wise flow (from root to wing tip) stabilises the leading edge vortex by carrying momentum away from the leading edge vortex in span wise direction as is the case for delta wings. By carrying momentum away from the leading edge vortex in span wise direction, its chord wise growth is kept small enough to avoid stall.

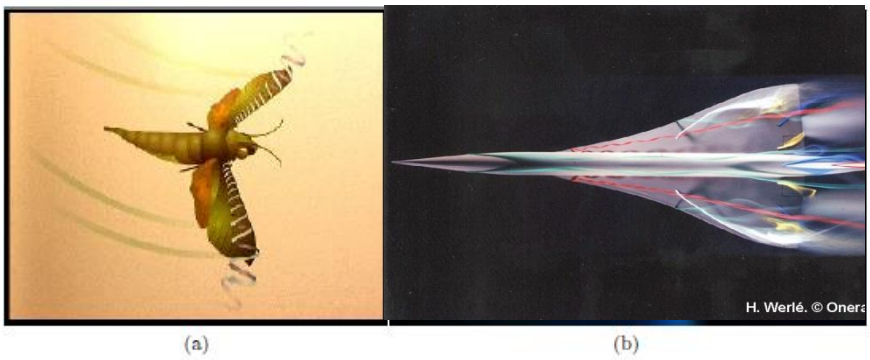

Fig. 18 Spiral shaped LEV: Ellington [Ellington, 1997] observed a spiral shaped leading edge vortex over the wings of a Manduca sexta (a), in an analogy to the spiral shaped leading edge vortex generated by the wings of a delta under a high angle of attack (b) [Werlé **et al** , 2011].

In depth studies using a dynamically scaled model of a fruit fly flapping wing **[Lentink & Dickinson, 2009]** showed that the leading edge vortex is not stabilised by the span wise flow but that it is stabilised by the 'quasi-steady' centripetal and Coriolis accelerations that result from the stroke motion of the wing and that angular acceleration is to mediate LEV spiral bursting, which is a high Reynolds number effect. Their analysis and experiments further suggest that the mechanism responsible for LEV stability does not depend on Reynolds number, at least over the range most relevant for insect and hummingbird flight ($100<Re<14{,}000$).

The strength of the leading edge vortex and its positive effect on the average thrust force increase with increasing wing speed. Hence increasing the flapping frequency or the stroke amplitude increases the thrust generated by the leading edge vortex **[Ho et al, 2003]**.

The stabilised leading edge vortex around hummingbird wings

Particle image velocimetry (PIV) measurements of the flow generated by the wings of a Rufous hummingbird during hovering flight show the existence of a stabilised leading edge vortex, but only during the forward stroke **[Warrick et al, 2005]**. As a consequence 75% of all thrust generated by the wing motion of the Rufous hummingbird is generated during the forward stroke. This observation explains why a robotic hummingbird with a symmetric forward and backward stroke may stabilise a leading edge vortex during both forward and backward stroke when hovering and hence generate considerably more thrust than its biological counterpart.

3.2.2 THE KRAMER EFFECT

(Fig. 19) shows the time course of the thrust generated by a dynamically scaled flapping wing of a fruit fly **[Sane & Dickinson, 2002]**. Two peaks in the thrust can be distinguished: a first one just before stroke reversal and the second one just after stroke reversal. These two peaks contribute about 35% of the total thrust generated. Computational simulations confirmed this observation **[Liu & Aono, 2009]**.

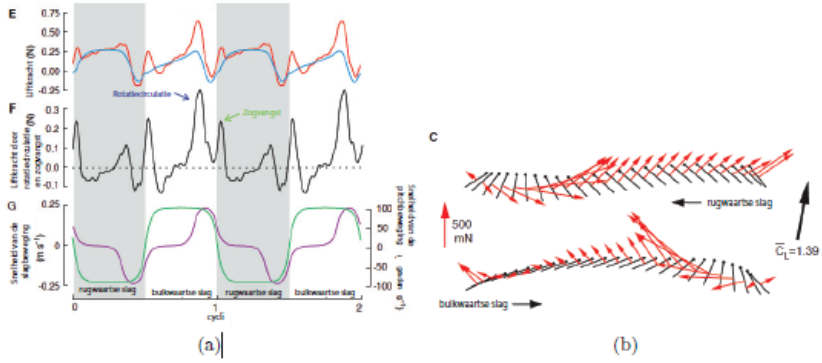

Fig. 19 **The thrust on a flapping wing**: (a) Shows the time course of the forces on a flapping wing of a dynamically scaled flapping wing of a fruit fly **[Sane & Dickinson, 2002].** The red line shows the resulting force, the blue line shows the components resulting from the stroke motion and the black line shows the force resulting from the rotational circulation and wake-capture. (b) Shows the direction of the resulting force during the wing motion.

The extent to which these peaks in thrust occur around the much larger flapping wings of a hummingbird is still unknown. Measurements around the flapping wing of a Rufous hummingbird using the technique of particle image velocimetry (this technique will be described in section 3.3) **[Warrick et al, 2005]** were inconclusive on the existence of these peaks.

The thrust peak just before stroke reversal is caused by the Kramer effect sometimes referred to as the 'rotational forces' **[Sane, 2003]**. The rotation of the wing around its span-wise axis (the wing rotation) generates an additional amount of rotational circulation in the fluid to re-establish the Kutta condition at the trailing edge.

The amount of thrust generated by the Kramer effect depends on the phase between the stroke motion of the wing and the wing rotation. When the wing rotation occurs mainly before the stroke reversal it is called an advanced wing rotation. When the wing rotation occurs mainly after the stroke reversal it is called a delayed wing rotation. When the wing rotation occurs mainly during the stroke reversal it is called symmetrical wing

rotation. The measurements performed by Dickinson on a dynamically scaled model of a fruit fly **[Sane & Dickinson, 2002]** showed that an advanced wing rotation results in a positive effect on the thrust force and a delayed wing rotation results in a negative effect on the thrust force. Dickinson's experiments revealed a significant effect of the time when rotation takes place: average thrust generated by an advanced wing rotation was found to be 70% larger than with a delayed wing rotation.

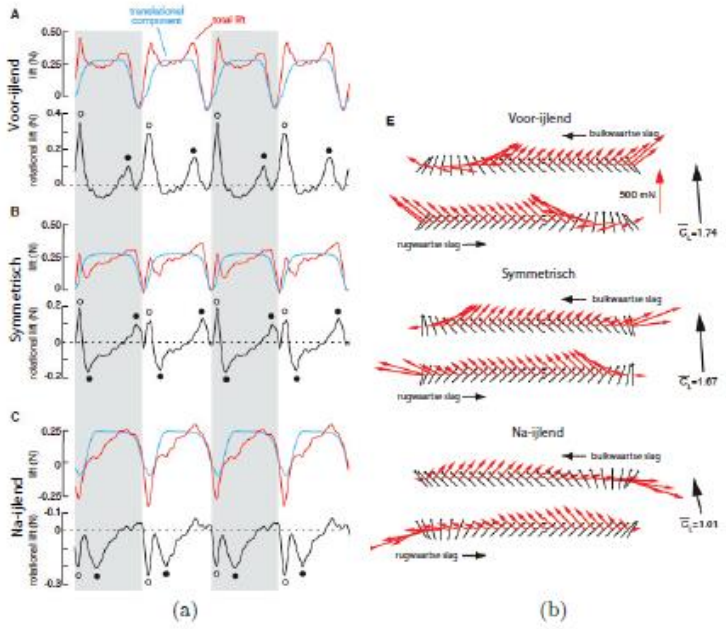

Fig. 20 **Advanced vs. delayed wing rotation:** (a) Shows the time course of the forces on a flapping wing of a dynamically scaled flapping wing of a fruit fly like in Fig. 19 **[Sane & Dickinson, 2002],** in the case of advanced, symmetrical and delayed wing rotation. (b) Shows the direction of the resulting force during the wing motion in case of advanced, symmetrical and delayed wing rotation.

3.2.3 WING-WAKE INTERACTIONS

One explanation for the thrust peak just after stroke reversal is based on wing-wake interactions, commonly referred to as wake capture. At the beginning of each wing stroke the wing goes through the wake generated by the previous wing stroke (see Fig. 21). This wake moves with an opposite velocity of the wing resulting in an increased thrust generated.

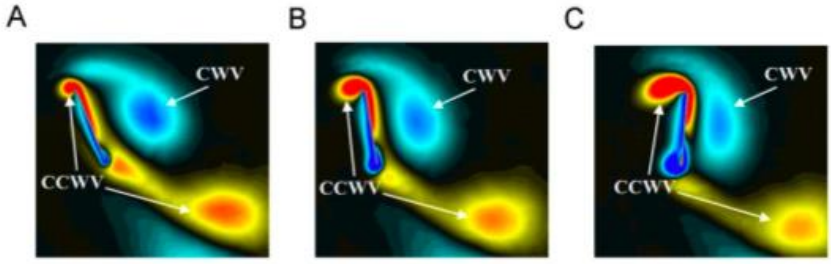

Fig. 21 Wake Capture: (A) Supination, (B) start of back ward stroke, (C) during early back ward stroke. The wake caused by the previous stroke (CWV) moves to the left and to the wing that starts to accelerate towards this wake (image from [Shyy **et al**, 2010])

The thrust peak resulting from wake capture is large and positive for an advanced wing rotation, small and positive for asymmetrical wing rotation and small and negative for a delayed wing rotation **[Sane & Dickinson, 2002]**.

3.2.4 THE ADDED MASS FORCE

Another explanation for the thrust peak just after the stroke reversal is the added mass of the accelerating wing. When an object accelerates through a fluid it encounters a reaction force due to the accelerated fluid. This reaction force is called the added mass **[Sedov, 1965]**. After stroke reversal the wing accelerates and experiences this added mass. The larger the wings' acceleration, the larger the added mass.

3.3 PIV MEASUREMENTS OF THE FLOW AND THE AERODYNAMIC PHENOMENA AROUND A HUMMINGBIRD-LIKE FLAPPING WING.

The flow around an object like a flapping wing can be measured and represented as a vector field by the particle image velocimetry method (PIV). Particle Image Velocimetry (PIV) is an optical measurement technique used to determine velocity vector fields of a flow. Tracer particles are seeded in the flow by a nebuliser. The flow is then illuminated by a laser sheet. The tracer particles light up so that they can be seen on pictures taken by one or more (high speed) cameras. The PIV technique relies on the cross correlation of successive pictures taken with a short time interval. The velocity vectors of the tracer particles are calculated by numerical differentiation of the calculated displacement vectors with the time interval between the two pictures. Planar PIV determines the

velocities that lie in the laser sheet. A more thorough background on PIV can be found in **[Melling, 1997]**.

A few researchers have studied the aerodynamic phenomena around a hummingbird-like flapping wing using PIV measurements. Benedict **[Benedict & Coleman, 1997]** studied the aerodynamics around and the thrust force produced by a mechanical hummingbird-like flapping wing at a Reynolds number of approximately 25000. They observed an increase of thrust due to the stabilisation of the leading edge vortex. Deng et al. **[Deng et al, 2016]** studied the aerodynamics around and the thrust force produced by a mechanism which claps two pairs of wings to each other. However the kinematics of clapping wings is profoundly different from the kinematics of a hummingbird-like flapping wing.

Sections 3.3.1 and 3.3.2 describe two sets of PIV measurements of the flow around a flapping wing that are performed in the framework of this research. These are the first and still only PIV measurements of the flow around a mechanical hummingbird-like flapping wing.

3.3.1 FORCE AND FLOW ANALYSIS OF THE FLOW AROUND A HUMMINGBIRD-SCALED FLAPPING WING BY 2D PIV MEASUREMENTS

RESEARCH OBJECTIVES

The objectives of these experiments are: visualising the leading edge vortex that is expected, validating the occurrence of wake capture and estimating the thrust generated by the flapping wing during hovering by measuring and analysing the flow around a mechanical hummingbird-like flapping wing using 2D Time-Resolved Particle Image Velocimetry (TR-PIV). Because this technique only allows to measure the flow in 2 dimensional planes, we measured the flow in 24 different planes to gain a better insight in the flow phenomena.

MATERIALS AND METHODS

The wing and the flapping mechanism

The flapping mechanism used in this paper is the stroke-cam mechanism which is described in the appendix X and is shown in Fig. 22.

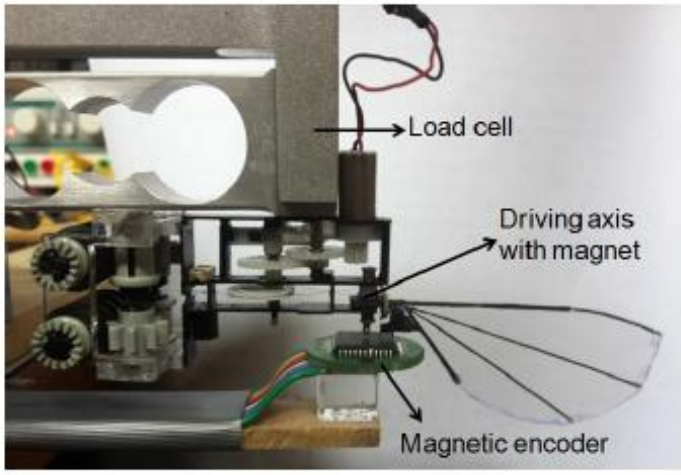

Fig. 22 The stroke-cam mechanism used in the experiments

The stroke-cam mechanism generates a symmetrical hummingbird-like wing motion, similar to the one of a hovering hummingbird. It is probably the lightest hummingbird-sized flapping wing mechanism which has been developed so far and it generates a harmonic wing stroke with both a high flapping frequency (up to 42Hz) and a large stroke amplitude (up to 180°). The wing rotation is geometrically limited to about 45°. For these experiments we choose a flapping frequency of 35 Hz and a stroke amplitude of 171°

The wing is a Mylar foil which is stiffened by thin carbon composite tubes (see Fig. 22). The wing has a length of 50mm (measured from wing tip to stroke axis) and its mass is 0.04gram. Fig. 23 shows a sketch of the wing planform. Table 5 lists numerical values of the dimensions which are shown in the sketch.

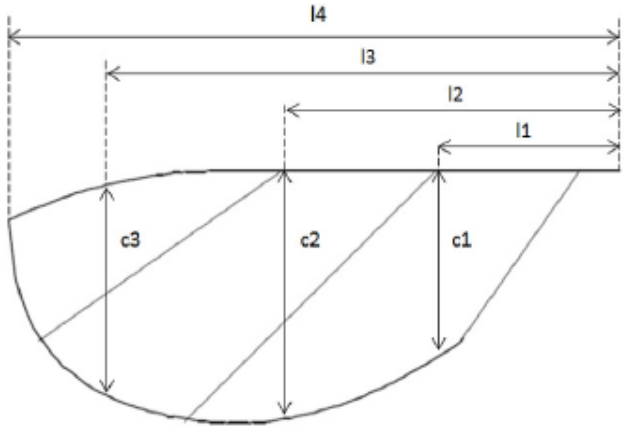

Fig. 23 Sketch of the wing planform with dimension indications. The values of the parameters can be found in Table 5.

span (%)	chord (mm)	length (mm)
25	c1 = 14.5	l1 = 13.5
50	c2 = 19.5	l2 = 25.5
80	c3 = 17.0	l3 = 38.0
100	c4 = 0.00	l4 = 47.5

Table 5: wing dimensions

The PIV measurement setup

Fig. 24 shows a schematic top view of the experimental setup. The flapping mechanism is positioned at the outlet of a small wind tunnel with a uniform outlet velocity of approximately 1 m/s and a turbulence intensity of less than 0.2%. The fluid flow around the wing of the robotic hummingbird and the induced wake by the wing's kinematics are measured using Time-Resolved Particle Image Velocimetry. This technique is a non-intrusive and optical method as it measures the velocity of small seeding particles in the flow by laser illumination. The Di-Ethyl-Hexyl-Sebacat (DEHS) seeding particles are generated by a Palas type AGF 10.0 Liquid Nebulizer. The particle diameter is between 0.2 and 1 µm with a median diameter of 0.35 µm, which ensures that velocity fluctuations up to 8 kHz can be followed by the largest particles and that 50% of them can follow fluctuations up to 67 kHz [Melling, 1997].The laser sheet generated by a Dual Cavity Nd:YLF Pegasus laser from NewWave has a thickness of 0.5 mm. The wavelength of the light is 527 nm and the pulse energy is 10 mJ at 1000 Hz. A single

'HighSpeedStar 5' camera of 1024 x 1024 pixels is used to capture the images. The sampling frequency of the system is 3000 Hz. The images are processed using Davis 7.2 and further in-house developed software is used for vector field processing.

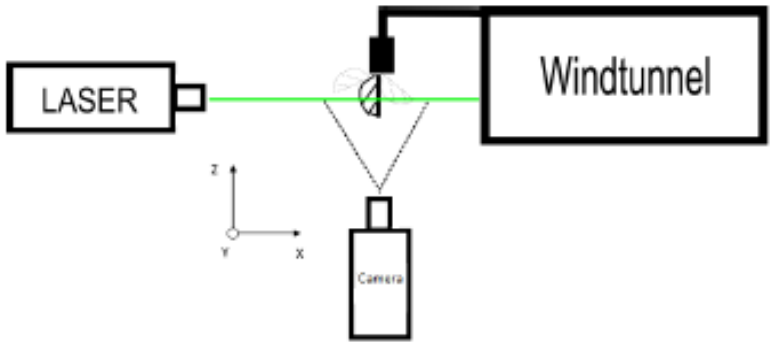

Fig. 24: Schematic view of the experimental flow setup**. The laser sheet is shown in green.**

The velocity of the flow field can only be measured in one plane at a time with the PIV measurement set-up described above. To have a better understanding on the flow variation with the span-wise direction of the wing, PIV measurements are taken of four chord wise cross-sections of the wing (measured from the wing root): at 25% of the wing length, at 50%, at 80% and at 102%. Table 5:6 lists the chord lengths at the first three span wise distances of the wing. To have a better understanding of the flow variation during the wing motion PIV measurements are taken at eight different phases during the wing motion as shown in Fig. 25: four measurements are taken in forward stroke and four in backward stroke. At each of these eight positions the four chord-wise cross sections at different span-wise positions of the wing (as described above) are measured.

To set the measurement plane, the flapping mechanism is mounted on a position mechanism which consists of two stages: one Misumi rotary stage (RPGE 25) and one Misumi linear stage (XDTS90). A change of the angle of the rotary stage with respect to the vertical axis changes the recorded phase angles of the cycle. A change of the position on the linear stage results in a measurement of a different chord wise section. Fig. 25 shows an overview of all 24 configurations.

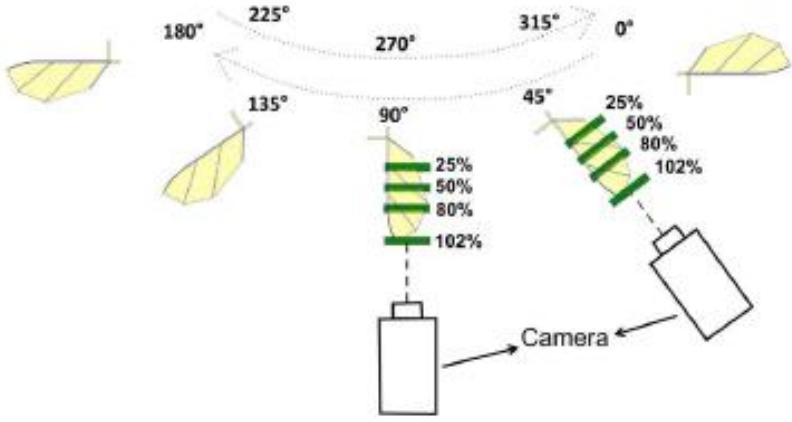

Fig. 25: **Schematic representation of measured configurations.** Several measurements are taken at various span wise locations of the wing (25%, 50%, 80%, and 102%) and at various phases of the wing motion**. T**he green line depicts the measurement plane.

Force and position measurement setup

To conduct the force measurements, the structure of the flapping mechanism is connected to a single point load cell as shown in Fig. 22. The load cell is a model 1668(S) from BCM with a capacity of 1 N. The RMB20PC magnetic encoder module from RENISHAW is used for the position measurement of the wing. This is a digital encoder with an absolute binary parallel interface. Fig. 22 shows the magnet which is attached to the driving axis of the wing and the magnetic encoder is positioned below this magnet. The load cell is connected to the CPJ module from SCAIM to amplify the output voltage of the load cell and it contains also a second-order low-pass filter with a 10 Hz cut-of frequency. The output from the CPJ module is connected to an analogue input terminal of the 'USB-6229 BNC'-module from National Instruments. This setup has a resolution of 0.5mN. This module allows further processing of the signal and this module is connected to a computer for further processing. 'LabVIEW Signal Express' is used for the acquisition of both sensor signals. To achieve a sufficient accuracy of the position measurement the sample frequency is 8000, which corresponds to 228 measurements every flapping cycle.

Calculation of the thrust generated by the wing motion by flow analysis

The wake of the wing is turbulent. To separate the small, random induced structures by turbulence from the large-scale periodic structures induced by the flapping, the Eulerian Time Filtering (ETF) technique is applied, as developed by Vanierschot et al. [Vanierschot et al, 2009]. This method was originally developed for the extraction of periodic structures in an annular jet. It also works very well for flapping wings, which

generate periodic flow structures too. After Eulerian Time Filtering, the data are phase-averaged to remove any small-scale structures which may be left. To calculate the forces from the measured velocity field, a method developed by [Noca et al, 1997] is mostly used in literature. In this method, the sectional thrust is calculated as:

$$\mathbf{F}' = \boldsymbol{\rho} \int_A \boldsymbol{u} \times \boldsymbol{\omega} dA - \boldsymbol{\rho} \oint_S \boldsymbol{n} \cdot \boldsymbol{u}(\boldsymbol{x} \times \boldsymbol{\omega}) dS + \oint_S \boldsymbol{n} \cdot [\boldsymbol{x} \cdot (\boldsymbol{\nabla} \cdot \boldsymbol{T})\boldsymbol{I} - \boldsymbol{x}(\boldsymbol{\nabla} \cdot \boldsymbol{T}) + \boldsymbol{T}] dS \qquad eq. 3.1$$

where A is an area enclosing the wing cross section at a fixed span wise location, S is the boundary of this area, **u** is the velocity vector, **x** is the position vector, **ω** the vorticity vector, **T** is the shear stress tensor and **I** is the unit tensor. The calculation of equation 3.1 requires spatial derivatives of measured quantities which are measured at discrete time steps. The procedure of numerical differentiation introduces significant errors. Here we propose an alternative procedure which is based upon integration instead of differentiation and which produces a much more stable result. The momentum equation is integrated over a control volume at a fixed span wise location. It is based on the Reynolds transport theorem. If pressure and shear forces are neglected (the control volume should be sufficiently large compared to the wing) the force of the wing on the fluid is given by

$$F_y = \frac{\partial}{\partial t}\left[\int_\Omega \rho V_y dV\right] + \int_{\partial\Omega} \rho V_y \boldsymbol{V} \cdot \boldsymbol{dA} \qquad eq. 3.2$$

where F_y is the vertical component of force on the fluid, ρ is the fluid density, V_y is the vertical component of velocity, A is the normal vector of the edges of the control volume and V is the volume. Equation (3.1) as well as equation (3.2) reduces to the theorem of Kutta-Joukowski for stationary flows, which has been frequently applied for the calculation of the thrust force on flapping wings [Birch et al, 2004], [Ramsey, 2011], [Tian & Iriarte-Diaz, 2006]. For the 2D integration in this study, all quantities are taken per m, e.g. the unit of F_y is N/m.

RESULTS

The leading edge vortex

Fig. 26A and Fig. 26B show the measured velocity field and vorticity field at a chord-wise measurement plane which is located at 50% span. The measurements are taken at a phase angle of 90°. At this phase in wing motion, the wing is moving from the right of the figure to the left. Its wing section is represented by the black line segment, with an angle of attack of approximately 30°. A distinguished leading edge vortex (LEV) is present above the wing section, which is identified in the vector fields as well as in the vorticity contours. Similar results are found at other span-wise positions. However, the

size and strength of the LEV at different span-wise positions change. Size and strength of the leading edge vortex increase from the wing root up to about 50% span.

At cross-sections between mid-span and the wing tip, the tip vortex interacts with the leading edge vortex structure and its strength decreases. The vector plot clearly shows that the wing produces a strong, concentrated downward flow. The maximum averaged velocities in the downwash reach 5 m/s but instantaneous velocities of 10 m/s have been measured. The downward momentum associated with this downwash is the main contribution in equation 3.2 to the thrust force which is generated.

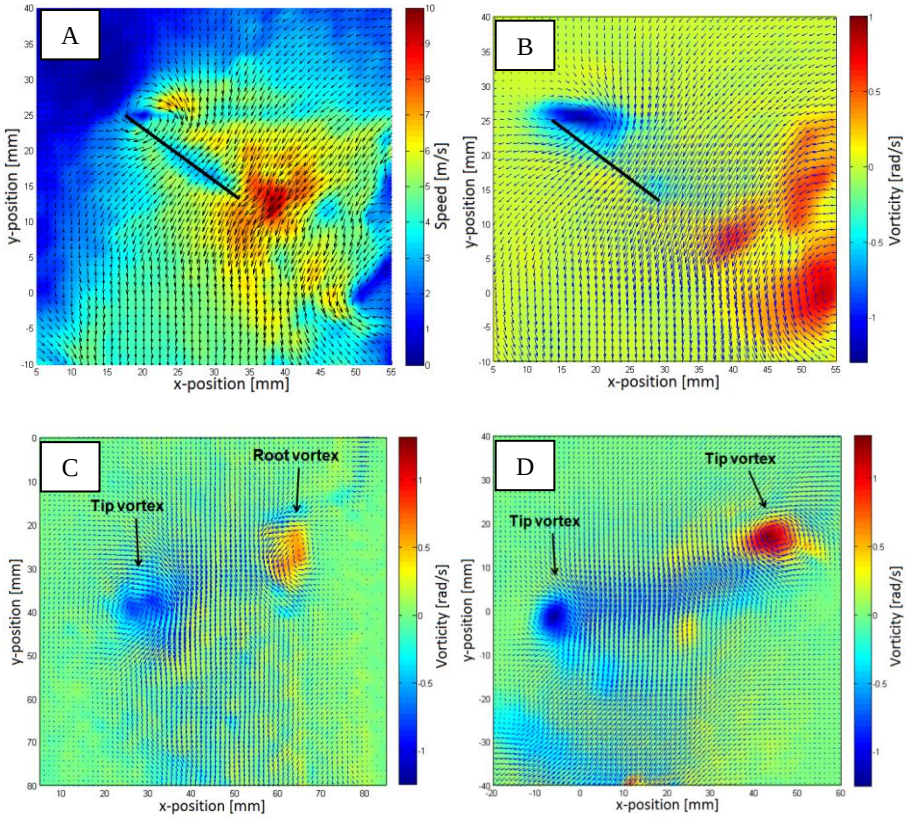

Fig. 26 (A) Instantaneous vector field (arrows) and instantaneous velocity magnitude (contours) of the flow of a flapping wing at 35 Hz flapping frequency and phase angle Ψ = 90° (the wing is moving from right to left) at 50% of span. For the same measurement figure (B) shows the instantaneous vector field (arrows) and instantaneous vorticity magnitude (contours). C&D show the vortical structures in the wake for a flapping frequency of 35 Hz. The phase angle of the motion Ψ is 0°. (C) a span wise measurement section. (D) a chord wise measurement section (80% span).

Elliptically shaped vortex loops in the wake

To identify the vortical structures of the wake, PIV measurements in a span-wise and in a chord-wise plane at a phase angle of 0° are analysed. The phase angle corresponds to the beginning of the wing's motion. The results are shown in Fig. 26. The velocity field in a span wise plane, shown in Fig. 26c, shows two counter rotating vortices. These counter rotating vortices are also seen in a chord wise plane (Fig. 26d). These vertical structures, together with the strong downwash have also been found by Warrick et al. **[Warrick et al, 2005]** who studied the vortical structures in the wake of a hovering hummingbird. The results in Fig. 26 also confirm the proposed model for the principal vortex wake structures of hovering Anna's hummingbirds (Fig. 27) by Altshuler et al. **[Altshuler et al, 2009]**. This study states that vortex loops are shed during wing rotation. These vortex loops have an elliptical shape, being longer in the ventral dorsal (in this study the x-axis) than the lateral- medial axis (in this study the z-axis).

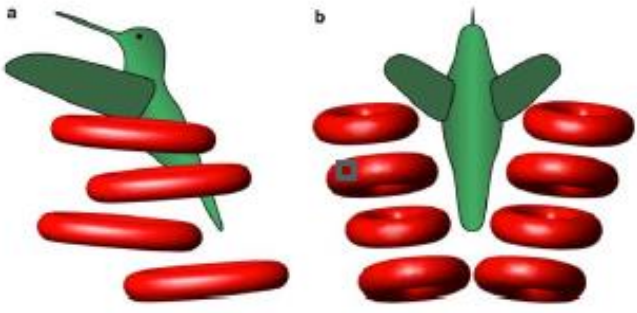

Fig. 27 **Toroidal Vortices:** Model postulated by Altshuler et al. for the formation of toroidal vortex structures. a) Lateral perspective on the vortex structures in the downwash of a hummingbird. b) Dorsal perspective on the vortex structures in the downwash of a hummingbird. **[Altshuler et al, 2009]**

Thrust

Fig. 28 shows the thrust profile on the wing for a flapping frequency of 35 Hz and phase angles $\Psi = 90°$ and $\Psi = 270°$. The maximum sectional thrust force occurs near the cross-section at 50% span. In this region the leading edge vortex is the strongest and also the chord length is large. When taking together all individual effects, this results in a high aerodynamic sectional thrust force. Results by Birch et al. show similar thrust profiles **[Birch et al, 2004]**. Maximum contribution to thrust is found to take place at about 60% span. This is slightly closer to the wing tip than in this study, but we have measured only four discrete sections.

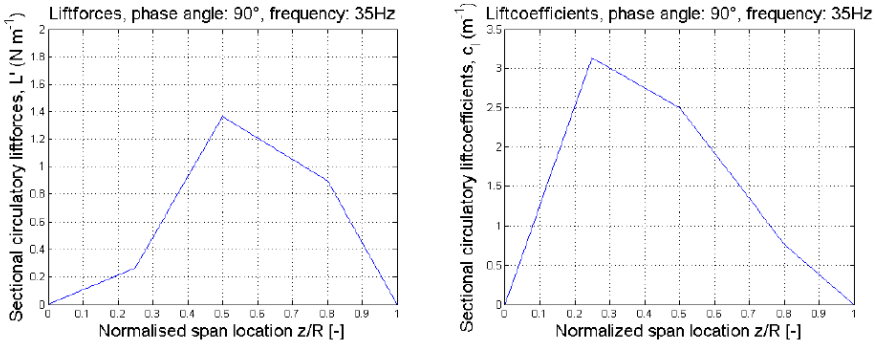

Fig. 28: thrust coefficient profile along the span wise direction of the wing for a flapping frequency of 35 Hz. The phase angle of the motion Ψ = 90°. (a) Sectional circulatory thrust force. (b) Sectional circulatory thrustcoefficient.

A very rough estimate for the thrust force is calculated by integration of the profiles in Fig. 28 in the span-wise direction. As there are only three measurement locations in the span wise direction, cubic spline interpolation is used for intermediate locations. Integration over the entire wing span gives values of 3.1cN for Ψ = 90° and 4.5cN for Ψ = 270° (1 centiNewton corresponds to 1 gram at 1g). Although these estimates are in the same order of magnitude as the direct measurements of the average thrust force which are reported in the next section, they should be interpreted with some care. To have better estimates, measurements at more locations are required.

Fig. 29 shows a simultaneous measurement of the average thrust force (measured with the load cell) and the stroke motion (measured with the magnetic encoder) for a flapping frequency of 35 Hz. Because the exact phase between both measurements signals is unknown and the force measurement is filtered as described above, no conclusions about the instantaneous thrust can be drawn from these measurements. The average thrust is 3.5cN, which is of the same order of magnitude as the average thrust estimated from the PIV-measurements. The position signal in Fig. 29 shows that the stroke motion of the wing can be approximated closely by a sine function. The stroke amplitude is 171°. The time intervals for the forward and backward stroke are respectively 0.0149 s and 0.0136 s. As the period of the backward stroke is approximately 10% shorter compared to the forward stroke, the average angular velocity during backward stroke is higher. As a consequence the thrust generated during the backward stroke is expected to be larger than the thrust generated during the forward stroke. This observation is confirmed by the thrust estimated from the PIV-measurements. (3.1cN during forward motion versus 4.5cN during backward stroke at Ψ =90° and 270° respectively.

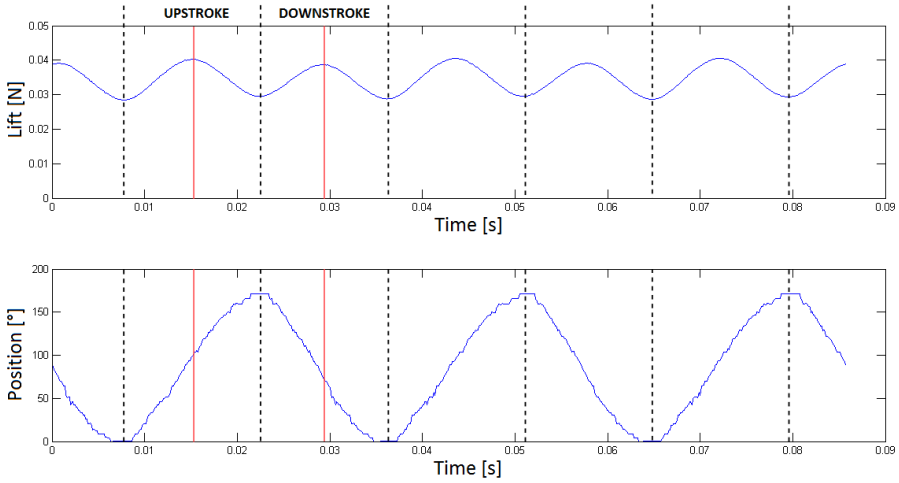

Fig. 29 Force and position measurements for flapping frequency 35 Hz and sampling frequency 8 kHz, with filter.

In order to study if the flapping wing benefits from the wake capture effect, a horizontal measurement was taken just after the pronation phase of the wing. Fig. 30 shows an instantaneous top view of the vorticity field. The wing is just starting its backward stroke to move to the left of the image. The flow that approaches the wing has a direction opposite to the wing motion due to the previous forward stroke. This shows that the flapping wing benefits from the wake-capture effect.

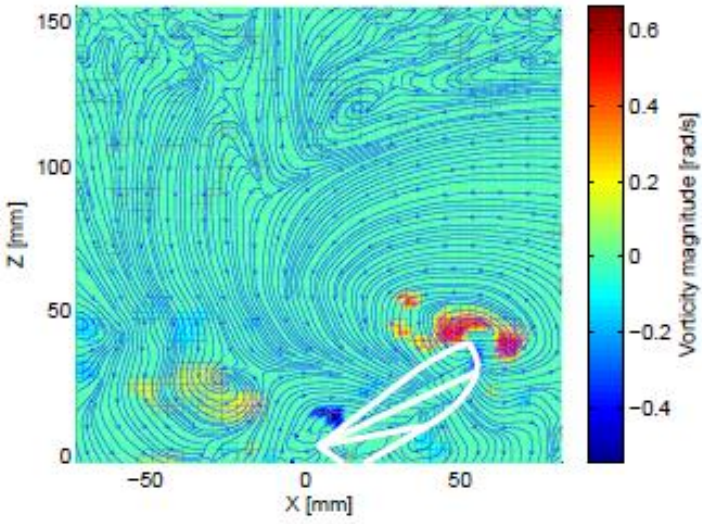

Fig. 30: Visualization of the wake-capture effect (top view). The flapping wing has just gone through pronation and it is starting its backward stroke to move towards the left of the image. The flow which approaches the wing has a direction opposite to the wing

CONCLUSIONS

The flow field around a high-frequency, high-amplitude flapping wing is measured and visualized by time-resolved Particle Image Velocimetry (PIV). Both a leading edge vortex and the wake-capture effect are observed. The large-scale periodic structures in the wake are extracted by the Eulerian Time Filtering method. Analysis of the results confirms the hypothesis that ring shaped vortices are shed by the wing during upstroke and down stroke, which is also confirmed by other studies. An estimate for, the total thrust force on the wing is calculated from the velocity field by integration of the momentum equation. The forces are validated by instantaneous position and force measurements using a load cell. The calculated thrust force is in the same order of magnitude as the measured thrust force.

3.3.2 VISUALISATION OF THE 3D FLOW AROUND A FLAPPING WING BASED ON 2D PIV MEASUREMENTS

RESEARCH OBJECTIVES

The aim of these experiments is to visualise the 3D flow field around a flapping as a 3D-vector field by recombining 2D-velocity vector fields taken from different viewpoints.

The wing has a length of 60mm length and it flaps at a frequency of 25.8Hz, a relatively small stroke amplitude of about 102° and an angle of attack of 45°. The wing is driven by one of the first and unfortunately worst performing versions of the resonant flapping wing mechanism. The research objective of visualizing the flow around a flapping wing of the Kulibrie as a 3D-vector field by recombining 2D-velocity vector fields is not met due to limited time and resources. The research however produced an interesting result, showing a small but considerable horizontal component of the flow that could explain why a figure of eight wing tip motion could generate slightly more thrust than a fully horizontal wing tip motion as is generated by the robotic hummingbirds listed in Table 1.

MATERIALS AND METHODS

The PIV measurement setup

The PIV measurement setup is the same one as described above, with the same settings.

The wing

The wing is a mylar foil which is stiffened by thin carbon composite tubes (see Fig. 31) It has a length of 60mm and a maximum chord of 25mm.

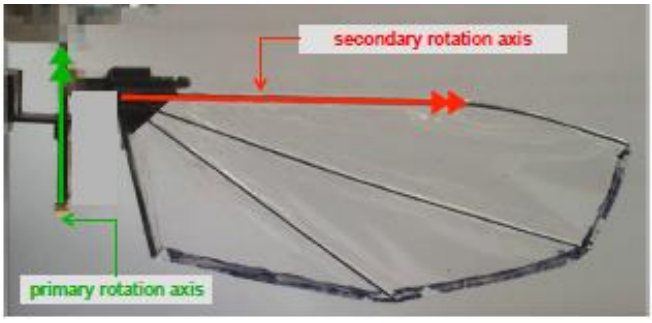

Fig. 31 A picture of the wing used in the second set of PIV measurements.

The wing motion and the flapping mechanism

The wing is driven by the resonant flapping wing mechanism shown in Fig. 32. The stroke amplitude is estimated roughly using a protractor. (the stroke amplitude is visible by the naked eye)

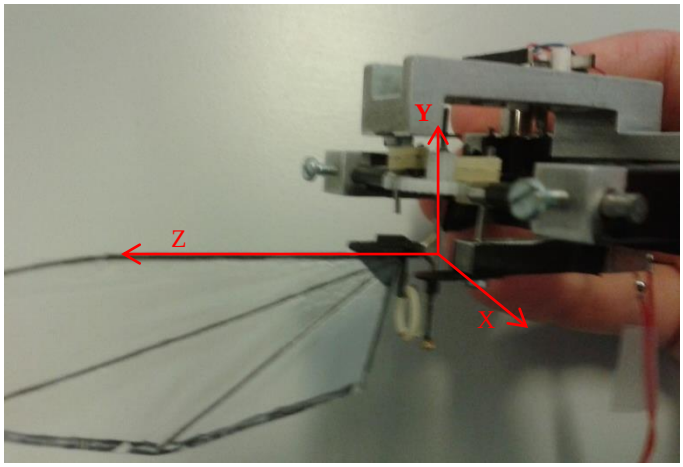

Fig. 32 **Definition of the used coordinate frame**. The origin lies at the intersection of the primary and the secondary rotation axis. The X-axis points towards the wind tunnel. The Y-axis coincides with the primary rotation axis. The –axis coincides with the leading edge when the wing is in the neutral position.

The PIV measurement setup

The planar PIV set-up that is used can only measure the velocity of the flow in one plane. In order to create a 3D representation two sets of perpendicular planes are measured. At the intersections of these planes a 3D velocity vector is reconstructed in a post-processing step. Fig. 33 shows the chord-wise (vertical) measurement planes and the X- and Y- axes of the coordinate frame. The Z- axis points towards the observer. Fig. 34 shows the span-wise (horizontal) measurement planes, here the Y- axis points away from the observer.

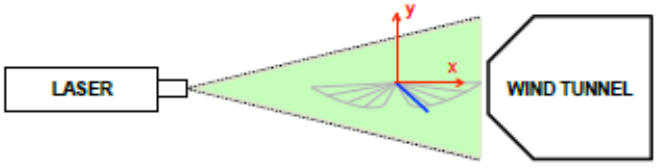

Fig. 33 Camera view of the PIV setup for the measurement of vertical planes. The wing is shown in blue. The grey wing positions show the extreme positions.

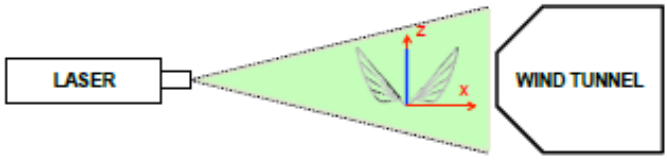

Fig. 34 Camera view of the PIV setup for the measurement of horizontal planes. The wing is shown in blue. The grey wing positions show the extreme positions.

In total 13 chord-wise (vertical) and 8 span-wise (horizontal) measurements are done. The measurements are repeated in order to increase the measurement reliability.

RESULTS

Fig. 35 shows the existence of a Leading edge vortex and an intersection of the same elliptically shaped vortex loops in the wake of the flapping wing as described above. These images show more subsequently shed vortex loops. It is clearly visible that the vortex loops which are shed during pronation are oriented differentially than the ones shed during supination.

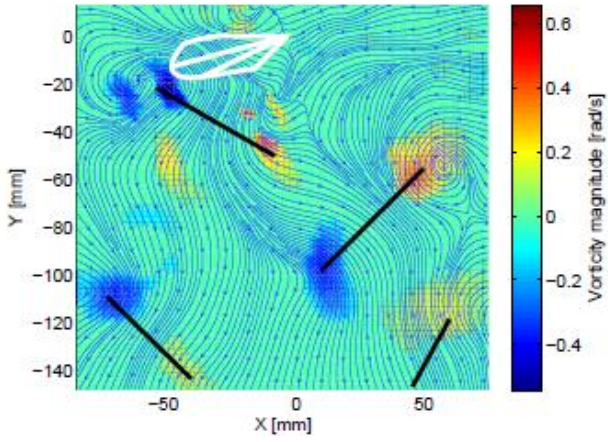

Fig. 35 The averaged velocity field over all 39 classes. There is a clear downwash visible. The zone of downwash to the left is mostly generated by the positive stroke. The downwash in both halves of the images has an X-component. As the production of the downwash is a prerequisite to produce thrust, the thrust can be increased by eliminating the X-component of the downwash.

Because the wing flaps in the horizontal XZ- plane without a Y- component of the wing motion (deviation) the TEV (trailing edge vortex) is shed earlier than the LEV. As a consequence, the TEV has already travelled a certain distance until the LEV is shed. The inter vortex flow, which takes place between the LEV and TEV, has a relatively small, but significant X- component. This X-component is observable in Fig. 3638 that shows the averaged velocity field. In this figure a clear down wash is visible. The zone of downwash to the left with the negative X-component is mostly generated by the forward stroke and the one on the right with the positive X-component by the backward stroke.

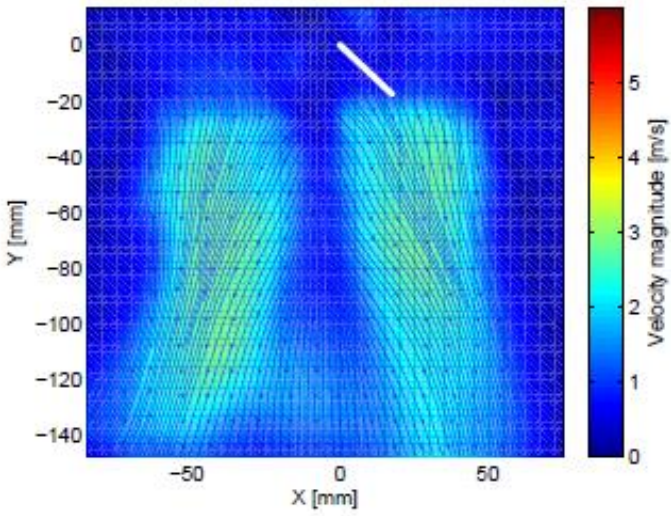

Fig. 36 Average velocity field for one flapping cycle of vertical plane 2. The zone of downwash to the left is mostly generated by the negative stroke and the one on the left by the positive stroke.

The thrust generated by the wings can probably be enhanced by eliminating the x component of the downwash. A possible strategy may be the implementation of a deviation from the stroke plane that results in a figure of eight wing tip trajectory. The current situation is shown in Fig. 37A. from a chord wise view.

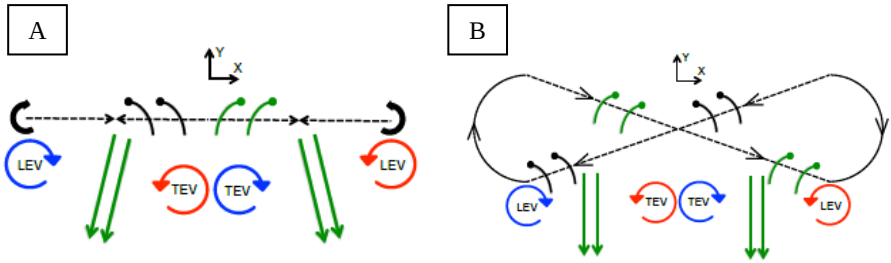

Fig. 37 (A) Chord wise view of the current wing motion of the Kulibrie. There is no motion in the vertical y direction. The TEV has travelled a certain distance until the LEV is shed. (B) Chord wise view of the true motion of a hummingbird wing. The LEV is shed lower in comparison with (A)

Fig. 37B. shows the same motion, but with the implementation of a deviation from the stroke plane that results in a figure of eight wing tip trajectory. The figure shows that the supination and pronation now start lower and end higher in comparison to the plane wing motion. As a consequence the LEV and the TEV are at the same height when the LEV is shed. This creates a purely downward airflow, which is expected to increase thrust. In this case the wing pushes the air forward and slightly downwards, enhancing the downwash.

3.4 EXPERIMENTAL PARAMETER STUDY OF THE INFLUENCE OF THE WING MOTION AND THE WING SIZE AND SHAPE ON THE AVERAGE THRUST GENERATED BY A HUMMINGBIRD-LIKE FLAPPING WING USING A RESONANT FLAPPING MECHANISM

3.4.1 INTRODUCTION

Objective

The average thrust generated by a hummingbird-like flapping wing is one of the most important design considerations in the development of a robotic hummingbird. It limits the mass of a robotic hummingbird, which in turn limits the size and the power of the actuators, the size and the energy capacity of the battery and the mass and sensing opportunities of the avionics.

With a prescribed wing size, the average thrust generated by a hummingbird-like flapping wing depends on several parameters that govern the wing motion and the morphology of the wing. It is of critical importance to maximize the average thrust that can be generated by a hummingbird-like flapping wing through a selection of the optimum values for each parameter.
This section describes a parameter study for five parameters that govern the wing motion, morphology and size of a hummingbird-like flapping wing: the flapping frequency, the stroke amplitude, the angle of attack, the aspect ratio and the wing size, defined by its length.

The data set obtained by the measurements provides useful information to improve and validate numerical models.
The prescribed wing motion is the simplified wing motion as explained in section 2.4.2 and used by all the flapping wing micro air vehicles listed in Table 1. The results show that this proposed simplification of the hummingbird's wing motion generates more thrust than a hummingbird wing of the same size for the same flapping frequency and stroke amplitude. A possible explanation for this observation is the symmetric wing motion allows a leading edge vortex stabilisation both during forward as during backward stroke, while a hummingbird only takes advantage of a leading edge vortex stabilisation during forward stroke [**Warrick et al, 2005**].

State of art

Little experimental data are available that relate the average thrust generated by a hummingbird-like flapping wing to its wing motion, morphology and size **[Phillips & Knowles, 2011]**. This lack of experimental data is not surprising given the challenge of designing a lightweight mechanism that is able to generate a simplified hummingbird-like wing motion with both a large stroke amplitude and a high flapping frequency. The challenge becomes even bigger if the mechanism has to be able to vary several kinematic parameters in a broad range. The resonant flapping mechanism that is used here is described in detail in chapter four. It allows to readily vary both the stroke amplitude and the flapping frequency without the need of a complex mechanical system. Furthermore both parameters are varied continuously, during operation and in a broad range.

In addition, the wing motion has to be measured too. Different researchers have used one or more high speed cameras that track the wing motion **[Leys, 2011], [Whitney & Wood, 2010]** and **[Wu et al, 2009]**. Many points on the flexible wing can be tracked so that not only the rigid body motion but also the deformation of the wing can be measured. This method however is very time consuming and the data of the wing motion are only known after a full image analysis. The data can therefore not be used in a feedback loop to set kinematic parameters to a desired value. A novel contactless measurement method is used here to measure the stroke angle with a MEMS magnetic encoder. The data from this encoder are used to set the stroke amplitude to a desired value.

3.4.2 MATERIALS AND METHODS

The wings

Seven different wings are used in the experiments. Table 6 summarises the most important characteristics of these wings. To study the influence of the wing size, five wings of different lengths are manufactured that have the same wing shape as shown in Fig. 38. The distance between the root of the wing and the stroke axis is 8mm.

To study the influence of the aspect ratio, two wing variants (80_S and 80_L) have the same length as wing 80_M, but a different aspect ratio. The shape of these two wings is obtained by scaling the shape shown in Fig. 38 respectively at 80% and at 120% of the reference value, but only in the chord-wise direction.

Because the diameter of the wing veins (black carbon fibre rods) and the membrane is the same for all wings, the relative wing stiffness increases with decreasing wing size.

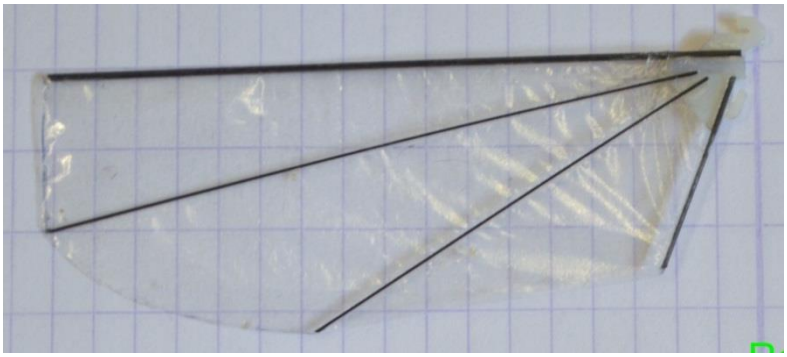

Fig. 38 The wing: The wing has a length of 80mm and is an assembled of carbon fibre composite rods (stiffeners) and a Mylar membrane.

The flapping mechanism

Fig. 39 shows the resonant flapping mechanism and the measurement set-up. The flapping mechanism is mounted on a double beam load cell which measures the thrust generated by the flapping wing. A small magnet is fixed to the stroke axis and it is used for the contactless measurement of the stroke angle with a magnetic position sensor. The flapping mechanism is described in detail in chapter 4.

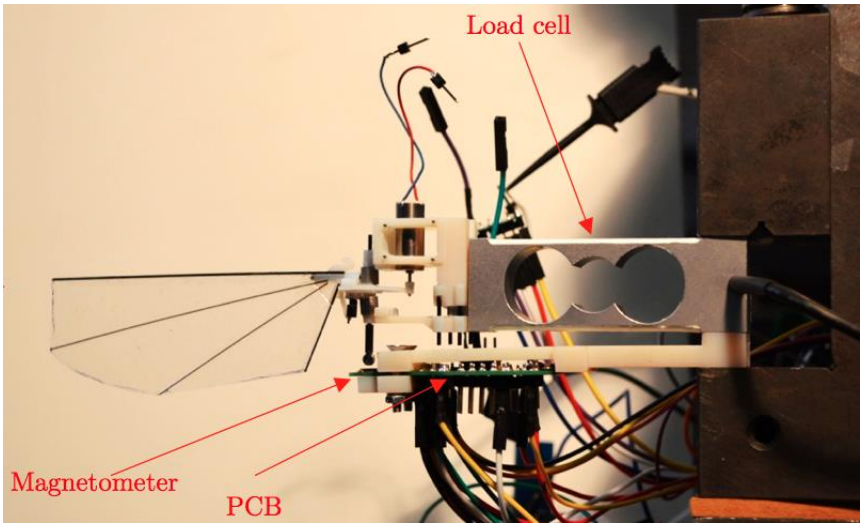

Fig. 39 **The resonant flapping mechanism and the measurement set-up:** The flapping mechanism is mounted on a double beam load cell which measures the thrust generated by the flapping wing. A small magnet is fixed to the stroke axis and it is used for the contactless measurement of the stroke angle with a magnetic position sensor.

The wing motion

The wing motion which is prescribed in the test set-up is the simplified wing motion of a hummingbird (see section 2.4.2). Three kinematic parameters of this motion are set independently: the flapping frequency, the stroke amplitude and the angle of attack. Angular velocity in the stroke motion is controlled during flapping by changing the frequency of the AC current through the motor. The desired frequency is set by a feed-forward controller. Table 6 shows the different flapping frequencies that are used in the experiments, ranging between 20Hz and 32Hz in steps of 1 Hz. The stroke amplitude is set as a variable kinematic parameter during flapping by changing the amplitude of the AC current through the motor after feedback control based on the output of the magnetic encoder. Table 6 shows the different flapping frequencies that are used in the experiments, ranging between 120° and 180° in steps of 10°.

The angle of attack cannot be changed during a flapping cycle but it is set as a fixed limit in advance by integrating a blocking element that limits the maximal angle of attack. Table 6 shows the different angles of attack that are used in the experiments, ranging from 35° to 60° in steps of 5°.

wing length (mm)	60	70	75	80_S	80_M	80_L	85
mean geometric chord (mm)	19	22	23	20	25	30	27
aspect ratio	3,2	3,2	3,2	4	3,2	2,7	3,2
mass (g)	0,1	0,12	0,13	0,12	0,14	0,17	0,15
inertia around stroke axis (gmm^2)	68	115	146	182	187	192	225
flapping frequencies (Hz)	22-34	22-32	21-31	20-30	20-30	20-30	20-28
stroke amplitude (°)	120, 130, 140, 150, 160, 170, 180						
angle of attacks (°)	35, 40, 45, 50, 55, 60						

Table 6 **The parameters varied in the experiments**: 7 different wings were subject of the experiments. For each wing, the stroke amplitude, angle of attack and frequencies are varied. The frequency is varied in steps of 1Hz.

The measurement setup

Fig. 40 shows a schematic representation of the measurement set-up. Four quantities are measured: the average thrust (T) generated by the wing, the stroke angle (θ), the current (A) through the actuator [M] that drives the wing and the voltage (U) over this actuator. A *Labview* based graphical user interface is developed to visualise the stroke amplitude and the average thrust generated by the flapping wing. This graphical user interface is also used to set the flapping frequency and the stroke amplitude. A digital analyser (*Saleae Pro 8*) records the time courses of the current, voltage and stroke angle. The measurements of the current (A) through the motor [M] that drives the wing and the voltage (U) over this motor are used to measure the power consumption and they are described in detail in chapter 4.

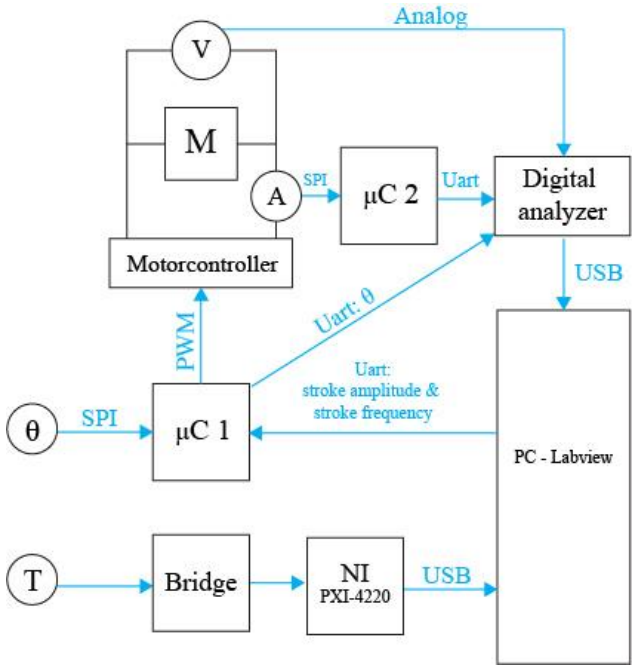

Fig. 40 A schematic diagram of the measurement setup: Four variables quantities are measured: the average thrust (T) generated by the wing, the stroke angle (θ), the armature current (A) through the motor [M] that drives the wing and the armature voltage (U) over the motor

Measurement of the stroke angle (θ)

The stroke angle (θ) is measured using a contactless magnetic position sensor from AMS (AS5055A) schematically represented as (θ) in Fig. 40 A custom PCB is designed to connect the magnetic position sensor with the microcontroller. The magnetic position sensor measures only 4mm by 4 mm by 0.8mm and it is small and light enough to be built in a robotic hummingbird (see chapter 6). This sensor measures the rotation of the stroke axis by sensing the magnetic field of a small magnet attached to the stroke axis. The measurement sensitivity is 0.088° resulting from a 12bit discretisation of the 360° measuring range. The stroke angle is measured 2^6=64 times per flapping cycle regardless of the flapping frequency.

The magnet is attached to the stroke axis as shown in Fig. 39 and it has a cylindrical shape with a radius of 1mm and a height of 1mm. Its inertia around the stroke axis is $2.4 \cdot 10^{-3} gmm^2$ which is insignificant compared to the inertia of the wings.

Before measurements are done, the sensor is calibrated in order to define the stroke angle to be zero if the wing is at mid stroke. The raw measurement data, in the form of a 12bit integer number, is first converted to a stroke angle θ between -180° to 180° by an algorithm programmed on microcontroller1 (μC1 in Fig. 40). Although the stroke angle can be measured in a range of -180° to 180° in practice the stroke amplitude is kept to a maximum of 180° which matches stroke angle from -90° to 90°.

The stroke amplitude (Ω) is derived from the measured stroke angle data by the following algorithm (3.1) programmed on microcontroller1:

$$\Omega = \frac{\sum_1^{64} \theta_i}{40.71} \qquad 3.1$$

The constant 40.71 is related to the number of measurements per flapping cycle. Here there are 64 measurements of the stroke angle per wingbeat cycle.
The measurement of the stroke amplitude is used in a proportional feedback loop, programmed on microcontroller1 to set the stroke amplitude to a desired value.

Measurement of the flapping frequency (f)
The flapping frequency is the frequency of the cosine signal generated by microprocessor1. This cosine signal is a discrete signal with a short time delay in between each step. Frequency changes with the time delay. By using a strobe, the delay matching the desired flapping frequencies can be measured in advance and used in a feedforward controller.

Measurement of the average thrust (T)
Thrust is measured using a common double beam strain gauge load cell of BCM (model 1668S) as shown in Fig. 39. The load cell is connected to a *Scaime* CPJ measurement bridge with built-in amplifier. The measurement sensitivity of the thrust measurement is 0.5mN. The thrust is measured at 1200 Hz and averaged over a period of 1 second.

3.4.3 RESULTS AND DISCUSSION

A total of 740 experiments are performed. A summary is shown in Fig. 41 to Fig. 44. Each figure shows the influence on generated average thrust of one the five different parameters that are set as a variable: the flapping frequency (Fig. 41), the stroke amplitude (Fig. 42), the angle of attack (Fig. 43) and the wing size (Fig. 44). In each of these figures the power consumption (see chapter 4) is represented by a dotted line while the thrust is represented by a solid line. Thrust is expressed in cN as the numerical value corresponds to the mass in grams that is lifted by that thrust level in hovering flight. Each measurement point is represented by a thick mark on the horizontal axis. In each graph

two parameters are varied: one on the horizontal axis and one that is distinguished by colour. For the convenience of the reader, the parameters that are kept constant are also shown in the text box in the upper left corner of each graph.

The influence of the flapping frequency

Fig. 41 shows the influence of the flapping frequency on the average thrust respectively for three different values of stroke amplitude, three different values of angle of attack, three different values of wing size and three different values of aspect ratio. The blue lines in Fig. 41A, Fig. 41B, Fig. 41D and the green line in Fig. 41C represent the same measurements.

According to a quasi-steady aerodynamic model **[Timmermans, 2016]** the thrust should increase with the square of frequency f. The results clearly show that in practice this is not the case. If each curve in the figure is fitted with an exponential function of f, the exponent is considerably lower than 2. Another observation is that thrust does not always increase with increasing flapping frequency, but in some cases it decreases with frequency as marked for example by the green curve in Fig. 41A.

Both observations can be explained by the wing twist which increases if the load on the wing increases as is observed by using a stroboscope. The increased wing twist results in a decreased average angle of attack. This means that in practice each wing can generate no more than a maximum amount of thrust (T_{max}), regardless of the stroke amplitude and flapping frequency.

Fig. 41B shows that a larger angle of attack at the wing root increases the maximum thrust that can be generated by a wing. Increasing the angle of attack too much however, increases the power significantly. The optimum angle of attack depends on the stiffness of the wing. More research is necessary to identify the best combination of wing stiffness and angle of attack for a particular wing.

Fig. 41C shows that a smaller wing, generates less thrust. Furthermore, the difference between the thrust generation of the 50mm wing and the 60mm wing is larger than the difference between the 60mm wing and the 70mm wing.

Fig. 41D shows that the wing with the highest aspect ratio produces significantly more thrust without significantly increasing the power that is needed.

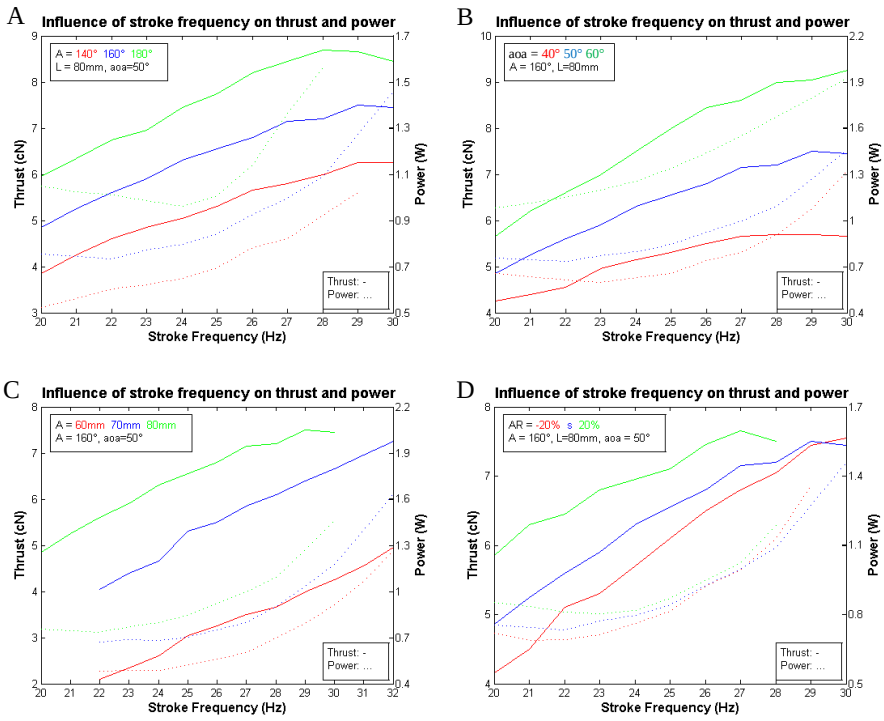

Fig. 41 **The influence of the flapping frequency on the average thrust:** The experiments are repeated for three different stroke amplitudes (A), three different angles of attack (B), three different wing sizes (C) and three different aspect ratios (D). The full line represents the thrust as measured and the dotted line represents the power consumption as measured. Each tick mark on the horizontal axis represents a measurement.

The influence of the stroke amplitude

Fig. 42A, Fig. 42B and Fig. 42C show the influence of the stroke amplitude (A) on the average thrust respectively for three different values of flapping frequency, three different values of angle of attack and three different values of wing size. The blue lines in Fig. 42A, Fig. 42B and the green line in Fig. 42C represent the same measurements.

According to a quasi-steady aerodynamic model **[Timmermans, 2016]** thrust should be proportional to stroke amplitude. The results show that the thrust indeed varies linearly with stroke amplitude in the range of interest.

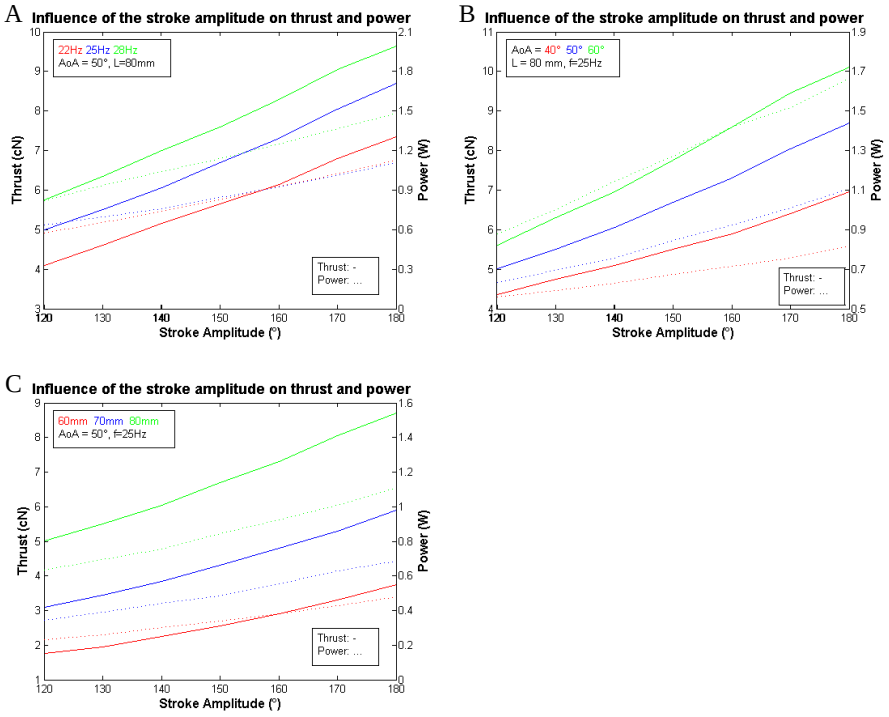

Fig. 42 **The influence of the stroke amplitude on the average thrust:** The experiments are repeated for three different flapping frequencies (A), three different angles of attack (B) and three different wing sizes (C). The full line represents the thrust as measured and the dotted line represents the power consumption as measured. Each tick mark on the horizontal axis represents a measurement.

The influence of the angle of attack

Fig. 43A, Fig. 43B and Fig. 43C show the influence of the angle of attack on average thrust respectively for three different values of stroke amplitude, three different values of flapping frequency, three different values of wing size and three different values of aspect ratio. The blue lines in Fig. 43A, Fig. 43B, Fig. 43D and the green line in Fig. 43C represent the same measurements.

According to literature the optimum angle of attack at which a maximum of thrust is generated is expected to be approximately 45°. The results however show that the optimum angle of attack does not lie within the measurement range of the experiments. The red curve in Fig. 43C shows that for a small wing the optimum angle of attack is smaller at approximately 50°. This observation is explained by the relative wing stiffness which increases with decreasing wing size

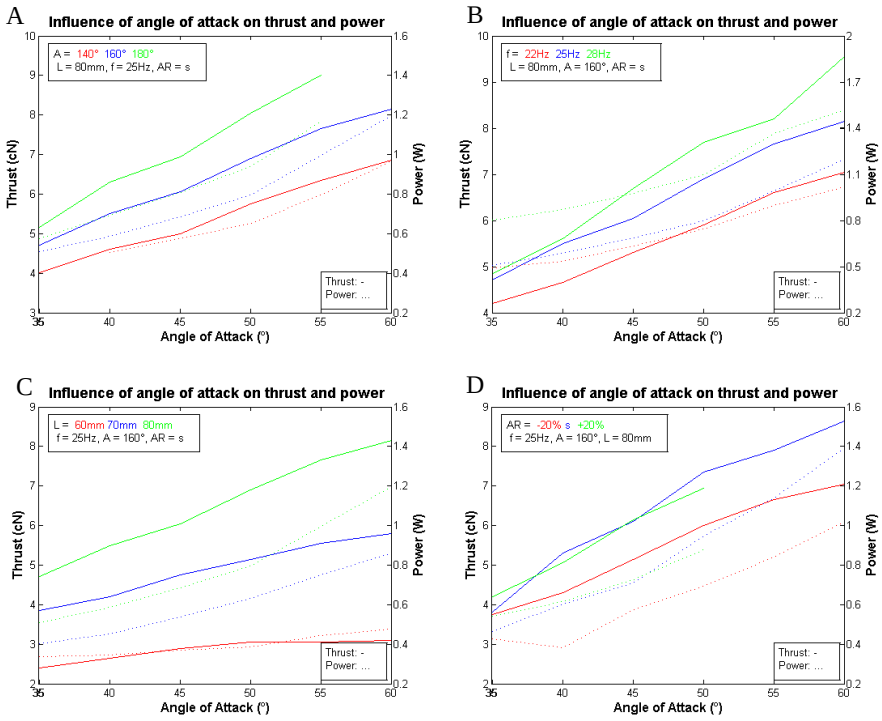

Fig. 43 **The influence of the angle of attack on the average thrust:** The experiments are repeated for three different stroke amplitudes (A), three different flapping frequencies (B), three different wing sizes (C) and three different aspect ratios (D). The full line represents the thrust as measured and the dotted line represents the power consumption as measured. Each tick mark on the horizontal axis represents a measurement.

The influence of the wing size

Fig. 44A, Fig. 44B, Fig. 44C and Fig. 44D show the influence of the wing size on the average thrust respectively for three different values of stroke amplitude, three different values of flapping frequency, three different values of angle of attack and three different values of aspect ratio. The blue lines represent the same measurements. The aspect ratio is only varied for wings with wing length 80mm. As a result the results for average thrust and power in Fig. Fig. 44D are represented by asterisks and circles respectively.

According to a quasi-steady aerodynamic model **[Timmermans, 2016]** the thrust varies linearly with the wing length. The results show that the relation between and wing length is approximately linear in the range of interest.

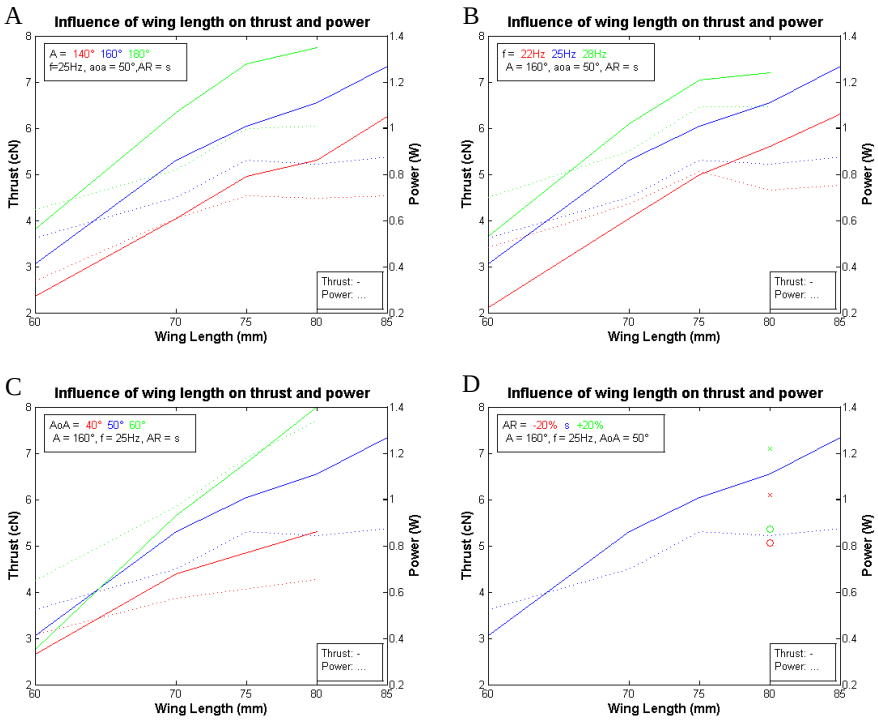

Fig. 44 **The influence of the wing length on the average thrust:** The experiments are repeated for three different stroke amplitudes (A), three different flapping frequencies (B), three different angles of attack (C) and three different aspect ratios (D). The full line represents the thrust as measured and the dotted line represents the power consumption as measured. Each tick mark on the horizontal axis represents a measurement.

Comparison of the thrust generated by artificial wings with the thrust generated by hummingbird wings

A robotic hummingbird which performs the simplified wing motion as described in chapter 2 has the potential to generate more thrust than its biological counterpart if the stroke amplitude, flapping frequency and wing size are set at identical values. After all according to Warrick **[Warrick et al, 2005]** hummingbirds only stabilise the leading edge vortex during forward stroke whereas a robotic hummingbird may stabilise the leading edge vortex both during forward and backward stroke.

Table 7 shows the thrust generated by hummingbird wings and the thrust generated by an artificial wing that performs the simplified wing motion. For this comparison the thrust generated by the hummingbird wing is assumed to be equal to the self-weight during normal hovering flight.

Wing length(mm)	60	70	75	80	85
Wing span (mm)	141	165	177	188	200
stroke amplitude normal (°)	160				
flapping frequency normal (Hz)	29	26	25	23	22
mass of the hummingbird (g)	5,4	7,3	8,3	9,4	10,5
thrust generated by hummingbird wing (cN)	2,7	3,6	4,1	4,6	5,1
thrust generated by artificial wing (cN)	3,4 - 4,2	4,8 - 6,3	4,4 - 7,2	4,3 - 7	6,3

Table 7 Comparison of the thrust generated by hummingbirds with artificial hummingbird-like flapping wings.

The stroke amplitude, flapping frequency and wing length are set at identical values. However the values for the angle of attack and the aspect ratio of hummingbird wings are unknown.

The thrust generated by the artificial wings ranges between in an interval which depends on the angle of attack that is prescribed. The thrust generated by the artificial wings is considerably larger than the thrust generated by the hummingbird wings. This difference however does not mean that a hummingbird is not able to generate more thrust. It is possible that hummingbirds apply an angle of attack that is lower than the lowest angle of attack in our experiments.

To validate the hypothesis that a robotic hummingbird could generate more thrust than its biological counterpart, because the leading edge vortex is stabilised both during forward and backward stroke as the PIV measurements described above, experiments should be performed that mimic the wing motion of a hummingbird under maximal load (see Table 2).

Comparison of the measured thrust with the state of art

Table 8 compares the thrust which is generated by two different prototypes of the *Nano Hummingbird* **[Keennon et al, 2012]** to the thrust generated by the artificial wings used in the experiments described above. The thrust generated by the *Nano Hummingbirds'* wings is larger. This difference is mainly caused by a difference in angle of attack.

	Nano Hummingbird (Saturn)	This research	Nano Hummingbird (final)	This research
wing length (mm)	68	70	74	75
aspect ratio	2,61	3,19	2,85	3,19
flapping frequency (Hz)	28	28	30	30
stroke amplitude (°)	180	180	180	180
thrust (cN)	8,6	7,4	9,3	9,1

Table 8 **This research vs State of art**

3.4.4 CONCLUSION

A total of 740 experiments are performed resulting in the largest data set available. They cover a broad range of wing sizes and wing motion parameters. Five parameters have been varied: flapping frequency, stroke amplitude, angle of attack, aspect ratio and wing span. The prescribed wing motion is the simplified wing motion which is proposed in 2.4.2 and which is used by all the flapping wing micro air vehicles listed in Table 1.

The results show that

- the average thrust varies linearly with the stroke amplitude in the range of interest; this observation confirms the predictions by a quasi-steady model of the aerodynamic forces around a flapping wing.
- the average thrust varies linearly with the wing length in the range of interest; this observation confirms the predictions by a quasi-steady model of the aerodynamic forces around a flapping wing.
- The influence of the flapping frequency on the average thrust; this observation does not confirm the predictions by a quasi-steady model of the aerodynamic forces. A possible explanation is that at higher flapping frequencies, the wing deformation has a significant influence on the thrust that is generated.
- The optimum angle of attack depends on the stiffness of the wing and the aspect ratio.

The measurement can be improved by implementing active wing rotation in order to study the effects of the rotation speed and timing on the average thrust generated by a hummingbird-like flapping wing. Active wing rotation would also allow for a fully automated experimental set-up whereas the one used here could not be fully automated because the block element had to be changed in order to vary the angle of attack.
Further research is required to understand the influence of the wing stiffness better.

3.5 CONCLUSION

A literature study reveals 4 aerodynamic phenomena that enhance thrust around flapping wings: the stabilisation of the leading edge vortex, the Kramer effect, wake capture and the added mass effect. Without these phenomena insects would not be able to fly. The stabilisation phenomenon in the leading edge vortex has the largest positive effect on the thrust. This phenomenon not only occurs around very small flapping wings of insect size but also around hummingbird sized wings.

Two sets of PIV measurements are performed around hummingbird-like flapping wings which confirm the existence of a stabilised leading edge vortex. These experiments also

show a (small) alternating horizontal component of the flow generated by a hummingbird-like flapping wing which suggests that a figure of eight wing tip trajectory has the potential to improve the average thrust that is generated.
A parameter study comprised of a total of 740 experiments is done. These experiments cover a broad range of wing sizes and wing motion parameters. This parameter study shows that the average thrust generated by artificial hummingbird-like flapping wings is larger than the average thrust generated by hummingbirds even if the stroke amplitude, flapping frequency and wing size are set at identical values. The explanation or this observation is the fact that hummingbirds only stabilise the leading edge vortex during forward stroke whereas the leading edge vortex is stabilised during both forward and backward stroke in the case of artificial hummingbird-like flapping wings which performs the simplified wing motion as shown by PIV measurements.

Further research

The experimental parameter study is a useful dataset for the design of the robot hummingbird. It may be used as a validation set for the development of a numerical model which after tuning may again be used for further improvement of the design of kinematic parameters and of the control strategy.

The experimental parameter study itself can be improved by implementing active wing rotation to study the effects of the rotation speed and timing on the average thrust generated by a hummingbird-like flapping wing. Active wing rotation would also allow for a fully automated experimental set-up whereas the one used here cannot yet be fully automated because the block element needs to be changed to set a variable angle of attack. Furthermore by implementing a learning algorithm an experimental set-up that actively controls the angle of attack could search the optimal wing motion for a certain wing. A final suggestion for improvement is the addition of a twist angle parameter to the parameter study that describes wing twist as an element of wing flexibility.

4 THE RESONANT FLAPPING MECHANISM

4.1 INTRODUCTION

The terminology ‘resonant flapping mechanism’ is adopted from literature (**[Baek et al, 2009], [Bolsman et al, 2009], [Hines et al, 2014])**where the adjective ‘resonant’ is used to denominate flapping mechanisms (as the one described in this chapter) that use elastic elements to slow down and store the kinetic energy at the end of each wing stroke. The stored energy then used to assists the acceleration of the wing at the start of the next wing stroke.
Such flapping mechanisms can be considered as mass-spring-damper systems of which the stroke amplitude is maximized for a certain driving torque at the damped resonance frequency. As a consequence the power consumption of the flapping mechanism can be decreased by tuning the flapping mechanism such that the desired flapping frequency is exactly or at least close to the damped resonance frequency.
The principle of a tuned resonant flapping mechanism is also found in nature. Many insects, like the locust for example, use the elasticity of their thorax to temporarily store the energy needed to slow down its wings at the end of each wing beat **[Wood et al, 2003]**.

This chapter describes the resonant flapping mechanism that is developed in the framework of this research (section 4.2 and 4.3) and studies its power consumption and performance (sections 4.4 and 4.5).

4.2 STRUCTURAL COMPOSITION OF THE RESONANT FLAPPING MECHANISM

Overview

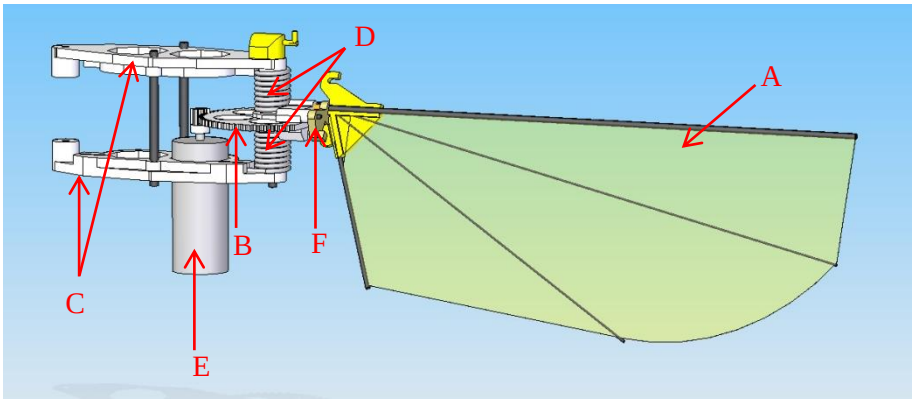

Fig. 45 **The resonant flapping mechanism:** (A) The wing; (B) the shoulder gear (B); (C) the frame (D) helical torsion springs (stroke springs); (E) brushed coreless DC motor with the pinion gear; (F) rotation block element

Fig. 45 shows the resonant flapping mechanism. The wing (A), which has a length of 80mm, is attached to the shoulder gear (B) by means of a rotational joint. The shoulder gear is elastically connected to the frame (C) by two helical torsion springs (stroke springs) (D) and it is driven by a common brushed coreless DC motor (E) with the pinion gear. The motor is fixed to the frame through a clamped connection. The wing rotation is limited by a rotation block element (F) and the wing rotation is suspended elastically to the frame by means of a rubber, called the rotation rubber, between the two yellow hooks (and shown in Fig. 46). Similar flapping mechanisms are described in recent literature **[Zhang et al, 2013]**, **[Campolo et al, 2014]**.
Fig. 46 shows the realisation of this flapping mechanism in a robotic hummingbird. Each wing is driven by a separate resonant flapping wing mechanism.

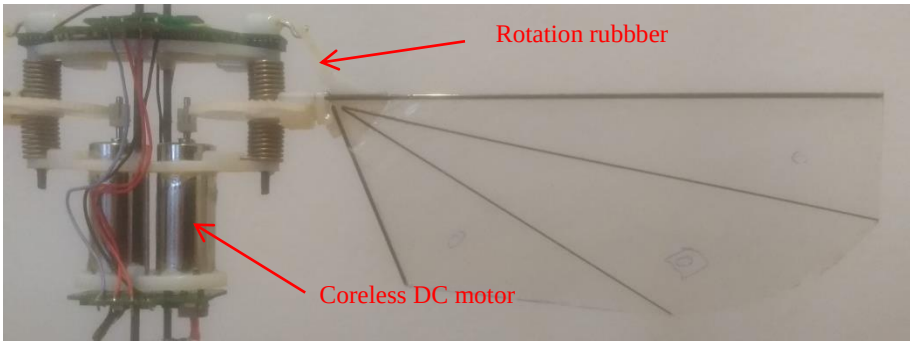

Fig. 46 **The resonant flapping mechanism:** The Kulibrie uses one resonant flapping mechanism for each wing.

Operation

The resonant flapping mechanism is directly driven by a small coreless DC motor. Through the application of an alternating voltage to the coreless DC motor it turns alternately clockwise and counter clockwise. As a result the wing performs a harmonic stroke motion. By driving the stroke motion directly, the flapping mechanism is considerably less complex than flapping mechanisms that uses crank-shaft mechanisms or mechanisms that use cables to convert the continuous rotational motion delivered by most actuators to a back and forth motion of the wing.

As mentioned in the introduction, springs are added to store the kinetic energy in the wings' stroke motion into elastic elements when the wing is slowed down at the end of each wing stroke. Release of the stored energy then accelerates the wing in the initial phase of each wing stroke.

The wing rotation (around its length axis) is elastically suspended by small rubber bands (shown in Fig. 46). It's not actively controlled, the rotational motion takes place as a passive effect under the influence of the inertial, elastic and aerodynamic loads on the wing.

A detailed description of the components of which the resonant flapping mechanism consists: the motor, gearbox, springs and wings and how they were selected is given in chapter 6.

4.3 MATHEMATICAL MODEL AND BEHAVIOUR OF THE RESONANT FLAPPING MECHANISM

A mathematical model for the resonant flapping mechanism could be used to optimize the components of which the resonant flapping mechanism consists and to optimize the resonant flapping mechanism as a whole. The formulation of such a mathematical model is the subject of currently ongoing research. This section describes merely some basic deductions from mathematical models which are overly simplified but have been helpful in the understanding of the flapping mechanism and which can roughly predict some aspects of the resonant flapping mechanism like for example the optimal flapping frequency.

4.3.1 NONLINEAR HARMONICALLY DRIVEN MASS - SPRING - DAMPER SYSTEM

The resonant flapping mechanism can be considered as a harmonically driven mass-spring-damper system with one degree of freedom, the stroke angle ($\theta(t)$).

$$\theta(t) = A\cos(2\pi f t + \varphi) \qquad 4.1$$

A linear harmonically driven mass -spring-damper system can be modelled as a lumped parameter model as follows:

$$I\,\ddot{\theta}(t) + c\,\dot{\theta}(t) + k\,\theta(t) = |\tau|\cos(2\pi f) \qquad 4.2$$

With I the total moment of inertia of the system around the wing root, c the linearised total damping coefficient, k the spring constant and τ the amplitude of the driving torque delivered by the motor.

For a given driving torque, the largest stroke amplitude for such a system is obtained at the damped natural frequency (f_{nd}) defined as:

$$f_{nd} = f_n \cdot \sqrt{1 - \zeta^2} \qquad 4.3$$

with f_n the natural frequency of the system given by equation 4.4 and ζ the dampıng ratio which is dependent of the damping c.

However this formulation is only valid for linear system whereas the resonant flapping mechanism behaves non-linear due the non-linear and nature of the damping (see section 4.3.2). Furthermore no expression for c could be experimentally derived so far. As a consequence formulation 4.3 cannot be used to predict the optimal flapping frequency.

However, for an underdamped system the damped natural frequency is slightly smaller than the natural frequency (f_n) of the system given by:

$$f_n = 2\pi \sqrt{\frac{k}{I_{eq}}} \qquad 4.4$$

With k the spring constant and I_{eq} the total equivalent inertia around the stroke axis as will be described in section 4.2.5. The natural frequency (f_n) is only dependent on the total equivalent inertia and the spring constant which are both easily obtained. From practical experience we know that the optimal flapping frequency is indeed slightly (about 1Hz) smaller than the natural frequency of the resonant flapping mechanism.

4.3.2 THE DAMPING

The total damping of the resonant flapping mechanism is a combination of several different types of damping which are all non-linear:

- the motor damping specific for the type of electric motor that is used,
- the frictional damping, mainly between the gears and in the joints,
- the material damping of the springs,
- the aerodynamic damping caused by the drag on the flapping wing

No quantitative analysis of the damping has been performed.

4.3.3 THE EQUIVALENT INERTIA

Table 9 gives the total equivalent moment of inertia around the stroke axis of the entire flapping mechanism and the equivalent moments of inertia around the stroke axis of all the moving parts of the system. Table 19 and Table 21 in chapter 6 give the equivalent inertia of several motors and wings of different sizes. The exact values of the equivalent moment of inertia of the moving parts of the spring are hard to calculate but their contribution is insignificant. 61% of the total moment of inertia is attributed to the motor and 37% to the wing; together they contribute 98% to the total moment of inertia.

The equivalent moment of inertia of the motor is derived by multiplying the moment of inertia of the motor around its rotating axis with the square of the gear ratio. As a consequence the gear ratio has a large effect on the total moment of inertia.

The total moment of inertia is calculated as follows:

$$I_{eq} = I_{wing} + I_{shoulder} + n^2 I_{motor} \qquad 4.5$$

	I (gmm^2)	Equivalent I (gmm^2)	Percentage of total I (%)	Mass (g)	Percentage of total mass (%)
Motor	3,67	367	61%	2,55	84%
wing	220	220	37%	0,14	5%
shoulder	9,9	9,9	2%	0,32	11%
pinion	0,006	0,6	0%	0,01	0%
springs	0	0	0%	0,34	11%
total		**598**	**100%**	**3,02**	**100%**

Table 9 **Inertia of the resonant flapping mechanism:** The subdivision by its parts of the total equivalent inertia around the stroke axis of the resonant flapping mechanism.

4.3.4 THE SPRING CONSTANT

The current version of the Kulibrie uses two wire wound spiral springs of spring steel. (see section 6.3 in chapter 6). This spring setup behaves linear and the spring stiffness can easily be calculated from the material characteristics, the diameter of the springs, the diameter of the spring wire and the amount of windings (ref).

The spring dimensions are chosen such that the resonance frequency of the flapping mechanism (given the inertia of the total system) is about 24Hz. At this flapping frequency the thrust generated by wings of length 80mm is sufficiently large to lift the weight of the robotic hummingbird.

4.4 POWER CONSUMPTION AND OPTIMISATION OF THE RESONANT FLAPPING MECHANISM

4.4.1 INTRODUCTION

In chapter three the thrust generated by a flapping wing is experimentally determined for a broad range of wing sizes and motions. To have an estimate of the mass of the system, the **power and maximum torque** are dominant factors as they define the size of the motor and the size of the battery, which together constitute about 63% of the total mass of the Kulibrie.

Another important characteristic of a flapping mechanism is its performance, defined as the thrust to power ratio. The performance is a measure for the efficiency of a flapping mechanism and it determines the flight endurance of a robotic hummingbird.

This section describes the measurements of the power consumption and the performance of the resonant flapping mechanism that is used in the experiments described in chapter 3. As such the power consumption of the resonant flapping mechanism is obtained for a large range of wing sizes and wing motions. The power is measured for a total of 722 experiments.

The power and performance of the resonant flapping mechanism are measured experimentally. These measurements provide the first step in the development of a numerical model that is required to optimize the flapping mechanism for a robotic hummingbird of a given wing span.

Another goal of these experiments is to select the most effective wing size and wing motion for the flapping mechanism. The motor, gear ratio and springs of this mechanism are selected based on earlier experiments. Earlier experiments have shown that this

combination of motor, gear ratio and springs is able to generate a wing motion that generates sufficient thrust to lift the weight of the robotic hummingbird in which it is used. The mass of this robotic hummingbird is 14g (see chapter 6). Chapter 2 explains that the stroke amplitude in normal hovering mode should not exceed 160°. The optimum combination of wing size and wing motion is capable of generating at least 7cN of thrust for a stroke amplitude of maximum 160° (equivalent to 7 grams).

4.4.2 MATERIALS AND METHODS

The flapping mechanism, wings and wing motion

The flapping mechanism which is used in the experiments is shown in Fig. 47. It allows to easily change the motor, springs, wing and gear ratio. The motor is a brushed, coreless dc motor with a diameter of 7mm and length of 16mm. Its mass and moment of inertia are shown in Table 19. The gears have a modulus of 0.3mm. The pinion has 6 teeth and the shoulder gear has 60 teeth, this result in a gear ratio of 10. Two stroke springs with a winding diameter of 4mm are used in a parallel configuration. Their characteristics are listed in Table 11. In this set-up the wing is not suspended to the body, but to the stroke gear.

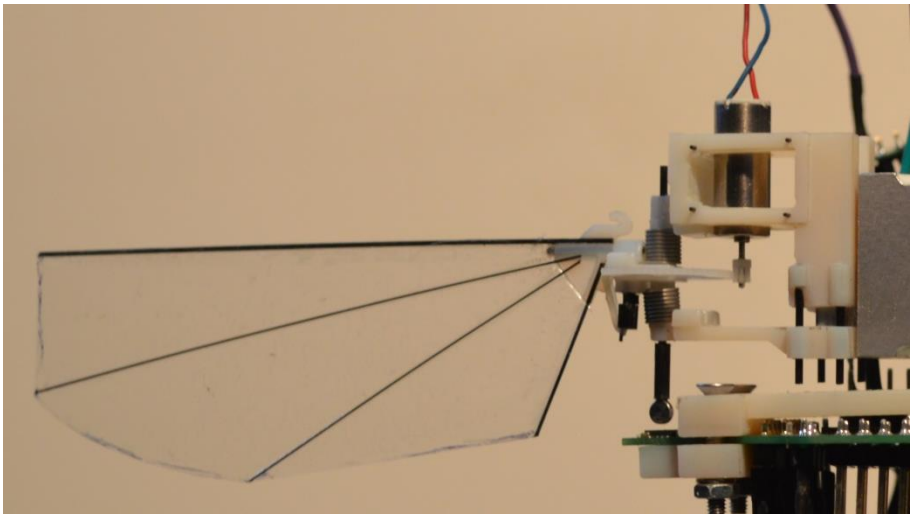

Fig. 47 **The resonant flapping mechanism as used for the experiments:** This flapping mechanism is used for the experiments described in section 4.3.

Measurement Set-up

The measurement set-up used for these experiments introduces explained in section 3.4 of chapter 3. For the convenience of the reader, the schematic representation is shown

again in Fig. 48. Four quantities are measured: the average thrust generated by the wing (T in dimensions cN), the stroke angle (θ in degrees), the armature current (A) defined as the current through the actuator [M] and the armature voltage (U) defined as the voltage over the motor. The measurements of the average thrust and the stroke angle are discussed in section 3.4.2.

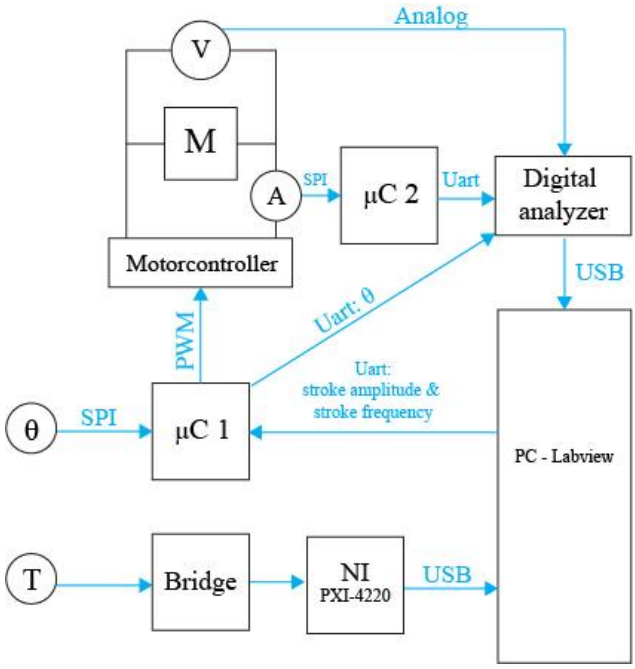

Fig. 48 **A schematic diagram of the measurement set-up:** Four quantities are measured: the average thrust generated by the wing (T in dimensions cN), the stroke angle (θ in degrees), the armature current (A) defined as the current through the actuator [M] and the armature voltage (U) defined as the voltage over the motor.

Armature Current

The armature current (A) is measured using the TLI4970-D025T4 miniature magnetic current sensor for AC or DC measurements, represented by (A) in Fig. 48. The measurement sensitivity is 6.1mA resulting from a 13bit discretisation of the 50V (-25A to 25A) measuring range. The current is sampled at 10 kHz, resulting in 400 samples per wingbeat at a flapping frequency of 25Hz. A custom PCB connects the current sensor with microcontroller2 that serves as an interface between the current sensor and the logic analyser. Fig. 49 shows an example of the current measurement.

Armature voltage

The voltage over the actuator is recorded using an analogue input of a logic analyser. The measurement sensitivity is 4.9mV resulting from a 12bit discretisation of the 20V (-10V to 10V) measuring range. The voltage is sampled at 125kHz, resulting in 5000 samples per wingbeat at a flapping frequency of 25Hz.

Power

The average electric power (P_{av}) consumed by the motor can be derived from the current and voltage measurements. The power is calculated as follows:

$$P_{av} = |U| \cdot |i| \cdot \cos(\varphi) \tag{4.6}$$

The phase difference (φ) between the current and the voltage is derived by analysing the current and voltage signals in *Matlab* **[MathWorks, 2017].**

Fig. 49 shows an example of the measurements of the armature current (red) and voltage (blue) for a stroke amplitude of 150° and a flapping frequency of 25Hz. The phase difference is shown as the distance between the yellow lines (which depict the zero-passage) and it is near zero for this case (and most other cases). A phase difference near zero is expected at the resonance frequency of the flapping mechanism.

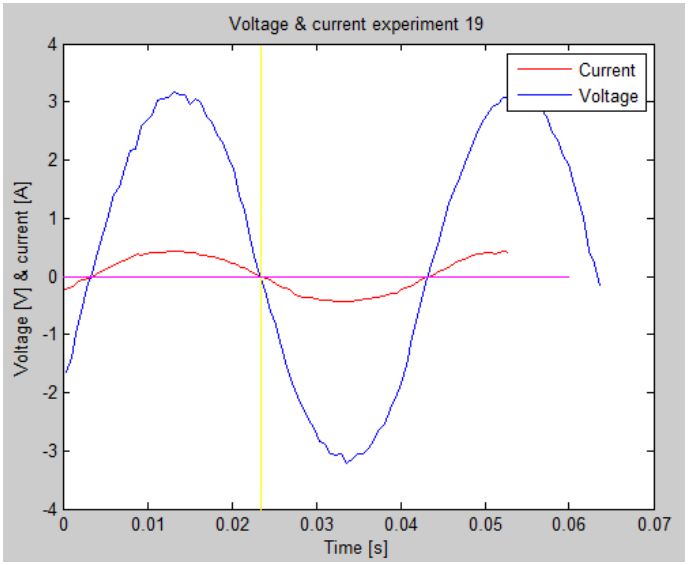

Fig. 49 Measurement of the power: current (red) through the actuator and the voltage over the actuator (blue) for a stroke amplitude of 150° and a flapping frequency of 25Hz. The phase difference is shown as the distance between the yellow lines is near zero.

4.4.3 RESULTS AND DISCUSSION

POWER CONSUMPTION

Fig. 41 to Fig. 44 in chapter 3 show the power consumption of the resonant flapping mechanism as functions of the stroke frequency, stroke amplitude, angle of attack, wing size and aspect ratio.

Power as a function of the flapping frequency

Fig. 41A shows that the required power increases uniformly with the flapping frequency for small stroke amplitudes. For large stroke amplitudes, a valley like character is observed for the power as a function of the flapping frequency. This valley reaches a minimum at a flapping frequency of about 24.5 Hz, which is higher than the resonance frequency.

The power in function of the stroke amplitude, angle of attack and wing size

Fig. 42 Fig. 43 and Fig. 44show that the power increases with the stroke amplitude, the angle of attack and the wing size as expected.

PERFORMANCE

Fig. 50 shows a scatter plot of the thrust in function of the power consumed by the resonant flapping mechanism for all experiments.

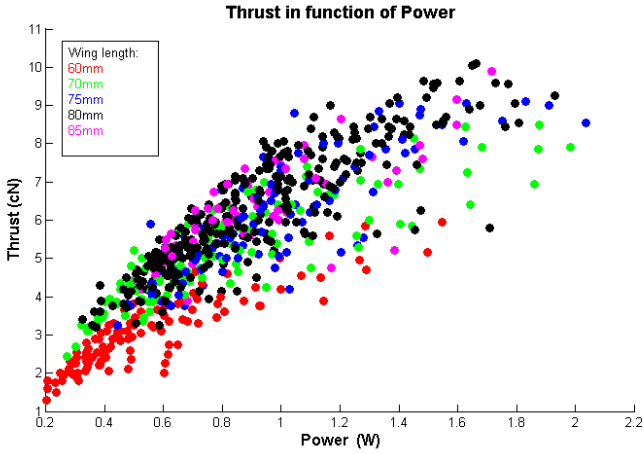

Fig. 50 **Thrust in function of Power: A** scatter plot of the thrust in function of the power consumed by the resonant flapping mechanism for all experiments

As expected Fig. 50 shows that a smaller wing generates less thrust and consumes less power. Each wing covers a large range in thrust and power depending on the wing motion that is imposed.

Fig. 51 shows the performance of the resonant flapping mechanism as a function of the flapping frequency for 5 different wing sizes. The stroke amplitude in these experiments is 160° and the angle of attack is 50°. The highest performance is observed at the resonance frequency which increases if the wing size (and thus wing inertia) decreases.

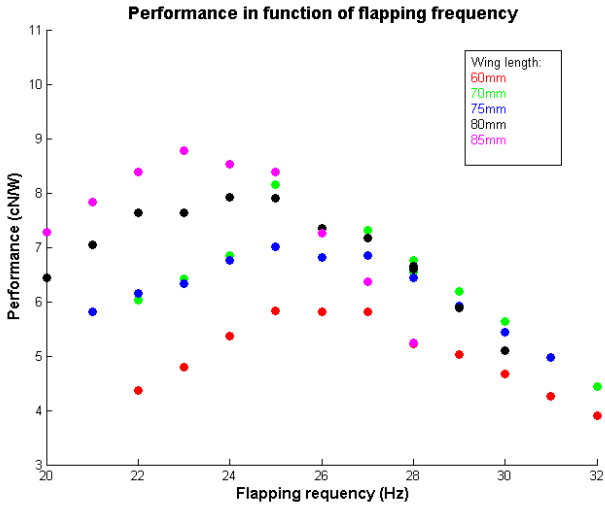

Fig. 51 **Performance in function of flapping frequency:** The performance of the resonant flapping mechanism in function of the flapping frequency for 5 different wing sizes. The stroke amplitude in these experiments is 160° and the angle of attack is 50°. The highest performance is observed at the resonance frequency which increases if the wing size (and thus wing inertia) decreases.

Fig. 52 shows the performance of the resonant flapping mechanism as a function of the stroke amplitude for 5 different wing sizes. The flapping frequency in these experiments is 25Hz and the angle of attack is 50°. The measurements at 170° stroke amplitude are not consistent with the other experiments. The performance remains approximately constant with variable stroke amplitude.

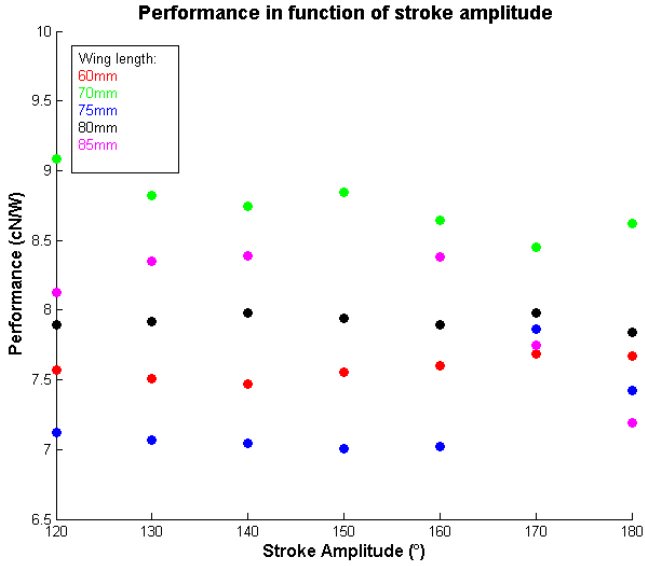

Fig. 52 **Performance in function of stroke amplitude:** The performance of the resonant flapping mechanism in function of the stroke amplitude for 5 different wing sizes. The flapping frequency in these experiments is 25Hz and the angle of attack is 50°. The measurements at 170° stroke amplitude are not consistent with the other experiments. The performance remains approximately constant with variable stroke amplitude.

SELECTION OF THE OPTIMUM WING AND WING MOTION FOR A ROBOTIC HUMMINGBIRD

To select the most appropriate wing and wing motion for a robotic hummingbird, only the experiments are taken into account that generate sufficient thrust (at least 7cN) to lift the estimated weight of a robotic hummingbird given that it uses a resonant flapping mechanism with the dimensions proposed above and with a stroke amplitude of 160° or less. Fig. 53 shows a scatter plot of the thrust as a function of the performance for all these experiments.

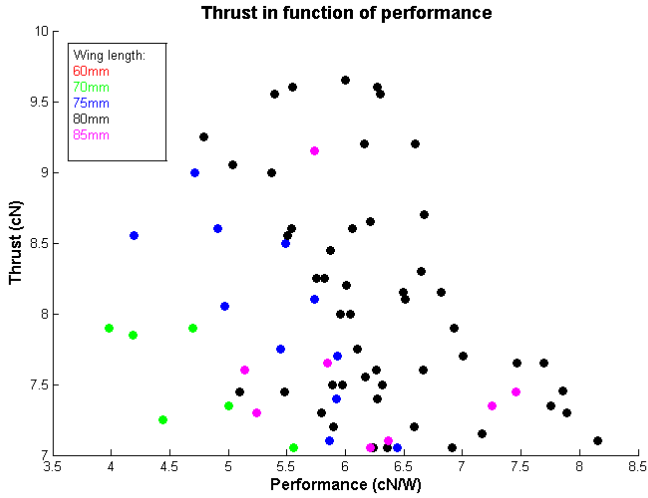

Fig. 53 **Thrust in function of performance:** The performance drops with the size of the wing and for each wing, the performance drops if the thrust it generates increases.

Table 10 shows some important conclusions that can be drawn from the analysis of wing motions of the data points in Fig. 53.

Wing length (mm)	# experiments	f_{min}	f_{max}	A_{min}	aoa_{min}
60	0	/	32	/	/
70	7	28	32	160	50
75	12	25	31	160	50
80	50	22	30	140	50
85	9	24	28	130	50

Table 10 **Analysis:** only the experiments are taken into account that generate sufficient thrust (at least 7cN) to lift the estimated weight of a robotic hummingbird with a stroke amplitude of 160° or less. No experiment with a 60mm wing generated more 7cN or more thrust.

- **A wing of 60mm length is not capable of generating a sufficient thrust level.** To generate a larger thrust the flapping frequency has be increased to above 32Hz, but for the given system (which is tuned at 22.5 Hz) the difference between the flapping and the resonance frequency is too large to be efficient.
- The **angle of attack (aoa) has to be at least 50°** regardless of the wing size.
- T**he minimum required flapping frequency increases with decreasing wing size** from 22Hz for an 80mm wing to 28Hz for a 70mm wing. A possible explanation is that the flapping frequency has to be sufficiently large to compensate the decrease of thrust due to the wing twist, which increases with wing size
- The minimum required stroke amplitude increases with decreasing wing size from 130° for an 80mm wing to 160° for a 75mm wing.

Table 11 shows the five most efficient wing and motion combinations that generate at least 7cN thrust with a stroke amplitude of 160° or less. The most efficient option (first row) is implemented in the Kulibrie.

L [mm]	AR	f [Hz]	A (°)	aoa (°)	T [cN]	|V| [V]	|i| [A]	P_{av} (W)	T / P (cN/W)
80	4	25	160	50	7,10	3,34	0,52	0,87	8,38
85	3.19	25	160	50	7,35	3,39	0,52	0,88	8,15
80	3.19	25	160	50	7,30	3,31	0,56	0,92	7,89
80	3.19	25	160	50	7,35	3,38	0,56	0,95	7,76
80	4	26	160	50	7,46	3,48	0,55	0,95	7,86

Table 11 **The five most efficient wing and motion combinations** that generate at least 7cN thrust with a stroke amplitude of 160° or less.

Wing length

Four of the five best performances are obtained using an 80mm wing. The performance drops with the size of the wing (as can be seen in Fig. 53). This observation is explained by the fact that smaller wings require a higher flapping frequency to generate sufficient thrust. The higher the flapping frequency the larger the difference with the resonance frequency (22.5 Hz). To increase the performance of smaller wings, the resonance frequency should be increased by using a smaller motor or stiffer springs.

Aspect ratio

The wings used to study the effect of the aspect ratio all have the same wing length of 80mm. From the three different aspect ratios that are tested, the largest wing has the best

performance (Fig. 53 and Table 11). More experiments are needed to study the effect of the aspect ratio on the performance of a flapping wing and to determine the optimum aspect ratio of a flapping wing.

Flapping frequency

The flapping frequency of the best performing experiments is 25Hz. This value is slightly higher than the resonance frequency of 22.5 Hz. This observation suggests that the performance of the resonant flapping mechanism can be increased by selecting slightly stiffer springs.

Angle of attack

The optimal angle of attack depends on several parameters like the wing size, the stiffness of the wing and the aspect ratio. The angle of attack that performs best in these experiments is 50° imposed on an 80mm wing. .

Thrust

The thrust generated by the five most performing experiments shown in *Table* 1114 is just a little higher than 7cN. Fig. 53 shows that for each wing, the performance drops if the thrust it generates increases.

Power consumption

The power consumption of the 5 most performing experiments is between 0.87W and 0.95W.

Performance

The performance of the 5 most performing experiments is between 7.86 cN/W and 8.15cN/W.

4.4.4 COMPARISON WITH STATE OF ART

Comparison with the *Nano Hummingbird*

In Table 12 the performance of the Kulibrie is compared to the performance of the *Saturn* prototype of the *Nano hummingbird* which is the most performing prototype of the *Nano Hummingbird* **[Keennon et al, 2012]**.

	Nano Hummingbird (Saturn)	Kulibrie
mass (g)	17,5	14,0
wing length (mm)	68	80
wing span (mm)	15,8	18,6
Power (W)	3,03	1,74
performance cN/W	5,8	8,4

Table 12 **Comparing performance:** The resonant flapping mechanism that is used in the Kulibrie has a performance of 8.4cN/W, which is 40% higher than the performance of the Nano hummingbird (5.8cN/W).

The power tabulated is the power that goes to the wing motion and does not include the power consumed by the electronic system.

The resonant flapping mechanism that is used in the Kulibrie has a performance of 8.4cN/W, which is 40% higher than the performance of the Nano hummingbird (5.8cN/W).

Comparison with propellers

Table 13 shows the performance of several motor-propeller combinations. The first four combinations use the smallest motors and their recommended propellers of *T-motor* **[T-motor, 2017]** a highly regarded manufacturer of electric motors and propellers for drones. From several operating conditions we only listed the ones with the highest performance. The fourth column shows the performance of smaller propellers **[Goetze, 2017].**

	T-motor MT3520	T-motor MT2208	T-motor MT1306	small props (refB)	resonant flapping mechanism
m (g)	205	45	11,2	2,9	2,55
thrust (g)	720	270	128	27 – 34	7
Disc area (cm^2)	1590	394	177	28	90
performance (cN/W)	12,5	9,7	6,4	3,0 - 3,5	8,0

Table 13 **Comparing performance with propellers:** The performance of a propeller decreases sharply with its radius. The performance of a flapping wing is considerably higher than the performance of a propeller with a comparable disc area.

The mass in Table 13 includes only the mass of the motor that drives the propeller or the flapping wing. The thrust that can be generated by a propeller is much higher than the thrust generated by a flapping wing with a comparable disc area (the area covered by the flapping wing in the stroke plane).

The performance of a propeller decreases sharply with its radius. By interpolation of the data in Table 13, it is clear that the performance of a flapping wing is considerably higher than the performance of a propeller with a comparable disc area.

4.5 THE ADDED VALUE OF RESONANCE

In the evaluation of the influence of the principle of resonance on the power consumption and peak driving torque, the average power consumption and peak driving torque ($|\tau|$) obtained by the experiment described above is compared to the average power and the peak torque that would be necessary to drive the wing without a spring element (k=0). This approach is elaborated here for the combination of wing, flapping mechanism and wing motion used in the latest prototype of the Kulibrie.

The relevant parameter for this combination of wing, flapping mechanism and wing motion are listed in Table 14.

wing	
L(mm)	80
AR	3.19
wing motion	
A (°)	160
aoa (°)	50
f (Hz)	25
Motor	
Ki (mNlm/A)	0.85
resonant flapping mechanism	
I (gmm2)	598
k (Nmm/rad)	0,0119
|i|	0.52
P_{av} (W)	0.87

Table 14 **Parameters**: the combination of wing, flapping mechanism and wing motion used in the latest prototype of the Kulibrie.

4.5.1 POWER CONSUMPTION AND PEAK TORQUE WITH RESONANCE

The power consumption of the resonant flapping mechanism

The average power consumption P_{av} of the considered combination of wing, flapping mechanism and wing motion is 0.87W, measured as described in section 4.3.2. The terms on the left hand side of equation 4.2 can be considered as torque terms: One contribution to overcome the inertial load, one contribution of the elastic load and a final contribution to overcome the aerodynamic load. From theses torques and the known stroke motion of the wing, the power according to each torque term can be derived separately.

Fig. 54 shows the evolution of each of the three contributions with time over two consecutive flapping cycles. This figure is obtained using the coarse estimate for the damping coefficient derived in section 4.4.2.

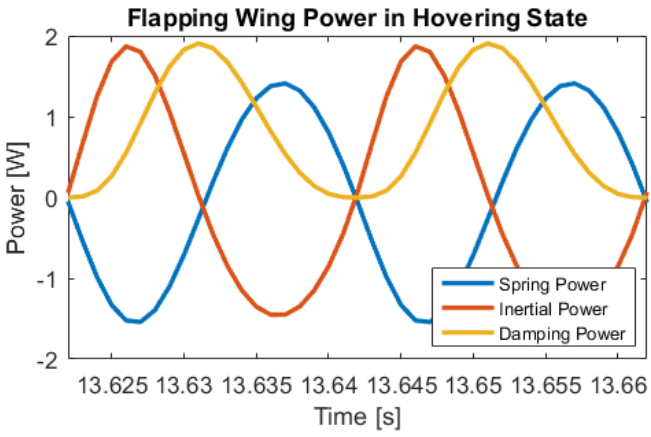

Fig. 54 **Flapping wing power in hovering state:** The evolution of each of the three contributions with time over two consecutive flapping cycles. This figure is obtained using the coarse estimate for the damping coefficient derived in section 4.4.2.

The figure shows that the power required to drive the inertial load is almost fully compensated by the springs, as is expected at the resonance frequency. In theory the power required to drive the inertial load should be fully compensated by the springs if the flapping frequency matches the resonance frequency of the flapping mechanism.

The peak driving torque of the resonant flapping mechanism

The peak driving torque necessary to drive the considered wing motion with the resonant flapping mechanism can be derived using the torque constant of the motor and the peak current $|i|$, which is 0.52A, measured as described in section 4.3.2.

$$|\tau| = K_i|i| \tag{4.7}$$

Fig. 55 shows the evolution of the driving torque with time for one flapping cycle, taking into account the damping coefficient as derived in section 4.4.2.

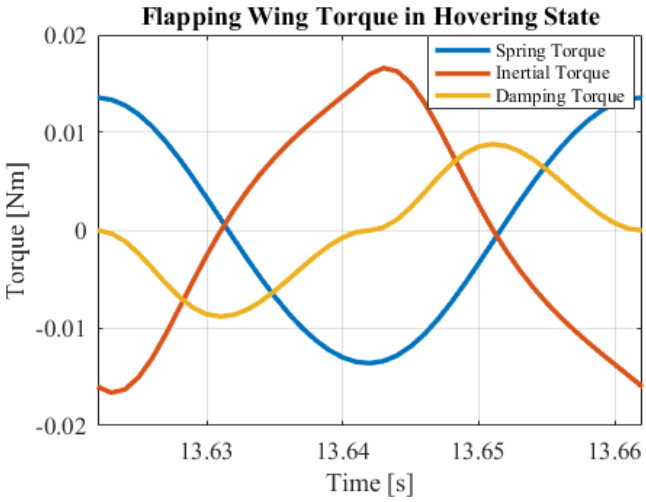

Fig. 55 **Flapping wing torque in hovering state:** The evolution of the driving torque with time for one flapping cycle, taking into account the damping coefficient as derived in section 4.4.2.

4.5.2 POWER CONSUMPTION AND PEAK TORQUE WITHOUT RESONANCE

The power consumption of the flapping mechanism without resonance

The average power consumption of the flapping mechanism without resonance can be estimated using equation 4.8:

$$P_{av} = |U| \cdot |i| \cdot \cos(\varphi) \tag{4.8}$$

U can be calculated by the following equation that applies to coreless dc-motors:

$$U = K_v\,\omega + Ri \tag{4.9}$$

Kv and R represent motor constants which are listed in Table 10. In the assumption of a perfectly harmonic wing motion, the angular velocity (ω) is derived from the measured wing motion as follows:

$$\omega = A\,2\pi f\cos(2\pi f t) \tag{4.10}$$

i can be estimated by solving the lumped parameter model for of the flapping mechanism (eq. 4.2) with the prescribed wing motion, in the case of a spring constant equal to zero:

$$I\,\ddot{\theta} + c\,\dot{\theta} = K_i i \tag{4.11}$$

With

$$i = |i|\cos(2\pi f t) \tag{4.12}$$

The solution of equation 4.11 is given by:

$$\theta(t) = A\cos(2\pi f t + \vartheta) \tag{4.13}$$

In equations 4.11 and 4.13, I, K_i, f and A are all constants which are measured and listed in *Table* 1114. To solve equation 4.11 the value of the total damping coefficient c is required.

A coarse estimate for the total damping coefficient of the system is derived from the lumped parameter model of the flapping mechanism (eq 4.2) with the prescribed wing motion:

$$I\,\ddot{\theta} + c\,\dot{\theta} + k\,\theta = K_i|i|\cos(2\pi f t) \tag{4.14}$$

The solution of equation 4.14 is given by:

$$\theta(t) = A\cos(2\pi f t + \vartheta) \tag{4.15}$$

For this case $|i|$ is measured, it is listed in *Table* 11.

Solution of equation 4.14 gives a value of c of $1.9 \cdot 10^{-7}$ (Nms/rad) and a ϑ of 156°. The motor current $|i|$ is then 1.12 A and the average power consumption P_{av} is 1.1 W.

The peak torque of the flapping mechanism without resonance

The peak torque of the flapping mechanism without resonance is 0.015Nm and is calculated using equation 4.7 and the values of $|i|$ derived in the previous paragraph.

4.5.3 COMPARISON OF POWER CONSUMPTION AND PEAK TORQUE

Power consumption

Comparison of the average power consumed by the resonant flapping mechanism (0.85W) with the average power consumed by the flapping mechanism without resonance (1.1W) for the same combination of wing and prescribed wing motion shows that the resonant flapping mechanism consumes 0.25W less, which means an improvement to efficiency of 22%. As a consequence a smaller and lighter motor can be used to drive the flapping wing motion and the flight endurance for the same battery increases.

Fig. 56 shows the evolution of the power consumption with and without resonance as a function of time for two consecutive flapping cycles as derived above.

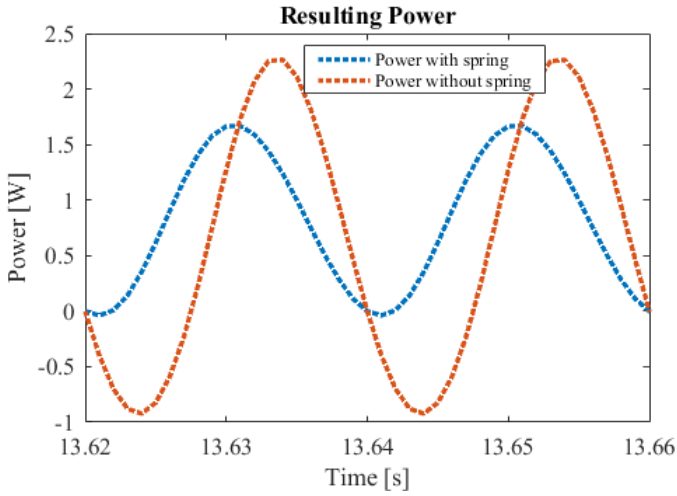

Fig. 56 **Resulting power consumption:** The evolution of the power consumption with and without resonance as a function of time for two consecutive flapping cycles

Peak torque

The peak motor torque required by the resonant flapping mechanism (0.008 Nm) is 47% lower than the peak torque required by the flapping mechanism without resonance (0.015Nm) for the same combination of wing and prescribed wing motion. As a consequence a smaller (lighter) motor can be used to drive the flapping wing motion.

Fig. 57 shows the evolution with time of the driving torque with or without resonance for two consecutive flapping cycles as derived above.

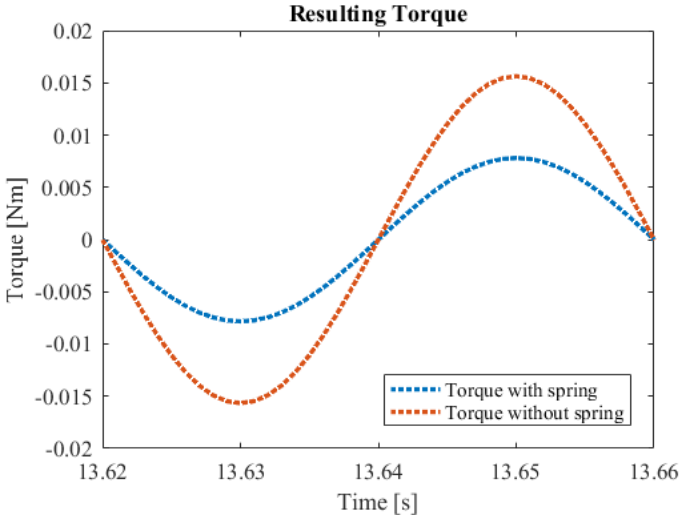

Fig. 57 **Resulting driving torque:** The evolution with time of the driving torque with or without resonance for two consecutive flapping cycles.

4.6 CONCLUSIONS

The resonant flapping mechanism can be considered as harmonically driven mass-spring-damper system. The non-linearity of the damping and the fast alternating motion of the coreless DC motor complicate the formulation of a mathematical model that can adequately predict the wing motion for a known flapping mechanism and wing.

The power consumption and performance is measured for a total of 722 experiments with different combinations of wing size and prescribed wing motions. The power consumption of the elastically suspended flapping mechanism is obtained for a large range of wing sizes and wing motions. The power consumption increases with stroke amplitude, angle of attack and wing size and it is minimum at a flapping frequency close to the resonant frequency of the flapping mechanism.

From these experiments the **best performing wing motion and wing size for a robotic hummingbird** are identified for a particular selection of the motor, gearbox and springs.

At a stroke amplitude of 160°, a flapping frequency of 25Hz, and an angle of attack of 50°, an 80mm wing generates 7.1cN thrust while consuming 0.87W of power. This results in a performance of 8.38cN/W.

Comparison of the performance of the resonant flapping mechanism with the flapping mechanism of the **Nano Hummingbird** shows that the performance of the resonant flapping mechanism is 40% higher than the performance of the Nano Hummingbird (5.8cN/W). Furthermore the resonant flapping mechanism performs considerably better than **propellers** with a comparable disc area, but these propellers can generate much more thrust.

The resonant flapping mechanism, as implemented in the Kulibrie, consumes 22% less power than the same flapping mechanism without resonance (without stroke springs). The peak torque is reduced with 47%. As a consequence a smaller (lighter) motor can be used to drive the flapping wing motion.

5 FLIGHT CONTROL OF A ROBOTIC HUMMINGBIRD

5.1 INTRODUCTION

The flight control of insects and hummingbirds is a marvel of biological evolution. The precision with which a hummingbird can hover above a flower to drink nectar, the air acrobatics performed by a fly to avoid the hand of an irritated monkey or the dance a honey bee performs to inform its fellow nectar hunters about the discovery of new flowers are just a few mesmerizing examples. These examples are the living proof that extraordinary flight manoeuvres can be performed by flapping wings.

This chapter describes how these extraordinary flight manoeuvers result from asymmetric wing motions and how these asymmetric wing motions can be performed by a robotic hummingbird, like the Kulibrie.

Section 5.2 gives an overview of the basics of flight control relevant to the rest of the chapter. Section 5.3 studies different types of asymmetric wing motions and describes which motion modes can be generated by the resonant flapping mechanism of the Kulibrie.

5.2 BASICS OF FLIGHT CONTROL

5.2.1 ATTITUDE: ROLL, PITCH AND YAW

To stabilise the flight of a robotic hummingbird its attitude (orientation in the air) has to be controlled. Three rotational degrees of freedom define the attitude of a robotic hummingbird: roll, pitch and yaw. The orthogonal roll, pitch and yaw axes for a robotic hummingbird are defined here as shown in Fig. 58 they intersect at the centre of mass of the robotic hummingbird. A rotation around the roll axis is defined by the roll angle (β_R). The pitch (β_P) angle and the yaw ($\beta_{Y)}$ angle are defined similarly.

To change the roll angle, a roll torque (τ_R) around the roll axis has to be generated. A similar definition applies to the pitch torque (τ_P) and the yaw (τ_Y) torque.

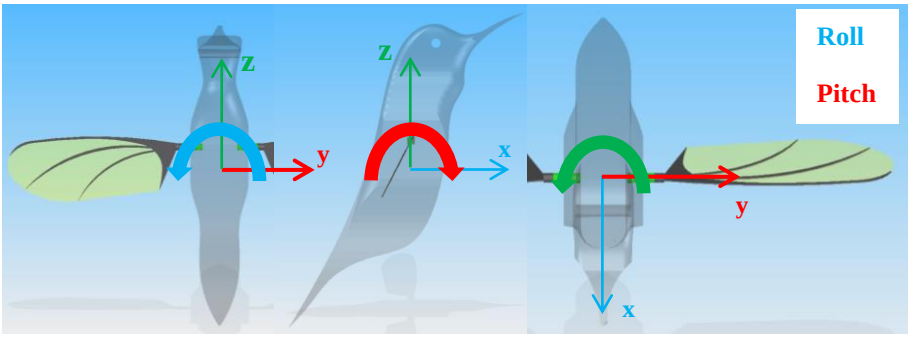

Fig. 58: Roll, Pitch & Yaw: Three rotational degrees of freedom define the attitude of a robotic hummingbird: roll, pitch and yaw

5.2.2 FLIGHT STABILISATION: ATTITUDE CONTROL

Attitude control

The attitude of a flying object can be partially controlled passively, without any active control; this greatly simplifies the control design. In a hot air balloon for example, pitch and roll are passively stabilised by the buoyancy and gravitational forces. Classic airplanes or large birds are passively stabilised during flight in pitch and yaw by the aerodynamic damping of their tail. While propeller based drones like a helicopter are partially passively stabilised by the gyroscopic effect resulting from the rotation of the propeller(s).

If the attitude of a flying object cannot be stabilised passively, an active control strategy is necessary. This requires sensors (or a pilot) to sense its attitude and means to generate roll, pitch and yaw torques to counteract disturbances from the desired attitude. As a consequence the control design becomes more complex.

Attitude control of a robotic hummingbird

Although larger birds use their tail to stabilise flight and perform flight manoeuvres, the tail of hummingbirds is remarkably small and most small insects have no tail at all. Furthermore flapping wings does not generate a resulting gyroscopic effect that increases stability, like propellers do.

As a consequence a robotic hummingbird needs to be able to generate roll, pitch and yaw torques to achieve flight stability and to perform flight manoeuvres. These torques can be generated by performing an asymmetric wing motion: to generate a roll torque the left wing needs to perform a slightly different motion than the right wing, whereas to generate a pitch torque a slight difference between the forward and backward stroke of both wings is required. Yaw torques can be generated by the combination of the two:

both an asymmetry between the flapping motion of the left and right wing as an asymmetry between forward and backward stroke. Section 5.3 studies the asymmetric wing motions that can be generated by flapping wings.

Passive stabilisation of the heading by flapping wings
The heading of a robotic hummingbird is defined by its yaw angle. If the two wings of a robotic hummingbird or its biological counterpart flap symmetrically the yaw motion is passively stabilised similar to how a tail stabilises the heading. This phenomenon is referred to as 'flapping counter-torque' by Hedrick et Al. **[Hedrick et al, 2009]** who are the first authors to describe this phenomenon. This phenomenon explains why during most flights of the Kulibrie its heading does not change rapidly, even though it is not controlled.

5.3 PERFORMING MANOEUVERS, MANOEUVRABILITY AND THE FLIGHT ENVELOPE

To change its position in space a flying object needs to perform flight manoeuvres, like forward or backward flight, flight in lateral directions, roll, pitch, yaw etcetera.

The flight envelope
Free flight is defined by six motion degrees of freedom. The more degrees of freedom that can be controlled independently during flight, the larger the flight envelope of a drone. A larger flight envelope allows a drone to perform more complex flight manoeuvres.

Usually some of the six degrees of freedom are coupled such that they cannot be controlled independently. Common quadcopters for example can only control four independent degrees of freedom. Forward or backward flight is an induced second order effect of a pitch rotation, while flight in lateral directions is an induced second order effect of a roll rotation.

The manoeuvrability
The manoeuvrability or agility is defined here as the degree of responsiveness with which flight manoeuvres can be performed. The manoeuvrability of a drone depends mainly on four aspects:

- the inertia of the drone around it centre of mass
- the magnitude of the control torques and forces
- the presence of a tail and its size and position
- the presence of a gyroscopic effect induced by fast rotating propellers

The larger the inertia and the smaller the control torques and forces, the longer it takes to perform a certain flight manoeuvre. A tail has an adverse effect on the manoeuvrability of a drone, because it acts like an aerodynamic damper to certain manoeuvres. The larger the tail and the further away the tail is positioned from the centre of mass, the larger the aerodynamic damping. Fast rotating propellers generate a torque, like gyroscopes, that counteract certain flight manoeuvres.

A large flight envelope and a high manoeuvrability are advantages for drones (like robotic hummingbirds) that need to swiftly perform complex flight manoeuvres. For example drones that are used for indoor applications or drones that need to dodge fast moving obstacles.

5.3.1 AVERAGE THRUST (REDEFINED)

In chapter 3 the average thrust was defined as the time average of the upward oriented vertical component of the force generated by a flapping wing. In this chapter a different definition is more convenient. The average thrust is redefined here as the time averaged resulting force generated by a flapping wing.

Although the force generated by hummingbird-like flapping wings varies continuously during the whole flapping cycle. The principle is adopted here that the flight of a robotic hummingbird can be stabilised and controlled by only taking into account the size and the position and orientation of the average thrust generated by the right wing (T_R) and the left wing (T_L) relative to the robotic hummingbirds' body.

All the robotic hummingbirds in Table 1 are controlled by control strategies based on this principle. Orlowski **[Orlowski, 2011]** shows that this principle is only valid if the inertia of the wings is low enough compared with the body mass of the robotic hummingbird.

5.4 ASYMMETRIC WING MOTIONS

This section describes the asymmetric wing motions that enable hummingbird-like flight manoeuvres. Several different kinematic parameters can be adjusted to control thrust or roll, pitch and yaw moments around the centre of gravity. Section 5.3.1 gives an overview of the dominant parameters. The next section gives an overview of the set of asymmetric wing motions observed in nature and a literature review of the asymmetric wing motions implemented in some robotic hummingbirds. The final section explains the set of asymmetric wing motion concepts that are implemented in the Kulibrie.

5.4.1 OVERVIEW

Table 15 gives an overview of the most important asymmetric wing motions that can be generated by modifying one of the following parameters of the wing motion:

- the stroke amplitude: A
- the angle of attack: α
- the stroke frequency: f
- the mean stroke angle: ϕ
- the deviation of the wing from the average stroke plane: δ
- the phase between the stroke and the rotation of the wing: ζ

The different types of asymmetric wing motions are marked by a short code starting with a letter that stand for the first order effect (2nd column) of the asymmetric wing motion (T: thrust, R: roll, P: pitch and Y: yaw) followed by the parameter of the wing motion that is adjusted and the type of asymmetry between parentheses. The type can be an asymmetry between the left and right wing (L/R), an asymmetry between the forward and the backward stroke of a wing (F/B) or a combination of the two (F/B & L/R). For example the R(f / L-R) asymmetric wing motion is one that generates a roll torque (R), by an asymmetry of the flapping frequency (f) between the left and the right wing (L/R).

The third column of Table 15 denotes the second order effect of an asymmetric wing motion. For example as soon as an R(A/L-R) roll manoeuvre is initiated it immediately generates a roll torque (first order effect) causing the robotic hummingbird to tilt around a lateral axis. This motion tilts the average thrust vector too and as a result it has a lateral component. As a consequence the robotic hummingbird starts to move in the lateral direction (second order effect).

	1st order effect	2th order effect	effect	applied in	active α ?
T(A/ -)	Thrust	/	++	Kulibrie, Robobee, Maryland	no
T(α/-)	Thrust	/	++	Nano hummingbird	yes
T(f/-)	Thrust	/	++	Kulibrie with stroke-cam mechanism	no
R(A/L-R)	Roll	sideways	++	Kulibrie, Robobee, Maryland	yes
R(α/L-R)	Roll	sideways	++	Nano Hummingbird	no
R(f/L-R)	Roll	sideways	++	Kulibrie 1 (stroke-cam mechanism)	yes
R(δ/L-R)	Roll & Sideways	/	+	/	no
P(ϕ/F-B)	Pitch	forward	++	Kulibrie, Robobee	no
P(α/F-B)	Pitch	forward	++	Nano Hummingbird	yes
P(f'/F-B) (ref)	Pitch & forward	/	+	Kulibrie, Robobee	no
P(δ/F-B)	Pitch & forward	/	+	Maryland	no
Y(ϕ / F-B & L-R)	/	yaw (?)	/	Kulibrie, Robobee	no
Y(α / F-B & L-R)	Yaw	/	++	Nano Hummingbird	yes
Y(f' / F-B & L-R) (ref)	Yaw	/	-	Kulibrie, Robobee	no
Y(δ / F-B & L-R)	Yaw	/	-	Maryland	no
Y(A & ϕ / F-B & L-R) (ref)	Roll & Pitch	Yaw (?)	-	Robobee	no
Y(ϕ => ζ / F-B & L-R)	Yaw	/	-	Kulibrie	no

Table 15 Asymmetric wing motions: Roll (R), Pitch (P) or Yaw (Y) manoeuvres can be performed by an asymmetry of the stroke amplitude (A), flapping frequency (f), mean stroke angle (ϕ), deviation of the wing from the average stroke plane (δ) or the phase between the stroke and the rotation of the wing (ζ). This asymmetry can be between the left and the right wing (L-R) or between the forward and the backward stroke (F-B). For some asymmetric wing motions an active control of the wing rotation (α) is required. which is not implemented in the resonant flapping mechanism. The references to the robotic hummingbirds mentioned in 5th column can be find in Table 1.

The larger the magnitude of thrust or torque generated by an asymmetric wing motion, the faster can a desired manoeuvre be executed or the smaller the modification needs to be to generate sufficient thrust or torque. The minimum required size of the thrust or torque depends on many factors, but in general a large influence on thrust or torque is preferred.

The actual magnitude of the resulting force or torque that can be generated by the asymmetric wing motion depends on many parameters concerning the wing motion, shape and size. To give an idea of this size, the fourth column of Table 15 gives an arbitrary measure of the magnitude of the resulting force or torque that can be generated by the asymmetric wing motion. For example: tests have shown that the split frequency yaw method (Y(ϕ / F-B & L-R) which is discussed in the next section can't generate a yaw torque that is sufficient large in contrary to the Y(α / F-B & L-R) method.

Split frequency modulation: Y(f' / F-B & L-R)
Split frequency modulation as proposed by **[Chirarattananon et al, 2014]** is a method to generate a yaw torque or a pitch torque. This method is characterised by a difference of angular stroke velocity between forward and backward stroke. In other words: the wing moves faster during forward stroke than during backward stroke (or vice versa). This results in a difference in drag between forward and backward stroke.

An increased wing speed in forward stroke is compensated by a reduced speed in backward stroke, such that the total cycle time remains constant.

Wriggle steering: Y(A & ϕ / F-B & L-R)
Wriggle steering as proposed by **[Fuller et al, 2015]** is a method to generate a yaw manoeuvre by performing consecutive cycles of roll and pitch manoeuvres as shown in Fig. 59. These cycles of consecutive roll and pitch manoeuvres result in a small change in yaw angle after each cycle because of nonlinearity in attitude dynamics.

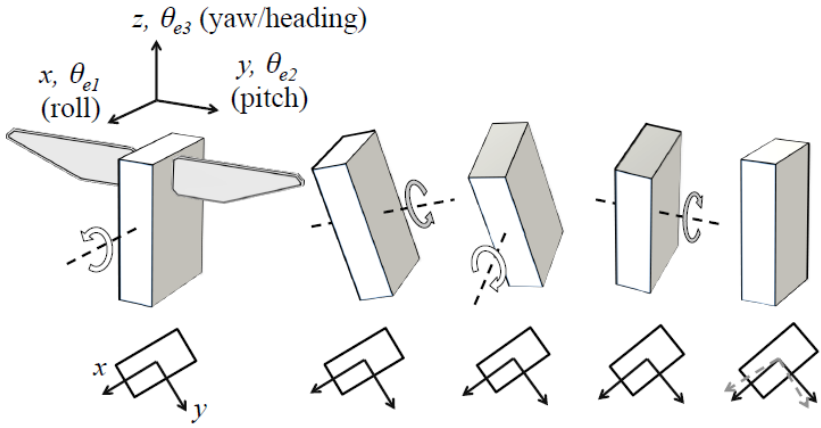

Fig. 59 Wriggle steering: a change in heading results from performing consecutive cycles of small roll and pitch manoeuvres because of the nonlinearity in attitude dynamics. For this yaw-method no active control of the wing rotation is required.

Performing flight manoeuvres by other means than an asymmetric wing motion
Besides the asymmetric wing motions listed in Table 15 other principles of performing flight manoeuvres or achieving stable flight are described in literature. Using an active tail for example like applied in the Mentor **[Zdunich et al, 2007]** or the Delfly **[Delfly, 2017]** or using a counter weight with a variable position relative to the centre of mass as was proposed in **[Yan et al, 2001]**.

Active or passive wing rotation
The rightmost column of Table 15 states if active wing rotation is required to perform a certain asymmetric wing motion. The design of the flapping mechanism for a robotic hummingbird becomes more complex if the wing rotation needs to be actively controlled. The resonant flapping mechanism does not actively control the wing rotation; instead, the wing rotation occurs passively as the result of the aerodynamic, inertial and elastic forces that act on the driveline and on the wing during flapping. As a consequence it cannot generate the asymmetric wing motions that are required in case of active control of the wing rotation.

As Table 15 shows, there is no need for an active wing rotation to vary thrust or to generate roll or pitch torques. It is however difficult to generate a yaw torque that is large enough to perform yaw manoeuvres without active control of the wing rotation. As a consequence the Kulibrie has not yet performed successful yaw manoeuvres. However, stable flight is possible without active control of the wing rotation, because the yaw is passively stabilised as discussed in section 5.2.2. Both the Harvard Robobee **[Ma Kevin**

et al, 2013] and the Kulibrie are capable of performing stable flight without active wing rotation.

5.4.2 FLIGHT MANOEUVRES IN NATURE

Hummingbirds and insects are the living proof of the large flight envelope and the high manoeuvrability that can be achieved with flapping wing flight. Research papers about asymmetric wing motions found in nature are scarce. The following paragraphs summarise all findings.

Roll
Ellington **[Ellington, 1999]** observed that some insects perform a roll manoeuver by a difference in stroke amplitude between left and right wing, while Hengstenberg **[Hengstenberg et al, 1986]** observed that some insects perform a roll manoeuver by a difference between the angle of attack of their left and right wings.

Pitch
Research on a free flying fruit fly revealed that the insect shifts the mean stroke angle in order to stabilise their attitude after an external pitch perturbation **[Ristroph et al, 2013]**.

Yaw
Some insects modify their angle of attack between forward and backward stroke to perform a yaw manoeuver **[Ellington, 1999]**.

Measurements on tiny fruit flies **[Ristroph et al, 2010]** reveal that they combine an asymmetry in angle of attack with a significant asymmetry in the mean stroke angle between the left and right wing. Most of the yaw torque however is attributed to the difference in angle of attack between forward and backward stroke.

Other studies attribute the yaw manoeuver of the fruit fly to “a backward tilt of the stroke plane and an increase in stroke amplitude **[Fry et al, 2003]**. A comparable wing motion was observed on the Annas Hummingbird by **[Altshuler et al, 2012]**. They observed that a hummingbird sustains yaw turns by expanding the wing stroke amplitude of the outer wing during the down stroke and by altering the deviation of the wing tip path during both down stroke and upstroke.

5.5 MECHANICAL RECONSTRUCTION OF ASYMMETRIC WING MOTIONS

The mechanical generation of an artificial asymmetric wing motion is one of the main challenges of developing a robotic hummingbird. The most common approach is to add several extra actuators to the flapping mechanism that adjust the wing motion in order to generate roll, pitch and yaw torques. The flapping mechanism becomes more complicated and the extra actuators and mechanical components add a considerable amount of mass to the robot. Currently only the 7 prototypes mentioned in Table 1 have been successful in controlling at least two of the three rotational degrees of freedom. Only the Nano hummingbird and the robotic hummingbird developed at the University of Maryland succeeded in controlling all of them. The next sections first describe which principles from Table 15 the existing robotic hummingbirds use to generate roll, pitch and yaw torques. The final section explains the principles of asymmetric wing motion which are implemented in the Kulibrie and how they are generated.

5.5.1 STATE OF ART

The currently existing robotic hummingbirds that are able to (partially) stabilise their flight by means of an asymmetric wing motion are summarised in Table 1 in chapter 1. Here, the asymmetric wing motions of three of these robotic hummingbirds will be discussed, because the asymmetric wing motions of the others are similar.

The Nano Hummingbird

In **[Keennon et al, 2012]** two different control strategies are explained that were both tested. The first prototypes of the *Nano Hummingbird* were controlled using wing rotation modulations: T(α), R(α) , P(α) and Y(α) Fig. 58 illustrates the principles. Strings coupled to actuators limit the angle of attack to a certain value in both forward and backward stroke. This method proves to work but it makes a lot of noise and it reportedly has 'control precision problems'.

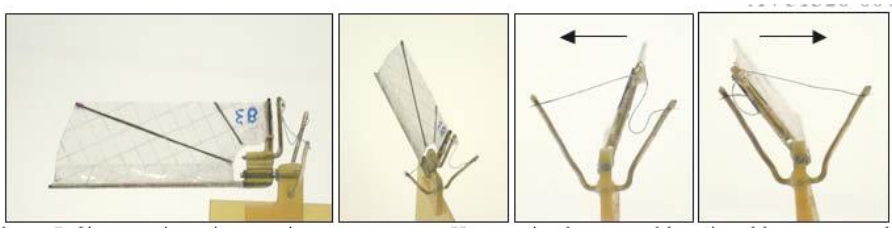

Fig. 60 Wing rotation modulation a difference in angle of attack between the forward and the backward stroke is realized by limiting the wing rotation by two cables of adjustable length. [Keennon **et al**, 2012]

This approach is abandoned in favour of wing twist modulations, as shown in Fig. 61. By rotating the root spar of the wing (indicated by the red arrow) towards the body, the tension in the wing increases and the wing twist decreases. As a consequence the thrust increases. This principle can be used to control the average thrust and the roll.

Rotation of the root spar of the wing along the length axis of the wing increases the drag on the wing during either forward or back ward stroke. This principle can be used to control the pitch and yaw.

Fig. 61 Variable wing twist modulation: a flexible membrane is suspended between the leading edge and the root spar (red arrow). If the root spar rotates away from the wing, the thrust is increased. By rotating the root spar slightly around the leading edge a difference of angle of attack is realized between the forward and the back ward stroke. [Keennon **et al**, 2012]

The researchers report that ”the wing twist modulation control system has excellent single axis controllability, and that it is not a detriment to propulsive efficiency, that it is quieter than the wing rotation system, and that it has an elegant design solution. Fig. 62 shows the final, yet complex control mechanism of the Nano Hummingbird.

Fig. 62 Control mechanics of the Nano Hummingbird [Keennon **et al**, 2012] the two separate gear trains are responsible for reducing the motor speed of two actuators that control the variable wing twist modulation. The upper part of the mechanism controls the stroke motion.

The robotic hummingbird of the University of Maryland

The robotic hummingbird of the University of Maryland **[Coleman et al, 2015]** uses a different set of asymmetric wing motions in order to maintain stability and to perform flight manoeuvres. To control thrust and roll, modulation of the stroke amplitude is used: T(A/ -) and R(A / L-R). These control principles are also used in the Kulibrie and they are discussed further in the next section. To control pitch and yaw, the stroke plane of each wing can be tilted separately. To generate a yaw torque the stroke planes of both wings are turned in opposite senses by angles β_R and β_L as shown in Fig. 63, taken from **[Coleman et al, 2015]**. To generate a pitch moment they are rotated in the same direction.

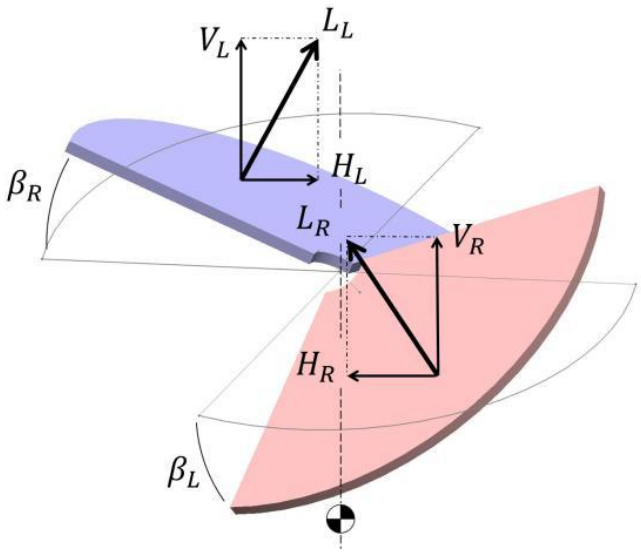

Fig. 63 Modulation of the stroke plane angle [Coleman **et al**, 2015] by tilting the stoke planes of both the left and right wing forward or backward pitch manoeuvres are generated. Yaw manoeuvres result from a difference between the tilt of the stroke planes of the left and right wing.

The Harvard Robobee

Again a different set of asymmetric wing motions is used by the Harvard Robobee. Just like with the Kulibrie, the Harvard Robobee uses a resonant mechanism and each wing is driven by a separate actuator. It is therefore no surprise that the set of asymmetric wing motions used by the Harvard Robobee are similar to the Kulibrie (see Table 15). This set of asymmetric wing motions is discussed in the next section.

5.5.2 THE ASYMMETRIC WING MOTION OF THE KULIBRIE

One of the main advantages of the resonant flapping mechanisms used by the Kulibrie is the simplicity to perform asymmetric wing motions and to generate thrust and roll and pitch torques. Several different asymmetric wing motions can be generated by merely modifying the current through the motors that drive each wing.

No extra actuators or other mechanical components need to be added to perform the flight manoeuvres. As a consequence the Kulibrie weighs considerably less than the

other robotic hummingbirds listed in Table 1. Furthermore it has a considerably lower component count, reducing the chance of failure.

Section 5.5.2.4 shows several options that are studied to generate a yaw torque, but they all have their disadvantages. The generation of a proper yaw torque remains a subject of research.

The simplicity to generate asymmetric wing motions with the resonant flapping mechanism comes with some limitations. First, it is necessary to drive each wing with a separate motor in order to perform roll manoeuvres. It is however expected to be more effective to drive both wings with one larger motor because of the adverse scaling of the torque and power to mass ratios of electric motors.

Furthermore the simple design of the resonant flapping mechanism limits the set of possible asymmetric wing motions:

- Because the wing rotation is not actively controlled it cannot be used to control flight, and consequently the flight parameters Tα, Rα, Pα and Yα (see Table 15) cannot be controlled by the resonant flapping mechanisms of the Kulibrie.
- Because the power consumption of the resonant flapping mechanism is highly dependent on the flapping frequency (as shown in chapter 4) modulations of the flapping frequency in order to perform asymmetric wing motions should be avoided if possible. As a consequence flight parameters Tf, Rf, Pf and Yf should be avoided.
- To avoid having to implement extra actuators Rδ, Pδ and Yδ should be avoided.

This leaves only a few options to directly control thrust and to generate roll, pitch and yaw torques.

Average thrust

The average thrust (which defines the vertical acceleration) is successfully controlled by varying the stroke amplitude (TA) of both wings symmetrically as shown in Fig. 64. The average thrust is increased by increasing the stroke amplitude. To increase the stroke amplitude of both wings, the amplitude of the alternating current through the motors of the resonant flapping mechanisms is increased. The same principle is used by hummingbirds, by the Harvard Robobee **[Ma Kevin, 2013]** and by the robotic hummingbird of Maryland **[Coleman, 2015]**.

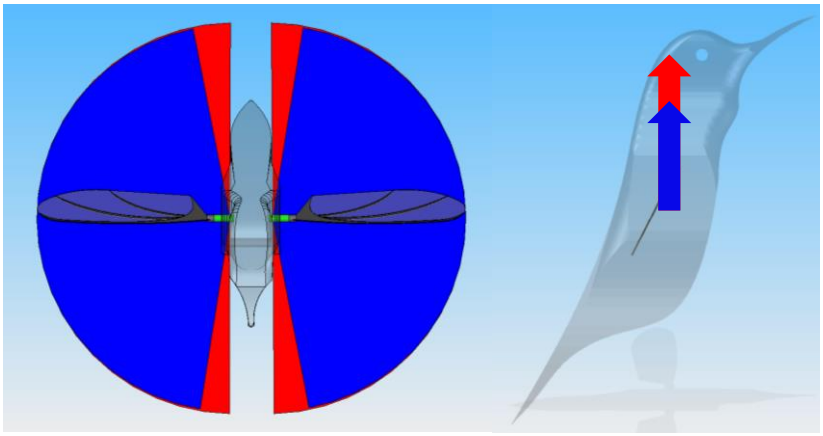

Fig. 64 Thrust modulation of the Kulibrie: The amount of thrust made by the wings of the Kulibrie can be modified without influencing roll, pitch or yaw by modifying the stroke amplitude.

Fig. 42 in chapter 2 shows the influence of the stroke amplitude on the average thrust generated by one wing. The figure shows that a near linear relation exists between stroke amplitude and the average thrust generated. This method varies the average thrust independently of roll, pitch and yaw.

Roll: R(A/L-R)

Roll is successfully controlled by imposing a left-right asymmetry of the stroke amplitude as shown in Fig. 65. In order not to affect the average thrust, the amplitude of one wing is increased while the amplitude of the other wing is decreased. A positive roll torque is generated when the amplitude of the left wing is increased. A difference in stroke amplitude between both wings is obtained by imposing a different amplitude of the alternating current between both motors of the resonant flapping mechanisms.

The same method is used by the Harvard Robobee **[Ma Kevin, 2013]** by and the robotic hummingbird of Maryland **[Coleman, 2015].**

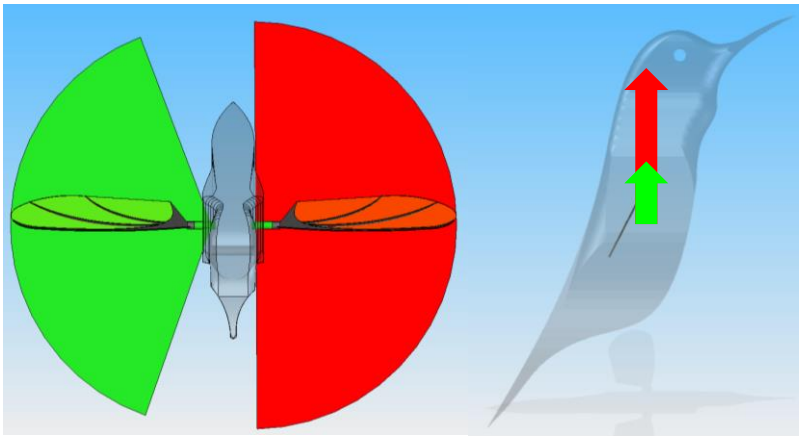

Fig. 65 Roll manoeuvres of the Kulibrie: The Kulibrie performs a roll manoeuvre by a difference in stroke amplitude between the left and the right wing.

Because of the almost linear relation between the average thrust that is generated by each wing and the stroke amplitude of each wing, the increase in amplitude of one wing should be nearly equal to the decrease of amplitude of the other wing. An almost linear relation would exist between the difference in stroke amplitude and the roll torque that is generated. This method varies roll independently of thrust, pitch and yaw.

Pitch: P(ϕ/F-B)
Pitch is successfully controlled by adjusting the mean stroke angle (ϕ) of both wings symmetrically as shown in Fig. 6671. A positive pitch torque is generated when the mean stroke angle is negative and vice versa.

The same principle to generate pitch torques is applied by fruit flies and by the *Harvard Robobee* **[Ma Kevin, 2013]**.

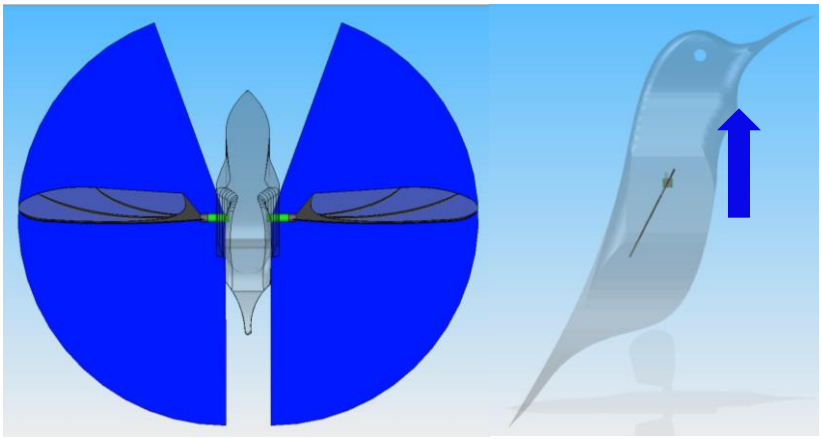

Fig. 66 Pitch manoeuvres of the Kulibrie: The Kulibrie performs a pitch manoeuvre by a modulation of the mean stroke angle. A non-zero mean stroke angle results in a change of the position of the average thrust.

A modification of the mean stroke angle only changes the position where the thrust force is applied which is generated by each wing relative to the centre of mass of the robotic hummingbird. As a consequence the pitch torque varies linearly with the mean stroke angle (for small mean stroke angles). Because the direction and the magnitude of both thrust vectors T_R and T_L remain unchanged, a pitch manoeuvre like this one does not directly affect the average thrust generated by both wings. This principle varies pitch independently of thrust roll and yaw.

Yaw

The generation of a yaw torque of sufficient magnitude that is independent of thrust, roll and pitch remains an unsolved problem with the resonant flapping mechanism used in the Kulibrie. The same issue is raised by the research team that develops the *Harvard Robobee*. Several methods to generate a yaw torque have been tested on the Kulibrie. These principles are tested on a prototype that was either flying freely or that was hold by hand. On a flying prototype of the Kulibrie, a proper yaw torque should be capable of compensating undesired yaw rotations.

Split frequency modulation: Y(f' / F-B & L-R)

Split frequency modulation of the wing motion results in a yaw torque, but it is not recommended to adopt this as the only option to generate yaw torque. The yaw torque generated by split frequency modulation proves to be too small to overcome unintended yaw motion of a free flying Kulibrie.

Furthermore no successful stable flight could be accomplished from the moment split frequency modulation is enabled. This observation may be explained by the fact that split frequency modulation also influences the average thrust, roll and pitch.
A third issue is that the motors overheat because split frequency modulation forces the wings to flap at frequencies that do not coincide with the resonance frequency of the system.

Wriggle Y(A & ϕ / F-B & L-R)
The wriggle method can be a valid alternative to generate proper yaw torques. This method however is not yet tested. Wriggle steering can save mass and reduce complexity by eliminating the need for additional actuators.

Y(ϕ / F-B & L-R) and Y(ϕ => ζ / F-B & L-R)
A asymmetrical change of the mean stroke angle as proposed in **[Karasek & Preumont, 2014]** does not result in any noticeable yaw torque. However if the rubber that is used to assist the wing rotation is not attached to the shoulder gear (as it was in earlier prototypes) but to the body, a modification of the mean stroke angle results in a slight difference between the forward and the backward motion of the wing which generates a yaw torque. The difference in the wing motion can be explained as follows:

Imagine a non-zero mean stroke angle such that a larger elongation of the rubber during forward stroke than during backward stroke is obtained. Because the elastic force will be greater for a larger elongation of the rubber, a slightly faster and more advanced wing rotation can be expected at the end of the forward stroke compared to the ones at end of the backward stroke.

5.6 CONTROL SYSTEM

To actively stabilize and control the flight a robotic hummingbird requires a control system that actively controls the wing motion of the robotic based on the pilot's inputs and the information from on-board motion sensors (section 5.6.2). The control design consists of a hardware part: the flight controller (section 5.6.1) and a software part: the control algorithm (section 5.6.3)

5.6.1 THE FLIGHT CONTROLLER

All revisions of the avionics utilise commercial-off-the-shelf (COTS) components on custom-designed circuit boards. The main elements of the avionics are a microcontroller unit (MCU) to manage all electrical systems, microelectromechanical systems (MEMS) gyroscopes and accelerometers (3 axes) for stability augmentation, a wireless receiver for obtaining commands from a pilot, driver circuits to operate the actuators, magnetic encoders that measure the stroke motion of each wing and components for DC power

conversion. This collection of core components is referred to as the flight controller. Fig. 67 shows the current version of the flight controller.

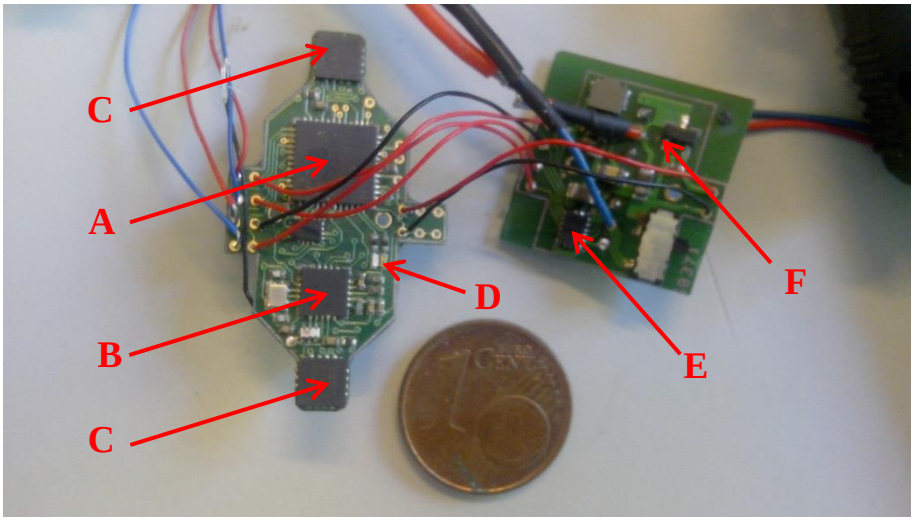

Fig. 67 Latest revision of the flight controller: **The flight controller consists** of a microcontroller (A), a wireless transceiver (B), Mems motion sensors **(at** the back of the left PCB), **Magnetic encoders (C), indicator LEDs (D), a motor driver (E) and power electronics (F).**

Microcontroller

The microcontroller, an *UC3L0256* from *Atmel,* is the central component of the flight controller. It runs the software required to control the robotic hummingbird, receives the output of all the sensors and sends the appropriate motor signal to the motor driver and the indicator LEDs. This microcontroller was selected in 2015. In meanwhile several other microcontrollers became available that have better specifications. Learning to know the operation of a certain microcontroller is a time consuming endeavour that kept us from switching to a more recent microcontroller.

Wireless transceiver

The nrf24L0+ bi-directional wireless transceiver of *Nordic* is used to send data from a ground station (controller) to the robotic hummingbird (for example the desired thrust) and to send data from the robotic hummingbird to the controller (for example the data from the motion sensors).

Besides the manual input from the pilot to control upward, forward, sideways and yaw manoeuvers also other data can be transmitted wirelessly from a graphical user interface programmed in *Labview,* for example data used to adjust the control algorithm.

Every wing beat cycle 13 bytes of information are sent to the Kulibrie and one byte is send to the controller. This component could be replaced by a more recent and better alternative, for example a *Bluetooth* transceiver.

MEMS motion sensors
The MEMS motion sensors implemented in the Kulibrie will be discussed in the next section.

Magnetic encoders
The stroke angles of both the wings of the Kulibrie are measured during flight by the same sensors described in section 8.4.2. The stroke angle serves as an input for the control algorithm, which will be discussed in section 8.11.1.

Indicator LEDs
The indicator LEDs are used to indicate any event that can be programmed in the software.

Motor driver
A DRV8833 motor driver of TI is used to drive both motors. This motor driver is used because the microcontroller cannot drive the motors directly due to the large currents that are required.

5.6.2 MEMS MOTION AND ORIENTATION SENSORS

Because a robotic hummingbird is not passively stable and its motions are too fast to be corrected manually by a human pilot, sensors that sense motion and orientation are required to actively stabilize and control the flight of a robotic hummingbird.
Research on insects revealed that in order to maintain stability insects use structures called halteres which detect body rotational velocities by measuring gyroscopic forces, much like mechanical gyroscopes **[Schenato, 2003]**.
MEMS (microelectromechanical systems) motion sensors, like the one shown in Fig. 68, are small and light enough to be implemented in a robotic hummingbird; they often weight less than 100 milligrams.

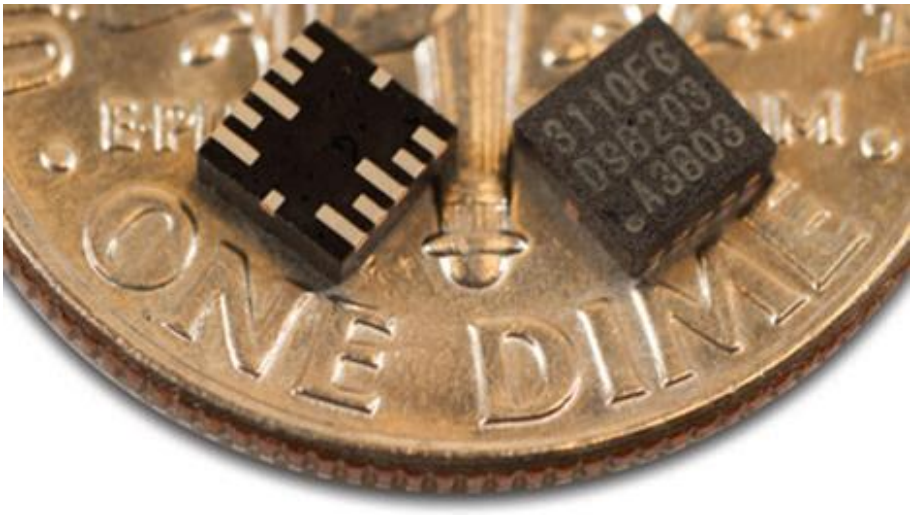

Fig. 68 Mems motion sensors

Billons of these sensors are used in consumer electronics like smartphones, but also for industrial and automotive applications. They are used in professional quadcopters but also in toy helicopters to stabilize flight. Every month new sensors become available, that perform better than their predecessors.

Not much literature exists about the implementation of MEMS motion sensors in robotic hummingbirds, but from **[Keennon et al, 2012]** and from our own experience we know that many MEMS motion sensors are not sufficiently performant to stabilize the flight of a robotic hummingbird. .

Especially the back and forth rocking of a robotic hummingbird (caused by the wing motion) complicates the use of MEMS motion sensors, because it generates a relative large amount of noise compared to quad copters for example.

TYPES OF SENSORS

Three types of MEMS motion sensors are commonly used in small drones; they are often combined into one component.

- **Gyroscopes**: measure the motion (angular rate) of a drone around one, two or three orthogonal axes
- **Accelerometers**: measure the acceleration of a drone along one, two or three orthogonal axes. By measuring the gravitational acceleration (of which the size,

orientation and direction are known), the absolute orientation of a drone can be defined.

- **Magnetometers**: to measure the absolute heading of a drone in the horizontal plane by measuring the magnetic field of earth

Only gyroscopes and accelerometers have been implemented in the Kulibrie so far.

5.6.1.1 CRITERIA

Table 16 shows the main characteristics of the MEMS motion sensors that are tested on the Kulibrie. These characteristics are taken from the data sheets. Many more sensors were considered but not tested because the information in their datasheets clearly suggested that they would perform worse than the ones in Table 16.
The sensors are tested by holding the Kulibrie by hand and letting the wings flap. Although a better, more consistent test method can be developed, tests like these allowed us to compare sensors.

Size

The relevant size of the sensor is the footprint or surface area it requires on the printed circuit board (PCB). The smaller the footprint is, the lower the weight of the avionics.
The footprint of a MEMS sensor is not only defined by the actual size of its package, but also by the amount of extra components (capacitors and resistors) that the sensor requires to properly function.
MEMS sensors become increasingly smaller. The first sensor that we tested, the *MPU 6050* from *Invensens (may 2014)*, has a footprint that is almost twice the size of the one of more recent sensors like the LSM6DSL from ST (nov 2016).

Supply voltage

The minimum supply voltage is an important criterion because the maximum voltage that can be delivered from a single lithium polymer battery as is used in the Kulibrie is about 3.7V.

Measurement range

The measurement range of a motion sensor has to be large enough such that the sensor does not go into saturation. The resolution of a motion sensor needs to be high enough to measure all the important aspects of the motion. All tested sensors have the same resolution that meets the requirements.

manufacturer	Invensense	Invensense	Invensense	Bosch	Bosch	ST	ST	Fairchild	Analog	KIONIX
type	ICM 20608	MPU 6500	MPU 6050	BMA 280	BMI 160	LSM6DS3	LSM6DSL	FIS1100	ADXL344	KX022
extra components	4	2	4	1	1	1	1	1	1	1
SPI speed (Hz)	8M	20M	20M	10M	10M	10M	10M	10M	5M	10M
Package size (mm)	3*3	3*3	4*4	2*2	2,5*3	2,5*3	2,5*3	3,3*3,3	3*3	2*2
price (€ per 3000)	3,92	4,62	5,2	1,03	2,07	1,95	1,95	3,48	1	0,97
minimal supply voltage (V)	1,71	1,71	2,4	1,62	1,71	1,71	1,71	2,4	1,7-2,75	1,8
Gyro	3	3	3	/	3			3	/	/
Range (°/s)	2000	2000	2000	/	2000	2000	2000	2560	/	/
resolution (bit)	16	16	16	/	16	16	16	16	/	/
noise sensitivity[°/s/sqrt(Hz)]	0,008	0,01	0,005	/	0,007*	0,007	0,0045	0,010	/	/
max data output rate (Hz)	8K	8K	8K	/	3,2K	1666 (3332)	6664	1K	/	/
Accelero	3	3	3	3	3			3		3
Range (g)	16	16	16	16	16	16	16	8	16	8
resolution (bit)	16	16	16	14	16	16	16	16		16
Noise sensitivity [ug/sqrt(Hz)]	250	300	400	120	180**	90	90	50	?	100
max data output rate (Hz)	4K	4K	1K	2K	1,6K	6,6K	6664	1K	3200	1,6K

Table 16: Tested MEMS gyroscopes and accelerometers

Noise sensitivity

The noise sensitivity determines to which extent a sensor is influenced by the flapping vibration. All manufacturers have their own way of defining the noise sensitivity of a motion sensor. As a consequence, the noise sensitivity of sensors of different manufacturers cannot be compared by only considering the information in the data sheets. Therefor it is necessary to test new sensors on a flapping prototype to measure their sensitivity to the flapping vibration.

Most sensors go into saturation because they are too sensitive to the flapping vibration as a consequence only two sensors are well suited: the BMA accelerometer of Bosch and the LSM6DSL gyroscope of ST.

5.6.1.2 TESTING NEW SENSORS

To facilitate the testing of new sensors on the Kulibrie without having to replace all avionics, a motherboard is designed comprising all the electronic components except of the sensors (Fig. 69). Every sensor is soldered on a tiny separate PCB that can be plugged in the motherboard as shown in Fig. 69.

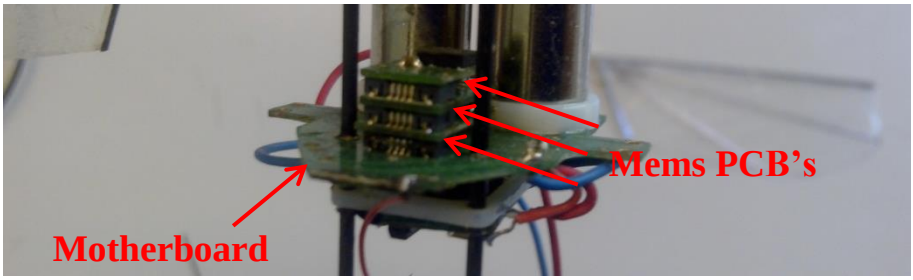

Fig. 69 Replaceable MEMS sensors, to facilitate the testing of new MEMS sensors

5.6.2 THE CONTROL ALGORITHM

A feedback control algorithm is programmed on the microcontroller of the Kulibrie. This algorithm controls the attitude of the Kulibrie by adjusting the wing motion based on the data from the motion sensors, encoders and manual input from the pilot.

For example if the robotic hummingbird tilts too much to the right due to a wind gust the control algorithm signals the motors to generate a roll torque that counteract this disturbance.

Roll and pitch are controlled independently while yaw control has not yet been implemented. In the case of pure hovering flight without forward or sideways velocity, the desired roll and pitch angles are zero.

The Motor inputs for the left motor (V_L) and the right motor (V_R) are given by the equations 5.1 and 5.2 respectively;

$$V_L = \phi + A_L \cos(2\pi f \Delta t) \quad \text{eq. 5.1}$$
$$V_R = \phi + A_R \cos(2\pi f \Delta t) \quad \text{eq. 5.2}$$

V_L and V_R are digital signals ranging from -127 to 128 and are linearly converted by the motor driver to an armature voltage between $-V_{source}$ and $+V_{source}$ with V_{source} the voltage of the battery.

Three parameters are varied in order o generate the appropriate thrust, and roll and pitch torques: the mean stroke angle ϕ defines the pitch torque by performing a P(ϕ / F-B) and the difference between the stroke amplitude of the left wing (A_L) and the right wing (A_R) defines the roll torque by performing a R(A / L-R).

The appropriate ϕ , A_L and A_R are determined using feedback control based on digital proportional–integral–derivative (PID) algorithms. In what follows the control algorithm that determines A_L and A_R is explained. The same control algorithm is used for ϕ.

Desired stroke amplitude

In a first step the desired amplitude for the stroke amplitude of the left wing (AD_L) and the right wing (AD_R) are determined (equations 5.3 and 5.4):

$$AD_L = AT_p - A\_Roll_p + A\_Roll_{imu} - A\_Roll_{cal} \quad \text{eq. 5.3}$$
$$AD_R = AT_p + A\_Roll_p - A\_Roll_{imu} + A\_Roll_{cal} \quad \text{eq. 5.4}$$

AD_L and AD_R are determined by:

- the pilot commands: AT_p that sets the amplitude to control the altitude and A_Roll_p that sets the required amplitude adjustment to control sideways motion,
- A_Roll_{imu} : the amplitude adjustment required to stabilize flight determined by the motion sensors
- and a calibration constant: A_Roll_{cal} to compensate any offset due to asymmetries in the wings.

Inner PID loop

Next, the appropriate A_L and A_R are each calculated by a separate (PID) controller that uses the measurement data from the encoders. Equations 5.5 to 5.9 show the implementation of the PID controller for A_L. The PID controller for A_R is implemented in a similar fashion.

$$e_{AL} = AD_L - AM_L \quad \text{eq. 5.5}$$
$$\dot{e}_L = e_{AL} - e_{AL-old} \quad \text{eq. 5.6}$$
$$E_{AL} = E_{AL} + e_{AL} \quad \text{eq. 5.7}$$
$$A_L = Kp_{AL} \cdot e_{AL} + Ki_{AL} \cdot E_{AL} + Kd_{AL} \cdot \dot{e}_{AL} \quad \text{eq. 5.8}$$
$$e_{AL-old} = e_{AL} \quad \text{eq. 5.9}$$

The control error (e_{AL}) is determined as the difference between the desired stroke amplitude and the measured stroke amplitude (equation 5.5).

A_L is determined in equation 5.8 as the sum of three terms: one term proportional to the control error, one term proportional to the integration of all previous control errors (E_{AL}) and one term proportional to the difference of the last two control errors ($\dot{e_L}$).

The appropriate PID constants (Kp_{AL}, Ki_{AL} and Kd_{AL}) are determined experimentally according to the method described in **[Liang et al, 2017]**
The proportional to $\dot{e}_L$ is omitted ($Kd_{AL} = 0$) in the controller of the latest prototype of the Kulibrie to reduce the sensitivity of the controller to noise. By doing so, a PI controller is obtained.

The roll amplitude (A_Roll_{imu}) and the pitch amplitude (A_Pitch_{imu}) that were introduced in equations 5.3 and 5.4 are each calculated by a separate PID algorithm that uses the angular roll velocity (ω_R) and he angular pitch velocity (ω_P), measured by the MEMS gyroscope and the roll angle (β_R) and the pitch angle (β_P) measured by the accelerometer. Equations 5.10 to 5.13 show the implementation of the PID controller for A_Roll_{imu}. The PID controller for A_Pitch_{imu} is implemented in a similar fashion.

$$e_{A\_Roll_{imu}} = -\beta_R \qquad \text{eq. 5.10}$$

$$\dot{e}_{A\_Roll\_imu} = -\omega_R \qquad \text{eq. 5.11}$$

$$E_{A\_Roll\_imu} = E_{A\_Roll\_imu} + e_{A\_Roll\_imu} \qquad \text{eq. 5.12}$$

$$A\_Roll_{imu} = Kp_{A\_Roll\_imu} \cdot e_{A\_Roll\_imu} + Ki_{A\_Roll\_imu} \cdot E_{A\_Roll\_imu} + Kd_{A\_Roll\_imu} \cdot \dot{e}_{A\_Roll\_imu} \qquad \text{eq. 5.13}$$

To assure that the Kulibrie performs a pure hovering flight if no roll or pitch command is given by the pilot, the desired A_Roll_{imu} (and A_Pitch_{imu}) are zero. Furthermore, as seen in chapter 3, the roll torque of a R(A/L-R) flapping asymmetry varies approximately linearly with the difference in stroke amplitude between the left and the right wing. As a consequence the control error ($e_{Roll_{imu}}$) is proportional to the roll angle (β_R) measured by the accelerometer and the derivative error of the roll angle ($\dot{e}_{A\_Roll\_imu}$) is proportional to the angular roll velocity ω_R.

Currently only the data from the gyroscopes are used, because the accelerometer has not yet been implemented. By doing so, the PID controller on the roll angle becomes a D controller on the roll angle or in other words a P controller on the angular roll velocity. This P controller is able to stabilize flight according to Karasek **[Karasek & Preumont, 2014]** and as proven by the stable (but wobbly) flight of the Kulibrie **[Leys, nov 2015]**.

This control algorithm is similar to the ones used in many simple quadcopters and to the one used by the *Nano Hummingbird* **[Keennon et al, 2012]** It is thanks to the latter that we knew from the start of the development of this control system that this approach could be successful.

5.7 CONCLUSION

To increase the manoeuvrability of a robotic hummingbird, it should be **designed without a tail**, like its biological counterparts. As a consequence, active and independent control of thrust, roll, pitch and yaw is required to stabilise the attitude of a robotic hummingbird and to perform flight manoeuvres.

A robotic hummingbird can generate roll, pitch and yaw torques by performing asymmetric wing motions.

The resonant flapping mechanism generates roll and pitch torques merely by adjusting the current through the motor and without the need of extra actuators or other mechanical components that would increase the weight and the complexity of the mechanism. An independent roll torque can be generated by increasing the stroke amplitude of one wing while decreasing the stroke amplitude of the other wing. This requires that each wing is driven by a separate resonant mechanism. A pitch torque can be generated by modifying the average stroke amplitude of both wings symmetrically.

The mechanism which flaps at or close to resonance frequency, does not allow for active control of the wing rotation. Consequently no successful method to perform independent yaw manoeuvers is implemented in the Kulibrie. Implementation of an active wing rotation would solve the yaw issue and would increase the flight envelope of the Kulibrie, at the cost of an increased complexity and weight of the flapping mechanism.

Several revisions of a custom made PCB are developed that contain the avionics of the Kulibrie. The latest version comprises: a microprocessor, a motor driver, a wireless transceiver, two indicator leds, two magnetic encoders to measure the stroke amplitude and mean stroke angle of each wing and several MEMS motion sensors that measure the angular velocity. Only a few MEMS are performant enough. The others go into saturation because of the vibration caused by the flapping wing motion.

A feedback control algorithm is programmed on the microcontroller of the Kulibrie. This algorithm, which comprises several PID algorithms, controls the attitude and the altitude of the Kulibrie by adjusting the wing motion based on the data from the motion sensors, encoders and manual input from the pilot.

6 THE DEVELOPMENT OF THE KULIBRIE, A ROBOTIC HUMMINGBIRD

6.1 INTRODUCTION

The aim of this PhD. is to develop a robotic hummingbird. This chapter describes how this robotic hummingbird, called the Kulibrie is developed. First a chronological overview is given from the development of the Kulibrie (6.2) after which the current status is described (6.3). In the following section the process of optimizing the flapping wing mechanism for the Kulibrie is described together with the final choice for motors, gearboxes and springs (6.4). Sections 6.5 to 6.7 describe how the frame, shoulders and wings are built. The last section before the conclusion of this chapter describes a series of flight tests that were performed in order to obtain stable flight of the Kulibrie (6.8).

6.2 CHRONOLOGICAL OVERVIEW

Table 19 shows the milestones in the development of the robotic hummingbird in chronological order. The development of this robotic hummingbird started in the framework of a master thesis **[Leys, 2011]** and is further elaborated as part of this PhD. Two different flapping mechanisms have been developed. The first prototypes of the robotic hummingbird used the stroke-cam flapping mechanism. After December 2014 the stroke-cam flapping mechanism is replaced by the resonant flapping mechanism.

6.2.1 2011 – 2013: THE STROKE-CAM FLAPPING MECHANISM

The first prototype of the stroke-cam mechanism (Fig. 72A) was developed in January 2010. Fig. 72B shows the state of the development at the start of this PhD.

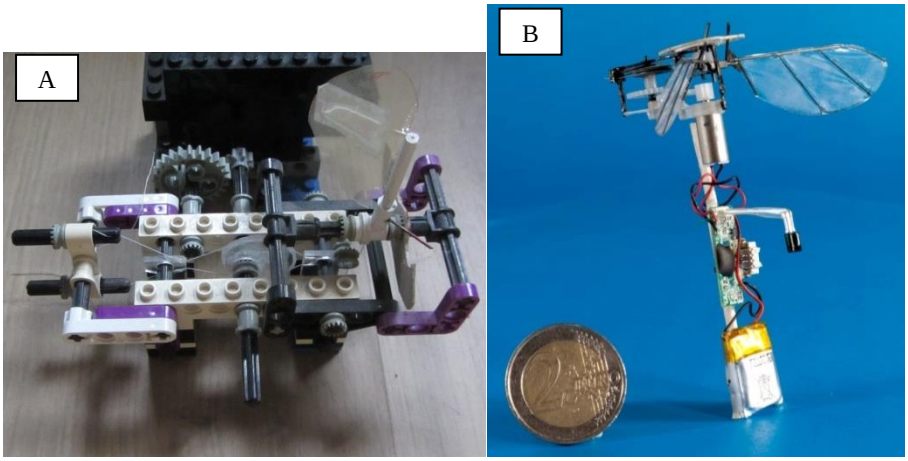

Fig. 70 The stroke-cam flapping mechanism: (A) the first version made in 2010 (B) the version of the stroke-cam mechanism at the start of this PhD. research

From November 2011 to November 2013 the stroke-cam mechanism was further improved to the prototype in Fig. 73B. This prototype was able to lift its own weight including battery and rudimental flight electronics. The prototype could not actively control flight, because the difficulty to implement asymmetric wing motions to the stroke-cam flapping mechanism. Furthermore the stroke-cam mechanism proved not to be robust enough to withstand more than a couple of minutes of flight before failure of one of the components.

After the first prototype of the resonant flapping mechanism (Fig. 73A) was developed in December 2013, the decision was made to end the further development of the stroke-cam flapping mechanism.

6.2.2 2014 - 2017: THE RESONANT FLAPPING MECHANISM

Fig. 73 shows the successive generations of the robotic hummingbird since the introduction of the resonant flapping mechanism. The improvements that distinguish each generation of the previous one are described by the pink rows in Table 19. The blue rows describe the milestones in the progress towards flight of the Kulibrie while the green rows describe the successive versions of the flight electronics of which some are shown in Fig. 74.

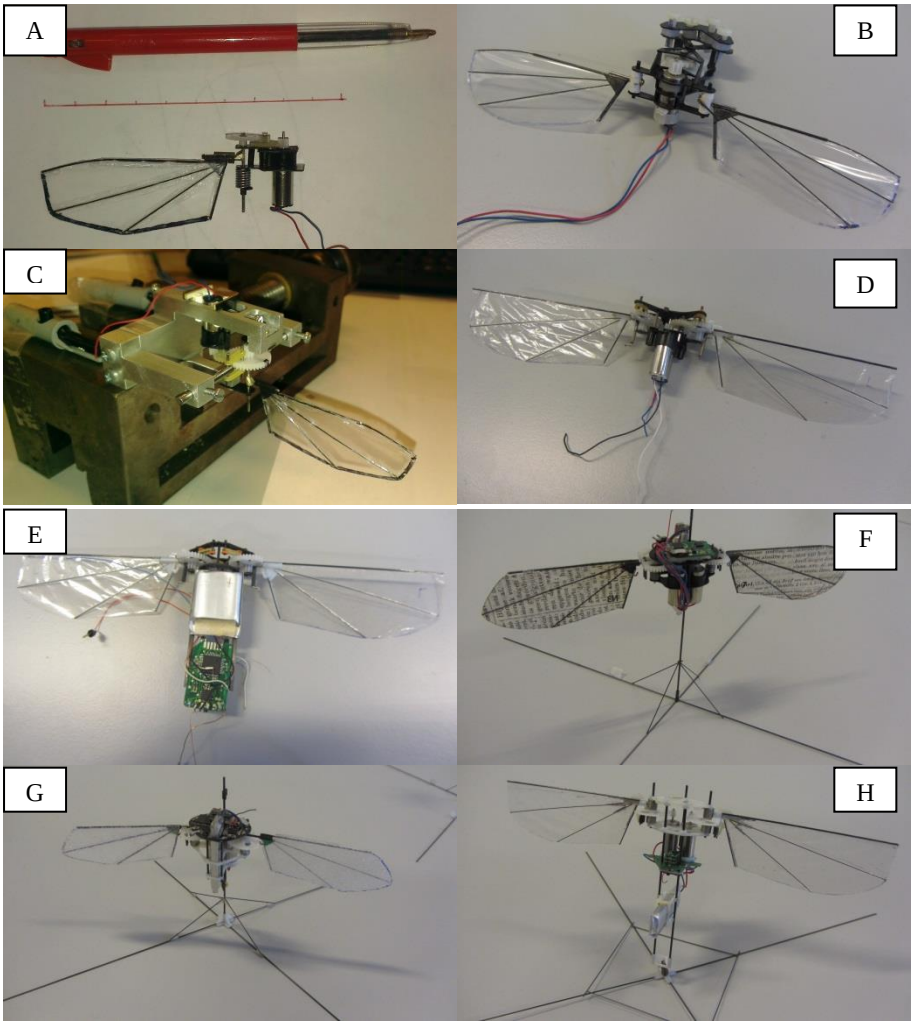

Fig. 71 The evolution of the Kulibrie: Table 19 explains the successive innovations in the design of the Kulibrie

11/12/2013	First prototype of resonant flapping mechanism (fig. A)
16/02/2014	First experimental setup of resonant flapping mechanism with rubbers (fig. B)
25/02/2014	First generation of Kulibrie with resonance mechanism (fig. X)
30/05/2014	First cable-assisted take off with resonant flapping mechanism, without battery or control electronics
19/06/2014	First tests of roll and pitch torque generation (video A)
25/08/2014	Brain 1 (fig E)
7/10/2014	Second generation of Kulibrie: with improved gearbox and on-board battery powered avionics (fig. X)
9/10/2014	First cable-assisted take off with on-board, battery powered avionics
26/11/2014	Brain 2: size reduction (fig E)
9/12/2014	Third generation of Kulibrie: replacement of rubbers with wire wound springs
18/12/2014	first tailed free flight (video B)
29/01/2015	successful implementation of roll PID control on test stand
3/03/2015	Fourth generation of Kulibrie: 3D printed body parts results in improved production repeatability
2/04/2015	free flight roll and pitch PID stabilization in 2D constrained flight setup (video C)
24/04/2015	Brain 3: PCB becomes part of the mechanical frame to reduce weight (fig E)
19/05/2015	first successfully controlled free flight (10s)
8/09/2015	Brain 4: implementation of second motion sensors (fig E)
14/11/2015	Fifth generation of Kulibrie: double spring prototype (fig. X) and movable battery
29/11/2015	improved flight control results in a 25s flight
24/01/2016	Brain 5: with 3 replaceable motion sensors
19/02/2016	improved flight control results in a 55s flight
3/01/2017	Brain 6: with 2 encoders to measure the stroke motion of both wings
16/01/2017	Sixth generation of Kulibrie: predictable flight control (Video C)

Table 17 Milestones: The milestones in the development of the Kulibrie in chronological order

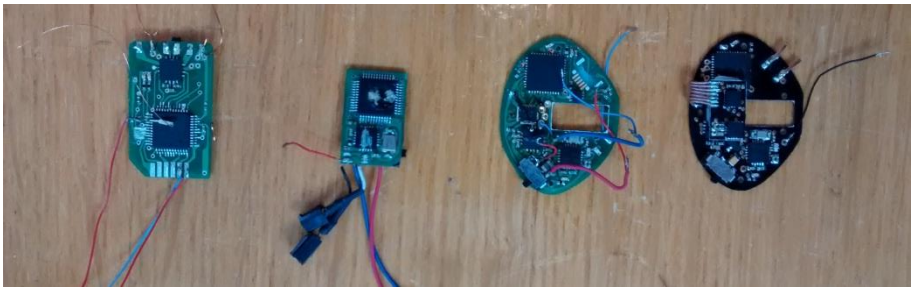

Fig. 72 The Control electronics of the Kulibrie: From left to right four consecutive versions of the control electronics of the Kulibrie.

6.3 CURRENT STATUS

6.3.1 SPECIFICATIONS

Fig. 75 shows the latest generation of the Kulibrie, developed in January 2017. Table 19 gives an overview of its specifications.

	Kulibrie (jan 2017)	Nano Hummingbird (Saturn 2010)
wing span (mm)	186	158
wing length (mm)	80	6,8
aspect ratio	3.19	2.61
mass (g)	14,1	17,5
flapping frequency (Hz)	25	27,5
stroke amplitude (°)	160 - 180	180
power consumption of flapping mechanism (W)	3,03	1,74
performance (g/W)	5,8	8,4

Table 18 Specifications of the Kulibrie compared with the Nano Hummingbird: The Kulibrie is slightly larger in span width but considerably lighter. The Nano Hummingbird consumes almost twice the amount of power as the Kulibrie.

The resonant flapping mechanism is able to generate a wing motion that generates enough thrust to lift the Kulibrie and to allow active flight control.

The simple design results in a prototype that weights 19% less than the Saturn version of the Nano Hummingbird which is regarded as the state of art in robotic hummingbirds. Flight tests showed that the Kulibrie is robust enough to withstand multiple crashes, some from over 3m height.

Due to resonance, the power consumption is 22% less compared to the same flapping mechanism without resonance. Compared to the Saturn version of the Nano Hummingbird, the performance of the latest version of the Kulibrie is 45% higher.

6.3.2 FLIGHT CONTROL

The latest generation of the Kulibrie is able to perform stable, but wobbly flight as shown in **[Kulibrie, 2017]**. The longest flight recorded lasted 55s, before the flight became too wobbly to stay aloft.

The altitude and the roll and pitch are actively controlled by asymmetric wing motions. The average thrust (altitude) is varied by adjusting the stroke amplitude of both wings, roll manoeuvers are performed by a difference in stroke amplitude between the left and the right wing and pitch manoeuvers are performed by adjusting the average stroke angle of both wings.

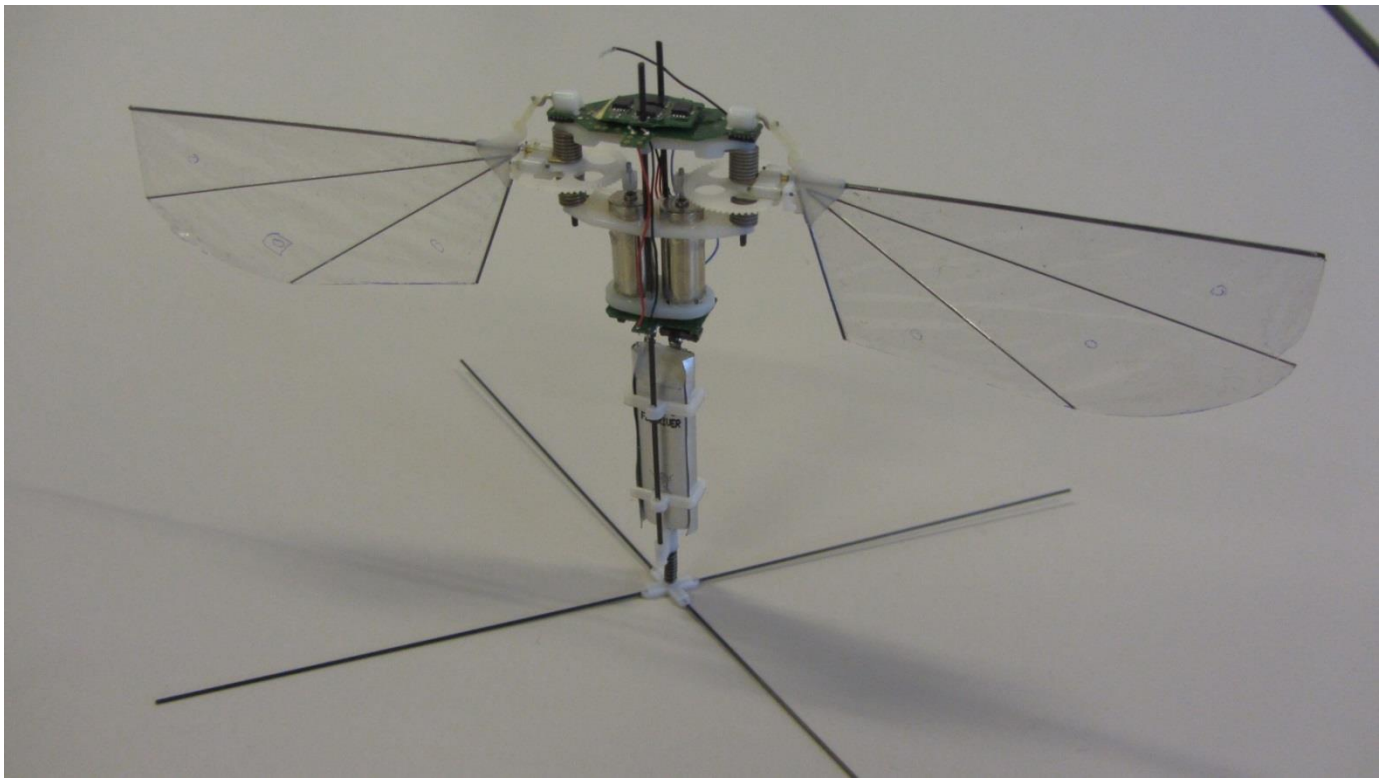

Fig. 73 The Kulibrie (January 2017, span width 186mm

6.4 SELECTING AND OPTIMIZING THE COMPONENTS FOR THE RESONANT FLAPPING MECHANISM

During this research the design of the flapping mechanism of the robotic hummingbird has been improved systematically by an experimental approach. Whenever a new design idea arises it is implemented and compared with the old design concept ceteris paribus. If the new design idea proves to perform better, it is kept.

6.4.1 SIMPLIFIED MEASUREMENT SETUP AND PROCESS

The simplified measurement setup

To evaluate the performance a simple version of the measurement setup described in section 3.4.2 is used on a daily base. This simplified measurement setup allows to compare quickly the average thrust and the power consumption of two different design concepts. This measurement setup allows to measure three quantities: the average thrust, the voltage of the source and the current drawn from the voltage source. All these quantities can be instantly read out and do not require any post processing of the measurements. The average thrust is obtained in the same way as described in section 3.4.2 and the voltage and current supplied by the source are displayed on the power source. During this research thousands of measurements like this have been performed to optimize the design of flapping mechanism and wings. Unfortunately, the results of these measurements have never been properly documented.

The simplified measurement process

In general these experiments followed the following procedure which is repeated for each design alternative.

1. Because the optimal frequency is dependent on many design parameters, the first step is to search the optimal flapping frequency for a certain combination of flapping mechanism and wing. This is done by following steps 2 and 3:
2. The armature voltage is turned up carefully until the wing flaps with a stroke amplitude of about 140° (the exact value does not matter).
3. The flapping frequency is varied manually to find the optimal frequency at which the current is minimized and the average thrust is maximized (almost always the same value). Varying the flapping frequency changes the stroke amplitude.
4. At this optimal flapping frequency the armature voltage is again increased to a certain value, such that the stroke amplitude is about 160° at which point the voltage, current and the average thrust are read out.
5. Usually a strobe is used to view the wing motion in slow motion to evaluate the wing motion qualitatively.

For each design alternative steps 1-5 are repeated. With the exception that in step 4 the same voltage is used for each design alternative. The best design alternative is the one that generates the highest average thrust and consumes the least amount of current.
This measurement process is used to compare different motors, gearboxes, springs and wings.

6.4.2 THE MOTOR

A brushed coreless dc motor is used to drive the resonant flapping mechanism. It is found to give optimum performance in this set-up. The only alternative that has been considered is a brushless out runner motor. Brushless out runner motors can produce a larger torque, but they have a much larger inertia, and this property eliminates the brushless out runner motor.

Coreless brushed dc motors are the most common type of small electric motors. They are used in many different applications, like for example in small quadcopters. They are readily available in many different sizes.

The torque that is delivered by a coreless brushed dc motors depends on the armature current (i) through the motor:

$$\tau = K_i \, i \qquad 4.4$$

With K_i the torque constant of a motor that is usually given in the datasheets of the motor. This equation has been used in literature **[Campolo, 2010]** to mathematically describe the resonant flapping mechanism.

Table 10 shows the most important characteristics of several coreless dc motors that are tested during this research project.

	M0717 - 1,1	M0717 - 1,2	M0717 - 1,4	M0614 - 2
mechanical properties				
diameter (mm)	7	7	7	6
length (mm)	17	17	17	14
mass (measured, g)	2,55	2,55	2,55	1,61
Moment of inertia (gmm^2)	500	500	500	140
Moment of inertia (measured,	376	376	376	/

gmm^2)				
max output power (W)	2,3	2,1	1,8	1,37
Stall torque (mNm)	1,92	1,98	1,77	1,11
electrical properties				
nominal voltage (V)	3,4	3,4	3,4	3,4
terminal resistance (Ohm)	1,10	1,20	1,40	2,00
stall current (mA)	2705	2397	2267	1714
electro-mechanical properties				
back-EMF constant (mV/rpm)	0,07	0,08	0,08	0,07
Ki (mNm/A)	0,72	0,85	0,81	0,68

Table 19 **Motor characteristics:** The motor characteristics of 4 coreless dc motors that have been used to drive the resonant flapping mechanism. The M0717-1.2 motor performed best.

Mechanical properties

The larger a motor, the more is the power and the larger is the torque which it can deliver (stall torque), but also the larger its mass and its inertia. Motors with a diameter of 6mm and a diameter of 7mm have been tested. Because no combination of motor-gearbox-spring-wing is available for a motor with a diameter of 6mm that would be able to generate sufficient thrust to lift a robotic hummingbird, the larger motor with a diameter of 7mm is used in the Kulibrie

Electrical properties

The nominal voltage is the optimum armature voltage for which a motor is designed. All tested motors have a nominal voltage of 3.4V close to the voltage of a Lithium polymer (LiPo) battery cell (~3.7V).

The terminal resistance determines the maximum power output and the stall torque of a coreless dc motor.

Electro-mechanical properties

The torque constant K_i is described above. It is the torque to current ratio of a coreless dc motor. The higher the torque constant of a motor, the more torque it delivers for the

same amount of current. The back-EMF constant is the voltage to motor speed ratio of a coreless dc motor.

6.4.3 GEARBOX

The gearbox converts the motor speed to the desired flapping frequency. A two spur gear gearbox is chosen. The gears have a modulus of 0.3mm and the gear ratio is 10. The gear ratio of ten results from many different gear-ratios that have been tested during the scope of this research. A higher gear ratio increases the torque that can be delivered to the wing, but it increases also the equivalent inertia of the motor with the square of the gear ratio. As a consequence, the spring constant (and thus the required torque) will need to be increased to maintain the desired resonant frequency.

6.4.4 STROKE SPRING

The selection of the type and dimensions of the elastic element depend on several criteria:

- The spring stiffness
- The mass of the spring
- The lifetime of the spring: the number of flapping cycles the springs can withstand, which depends of the maximum deflection of the spring. As long as the deformation is below the endurance limit, a spring can withstand an infinite number of deflections.
- The material damping of the spring
- The price and the availability of the spring

Two different types of spring elements have been tested: rubber bands and helical torsion springs. The latter type proved to be the best option.

Rubber bands

Early prototypes of the resonant flapping mechanism were equipped with rubber bands as shown in Fig. 74 Rubbers bands of many different sizes and different stiffnesses have been tested. Although rubber bands have the advantage of a relatively low mass, they proved not to have a long lifetime, lasting only a couple of thousands of flapping cycles. Furthermore they added a substantial amount of damping to the resonant flapping mechanism.

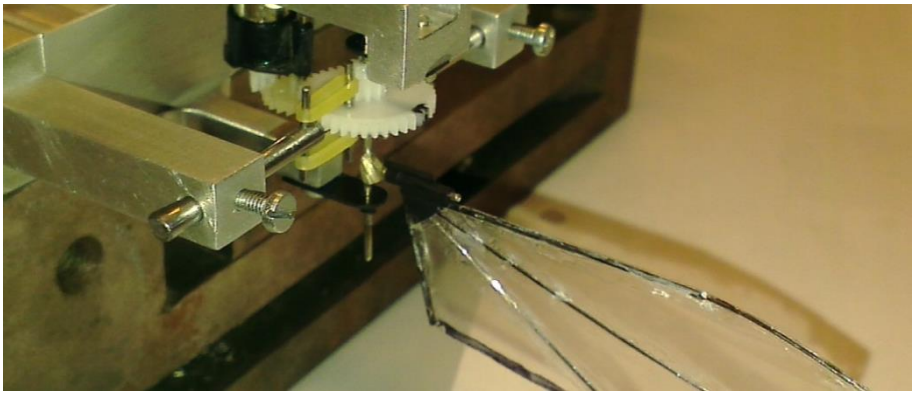

Fig. 74 **Rubbers as Elastic stroke elements:** Early resonant flapping mechanism that uses rubbers for the elastic element of the stroke motion.

Helical Torsion spring

The idea of using rubber bands is abandoned in favour of wire wound torsional springs of stainless steel. Their mass is higher (see Table 11), but if properly designed, they can withstand for an infinite number of flapping cycles and they add less damping to the resonant flapping mechanism.

Two different implementations of wire wound torsional springs have been tested, one with only one spring, as shown in Fig. 75 and the other one with two springs as shown in Fig. 76.

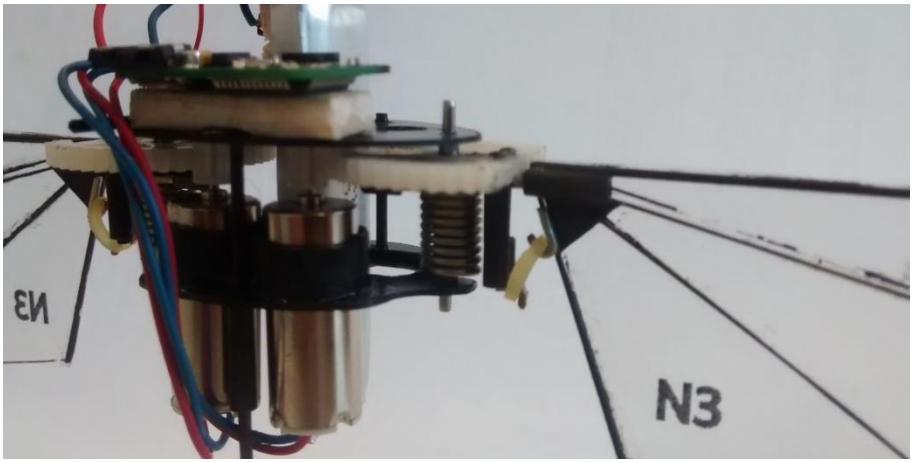

Fig. 75 **The resonant flapping mechanism with one stroke spring:** An example of a resonant flapping mechanism used in the Kulibrie that only uses one stroke spring. This setup proved to generate a slightly different wing motion in forward stroke as in backward stroke.

The implementation with two springs has two advantages. The first advantage is that the implementation of two springs results in the same stiffness in forward and backward stroke: Wire wound torsional springs have a different spring stiffness when deflected clockwise than when deflected counter clockwise. As a consequence the spring stiffness is different during forward stroke than during backward stroke. By using two springs which are wound in opposite senses, the sum of the spring stiffness of both wings is equal in forward as in backward stroke.

Another advantage of using two springs in a parallel configuration is that the total spring stiffness is doubled with the same maximum allowable deflection.

Table 20 shows the relevant characteristics of the latest versions of the wire wound torsional springs that are mounted in the Kulibrie. They are custom made and designed for a specific spring stiffness. The pitch is the spacing between the windings.

	Spring 0,5/4/8 015 pitch	Spring 0,55/4,75/8 015 pitch
E modulus (Mpa)	195000	195000
wire diameter d (mm)	0,5	0,55
spring diameter D (mm)	4	4,75
number of windings	8	8
pitch (mm)	0,15	0,15
height (mm)	5,05	5,45
mass (g)	0,17	1,17
maximal continuous deflection (°)	105	126
k (Nm/rad)	0,0060	0,0073

Table 20 **Spring Characteristics:** Characteristic of two springs with different spring stiffness.

6.5 DESIGN AND PROTOTYPING OF THE FRAME

The frame holds all the components of the driveline and the avionics together and serves as the gearbox for the gears in the robotic hummingbird. Fig. 73 shows the frame of the latest prototype. During the course of this research three different methods have been used to manufacture the frame. All methods use plate-like structures that are interconnected by carbon fiber rods. One method uses plate-like structures cut out of a thin carbon fiber composite plate while the other methods make use of 3D printed plate-like structures, printed with two different 3D-printers and 3D-printing techniques.

6.5.1 3D-PRINTED PARTS USING AN FDM PRINTER

The prototypes that were developed before the start of this PhD. were made of 3D-printed parts from ABS printed by a *Dimension* sst 1200es printer. This printer prints parts using an FDM (Fused Deposion Modeling) technique.

Disadvantages
The resolution of this printer proved to be too low to conveniently set the desired distance between gears of modulus 0.3. Furthermore the parts were brittle and broke easily after crashing.

6.5.2 CARBON COMPOSITE FRAME

To improve the robustness and precision of the frame the idea of printing the plate-like structures of the frame was abandoned in favour of using parts cut out of a carbon fiber reinforced polymer plate with thickness 0.5mm (see Fig. 75). First the shape and the position of the holes were lightly engraved onto the carbon plate, using a laser-cutter. (carbon fiber reinforced polymer cannot be cut by a laser-cutter). After which a handheld multi-tool was used to cut out the parts and to drill the holes.

Advantages
A frame made from plate-like parts cut out of a carbon fiber reinforced polymer plate is strong enough to withstand crashes and can be made thinner than a frame made from 3D-printed parts, making it lighter.

Disadvantages
Drilling and cutting parts out of a carbon fiber reinforced polymer plate by hand is a time consuming technique. Furthermore it proved to be difficult to accurately position the gears. The drilling of the holes (that hold the axes around which the gears turn) had to be done with great care and did not always result in a satisfactory outcome. These problems could be overcome with a CNC mill.
Another practical problem is that the carbon plate is too thin to conveniently ensure that the axes are parallel to each other and perpendicular to the plate-like parts made from carbon. This issue will be further addressed in the next section.

6.5.3 3D PRINTED FRAME USING A POLYJET PRINTER

Since 2015 a new 3D printer is available: an Objet Prime printer from Stratasys. This printer uses a process that jets and cures thin layers of liquid photopolymer with UV energy. This printer is able to make parts with a high resolution of 600dpi that are less brittle than the 3D printed parts using the printer described in section 9.5.1.

Disadvantages
To ensure that the frame is robust enough to withstand crashes, the 3D printed parts need to be sufficiently thick (about 1mm). As a consequence the parts made by this printer are about twice the weight of comparable parts cut out of a carbon fiber reinforced polymer plate. However because the total weight of the frame is only about 10% of the total

weight of the robotic hummingbird, the total weight increase when using 3D-printed parts is about 5%.

Advantages

Printing parts is much less time consuming than cutting them out, because they can be designed using CAD-software and it takes about an hour to print all the parts used in one prototype.

The resolution of the printer is sufficiently high to ensure a proper distance between small gears.

Some 3D-like elements need to be added to the plate-like structures, like for example parts that hold the springs. These elements can be printed together with the plate-like structure as one, increasing the precision of the parts. While with the technique described in section 9.5.2 these elements had to be added manually to the carbon fiber plate structures.

6.6 DESIGN AND PROTOTYPING OF THE GEARS AND SHOULDERS

At this time, the gears cannot be printed with a 3D printer because there is no printer available that can print in materials that meet the requirements concerning wear and friction and has a sufficiently high resolution. Therefor COTS gears have been used. Only a limited amount of small different gears are available which limits the design freedom for the gears.

The shoulders (see Fig. 76) are made from a gear of which a part is cut out and some 3D-printed parts are glued on to hold the springs and the axis for the wing rotation.

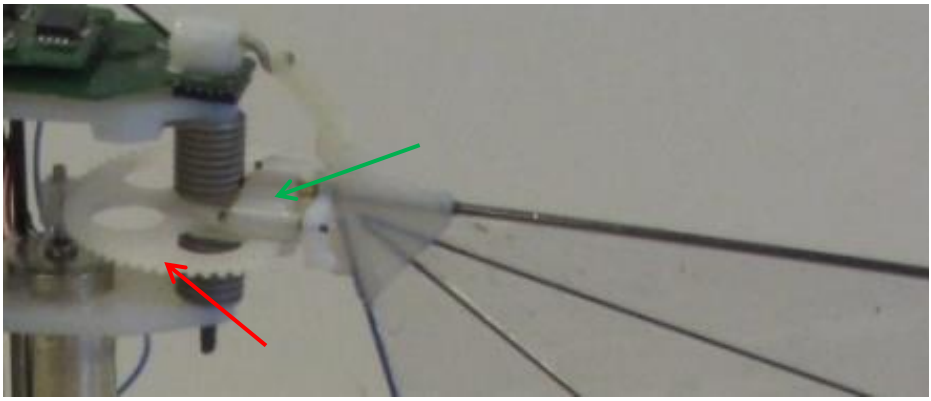

Fig. 76 **The shoulder:** The shoulder is made from a COTS gear (red arrow) to which some 3D-printed parts (green arrow) are glued.

6.7 Design and prototyping of the wings

In the course of this research project over 100 different wings have been made (see Fig. 77). Although they differ in many aspects like: size, materials, structural composition etc., they all consist of three basic parts: a thin **membrane**, stiffened by a **wing frame** made from pultruded carbon fiber rods and the **root** that serves as the connection to the shoulder. In this way they resemble roughly the thin wings of hummingbirds which are stiffened by bones and feathers.

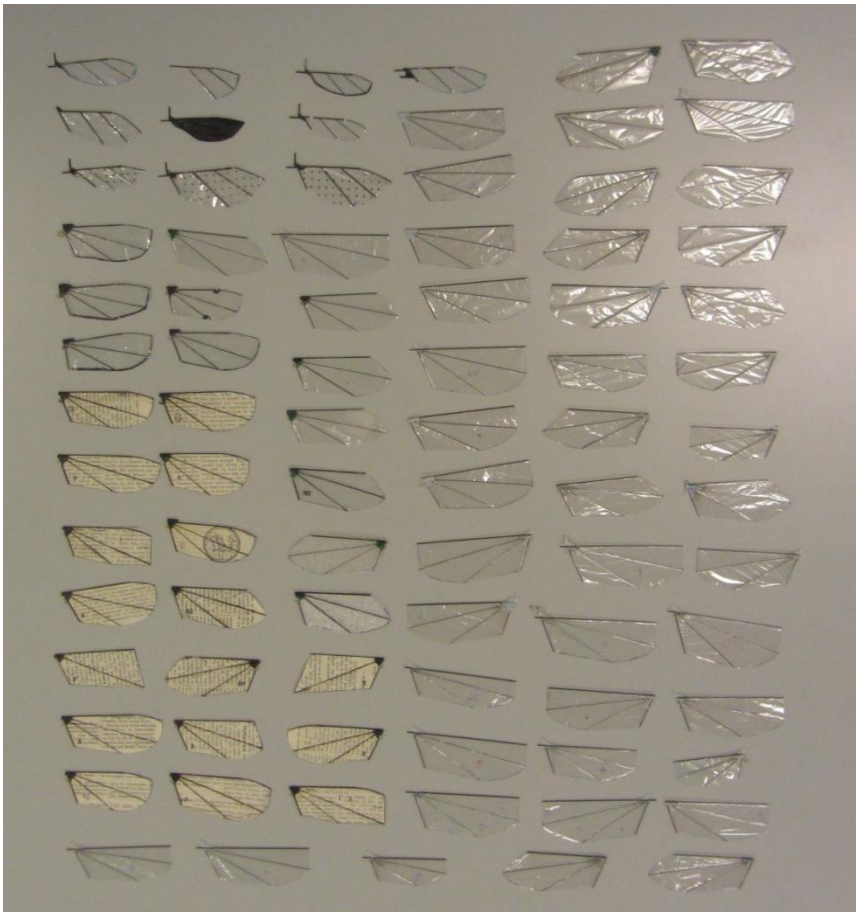

Fig. 77 An overview of all the wings made in the framework of this research (random order)**.** The second wing from the top at the left is the same wing as shown in Fig. 78 and has a length of 50mm.

	Wing 60	Wing 70	Wing 75	Wing 80_S	Wing 80_M	Wing 80_L	Wing 85
wing length (mm)	60	70	75	80			85
average wing chord (mm)	18.8	21.9	23.4	20	25	30	26.6
aspect ratio	3.19	3.19	3.19	**4**	**3.19**	**2.66**	3.19
mass (g)	0.10	0.12	0.13	0.12	0.14	0.17	0.15
Inertia around stroke axis (gmm^2)	68	115	146	182	187	192	225

Table 21 characteristics of the wings used in the experiments described in section 3.4.2 of chapter 3

Building wings is a time-consuming activity. Although the time to make a wing is significantly reduced from about 2 hours in 2012 to about 30 minutes currently, the time it takes to make a wing still limits comprehensive experimental research concerning the many parameters that govern the wing shape, stiffness and robustness.
Nevertheless, three aspects of the wing are important and have been improved during time:

The performance of the wing
The performance of the wing is defined by the thrust one can generate and the power that is required to generate this thrust. The performance of the wing is improved by using the experimental approach described in section 6.4.1.

The robustness of the wing
An important aspect of the wing of a robotic hummingbird is its robustness. A wing should withstand the impact of it flapping against an object and withstand the impact of a crash to some degree. The robustness of the wings is improved step by step by trial and error to an extent that currently they are robust enough to withstand the vast majority of crashes and only seldom a wing breaks.

The repeatability of the manufacturing process of the wings,
The repeatability of the manufacturing process of the wings determines to which extent two wings that are made to be equal are indeed equal. The repeatability of the wing is improved by using better production methods, to an extent that it is no matter of concern anymore.

The following sections describe how the wings were made at the start of this research and which changes to the wing design and production process have been implemented to improve the performance, the robustness and the repeatability of the production process

of the artificial hummingbird wings. Fig. 78 shows the first and the last wing made during this PhD.

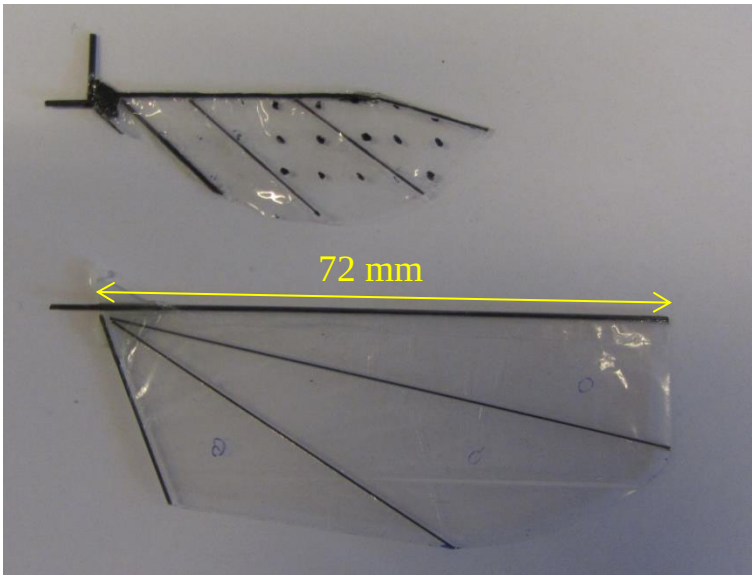

Fig. 78 The first and the last wing: The upper wing is the first one that was made in the frame work of this research and the lower wing is the last one made. The ribs are made from carbon fiber composite rods and the membrane is made from Mylar foil. The lower wing measures 72mm between wing tip and the point where the ribs intersect. However the wing length of this wing is 80mm defined as the distance between wing tip and stroke axis.

6.7.1 THE WING ROOT

The first wings had a wing root that was a manually assembly of 3 small parts made by hand. Fig. 79 shows an example of such a wing root, with its parts. Although this production method results in the lightest wing roots, making one is time consuming and it is a process that is difficult to repeat in order to obtain similar wing roots. With the advent of the 3D-printer described in section 6.5.3, it became possible to print the wing roots. This had two major advantages: it solves the repeatability issue and saves a considerable amount of time. Fig. 78 shows a wing with a 3D-printed wing root in. 3D-printed wing roots are heavier but because they are relatively close to the stroke axis, their moment of inertia is relative small in comparison with the total moment of inertia of the wing.

6.7.2 THE WING FRAME

The wing frame consists of a leading edge and usually two extra veins which are all carbon fiber rods or tubes cut to the desired lengths. Besides, the overall size of the wing, which is determined by the weight that has to be lifted and the flapping mechanism, four aspects of the wing frame have been tested using the experimental method described in section 6.4.1:

The thickness of the leading edge and the veins

Off-the-shelf carbon rods and tubes exist in a limited amount of thicknesses. For the veins we tested carbon rods with thicknesses of 0.3 and 0.5 mm. For the leading edge we tested carbon rods of 0.7 and 0.5mm and a carbon tube with an outer diameter of 0.7 mm and inner diameter of 0.3mm.

The thickness of both the leading edge and the veins has an influence on the stiffness of the wing and the moment of inertia of the wing around the stroke axis. To obtain a wing that is sufficiently stiff, such that its deformation due to the wing motion does not reduces the stroke amplitude or twists too much, the carbon rods needs to be sufficiently thick. However thicker carbon rods also considerably increase the moment of inertia. A trade-off exists between wing stiffness and wing inertia. The optimal thickness of the leading edge and the veins depends on the size of the wing, the stiffness of the wing membrane and the wing motion. As a consequence, an experimental trial and error method remains necessary to optimize the thickness of the leading edge and the veins.

Early wings had a leading edge that was made of a combination of a tube at the root of the wing and a rod of 0.3mm at the wing tip. This rod was fitted in the tube. This results in a leading edge that is sufficiently stiff, but has a considerable lower moment of inertia around the stroke axis. As a consequence wings with this type of leading edge have a better performance than wings with a leading edge made of the tube. This type of wings however brakes easily at the intersection between the tube and the rod when colliding with an obstacle. Therefore we abandoned this design for the leading edge in favour of a more robust leading edge made from one rod or tube.

For relative large wings with wing length of 80mm we found that in general veins with the smallest available thickness of 0.3mm are sufficiently stiff and a for the leading edge, the tube performs better than the rods. For relative small wings of length 50mm a rod of 0.5mm performs better than the tube for the leading edge.

The amount of veins

All wings have two veins, with the exception of one wing design. This wing has only one vain (see Fig. 77) and performed worse than a comparable wing with two veins. More research is necessary to better understand the influence of the amount of veins.

The orientation of the veins

Two different types of wings were made concerning the orientation of the veins. Originally the veins were glued onto the leading edge (upper wing in Fig. 78). However tests showed that wings with veins that radiated outwards from the wing root (lower wing in Fig. 78) perform better and are more robust.

6.7.3 THE WING MEMBRANE

The most important criteria for the membrane are its areal density and its resistance to plastic deformation and tear. Two materials are tested in several thicknesses:

- polyethylene terephthalate which is sold under the brand name Mylar
- lightweight offset paper, taken from a bible, is thinner, lighter and more resistant to tear compared to other types of paper (Fig. 79).

A Mylar foil proved to be a better option than lightweight offset paper. Although it is more difficult to glue Mylar to carbon fibre rods; it is selected because it is lighter and better resistant to tear.

Three thicknesses of Mylar foil are tested: 5, 10 and 20 micron. The 10µm version is selected for the latest wings. However more research should be done to have a better understanding of the influence of the Mylar foil thickness on the thrust generated by the wing and the power needed to generate the wing motion.

Fig. 79 Wing made from light weight offset paper

6.8 ESTABLISHING STABLE FLIGHT

To obtain stable flight of a robotic hummingbird many aspects have to be considered and implemented correctly: Among other aspects:

- the flapping mechanism of the robotic hummingbird needs to be able to adequately and reliably perform asymmetric wing motions such that independent roll, pitch and yaw torques can be generated
- a control system has to be implemented with sensors that adequately measure the attitude at a rate sufficiently fast
- the actuators need to be able to react fast enough to counteract undesirable motions
- the control algorithm needs to be implemented correctly.

If one of these aspects is not properly implemented, stable flight cannot be achieved. If stable flight is not achieved, it can be difficult to pin point the cause of this failure. One way to overcome this problem is by a step-by step approach such that all aspects can be evaluated independently.

This section describes the step-by-step trial and error approach that consists of a series of 'flight tests' which was followed to obtain stable flight of the Kulibrie. Because no means of generating a yaw torque has been implemented, only pitch and roll motions are stabilized, which is sufficient to stay aloft. Table 17 gives a chronological overview of all the milestones that have been reached so far to obtain stable flight.

6.8.1 HOVERING FLIGHT ASSISTED BY GUIDES

A first series of flight tests is performed to evaluate if the flapping mechanism is able to generate a sufficient amount of thrust to lift the robotic hummingbird. A setup is made that allowed the Kulibrie to fly up and down guided by two nylon cables (see Fig. 80).

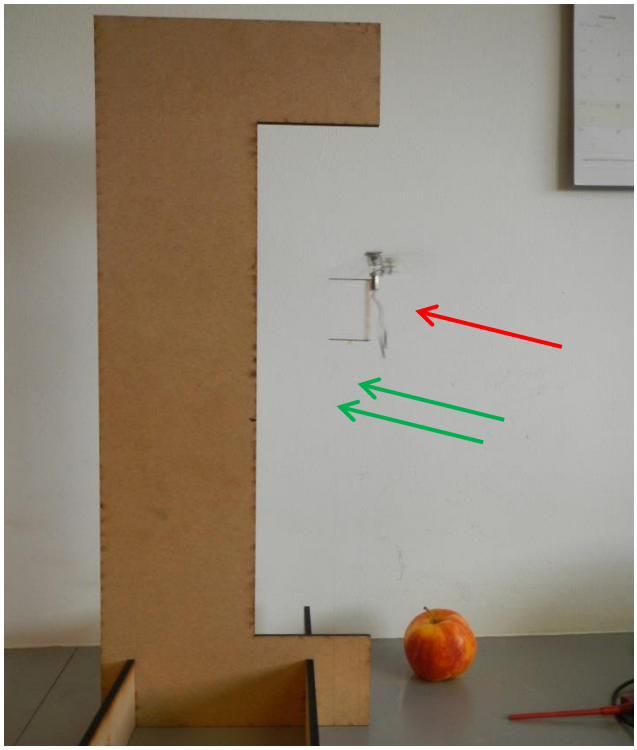

Fig. 80 **Experimental validation of thrust:** A prototype of the Kulibrie (indicated by a red arrow) is able to fly up and down and is guided by two nylon wires. The nylon wires are too thin to be viewed in the image. They are indicated by green arrows.

This test proved that the resonant flapping mechanism is indeed able to lift the weight of the robotic hummingbird. Furthermore it showed that no undesired variations in average thrust occur during flight and that the thrust can be varied by a pilot such that the altitude of the robotic hummingbird can be controlled manually.

6.8.2 PASSIVELY STABILIZED FREE FLIGHT

The next step was to obtain free flight, without the need of guides. The first approach that resulted in free flight was inspired by the research of Van Breugel [Van Breugel et al, 2009] and made use of aerodynamic dampers (tails) that passively stabilize flight (see Fig. 81).

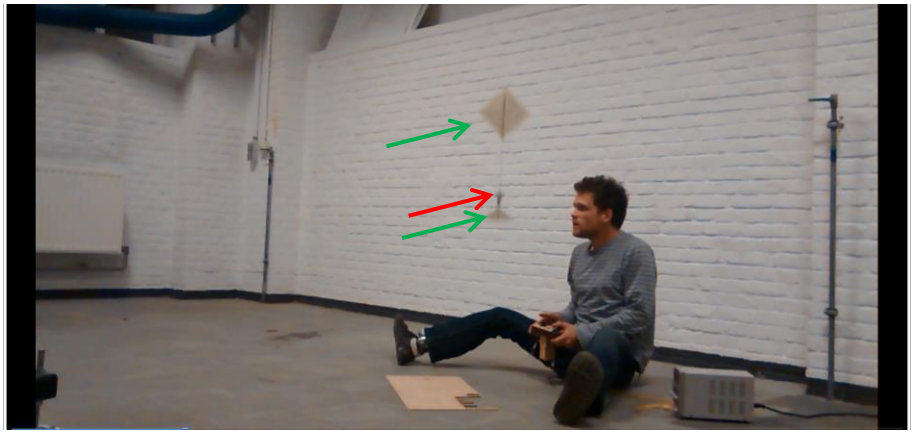

Fig. 81 **Experimental validation of passively stabilized flight of the Kulibrie.** The flight is stabilized passively by using aerodynamic dampers. The aerodynamic dampers are indicated by the green arrows and the body of the Kulibrie is indicated by the red arrow.

These flight tests showed that also without guiding cables, no undesired variations in average thrust occur during flight and that the thrust can be varied by a pilot such that the altitude of the robotic hummingbird can be controlled manually.

6.8.3 EVALUATING ROLL AND PITCH TORQUE

In a next step the pitch and roll torques that can be generated by asymmetric wing motions are evaluated. This is done by attaching the robotic hummingbird to a tests setup (see Fig. 82) that only allowed roll and pitch motions. Roll and pitch manoeuvres are controlled manually.

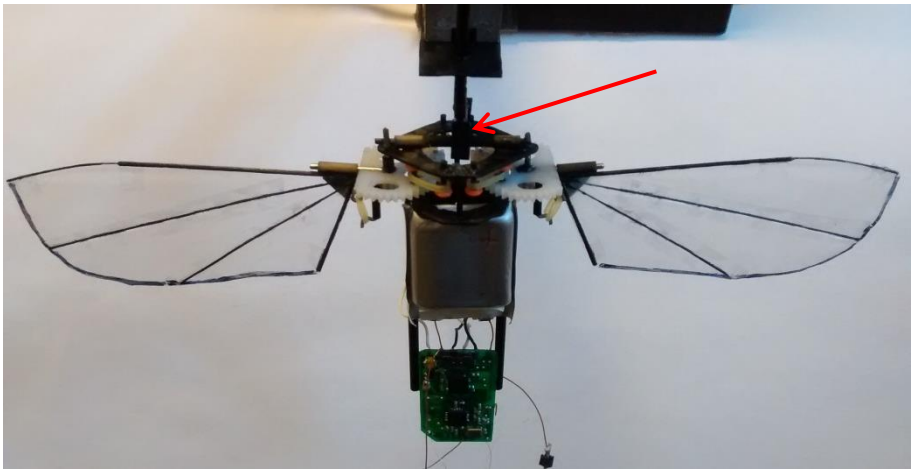

Fig. 82 **Experimental validation of the Roll and pitch torques.** A prototype of the Kulibrie is fixed by means of a gimbal joint (indicated by the red arrow). The gimbal joint allows the Kulibrie to perform roll and pitch motions simultaneously.

These tests showed that the roll and pitch torques are large enough to tilt the robotic hummingbird significantly. Furthermore they showed that no undesired variations in roll or pitch angle occurred during flapping. Another important conclusion that could be drawn from these experiments is that roll and pitch torques can be generated independently.

6.8.4 ACTIVELY STABILIZED FREE FLIGHT IN ONE PLANE

In a next series of experiments the active control of pitch and roll were first evaluated separately. To do this a setup is made that consists of two large parallel plates made from transparent Plexiglas (see Fig. 83). The distance between the plates can be adjusted with bolts and nuts. A cubic flight frame is attached to the robotic hummingbird that is slightly smaller than the space between the plates and large enough to envelop the wing during flight. This flight frame ensures that the wings do not collide with the Plexiglas plates and ensures that the robotic hummingbird can only describe a planar motion. By rotating the robotic hummingbird (and flight frame) 90 degrees it is possible to test either roll or pitch control.

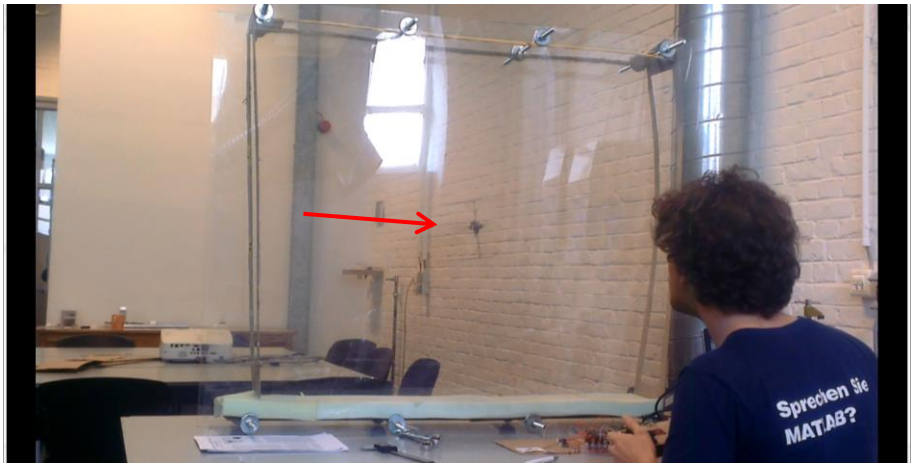

Fig. 83 **Separately evaluating the active roll and pitch stabilization of the Kulibrie.** The Kulibrie (indicated by a red arrow) flies between two transparent plates and is surrounded by a protective frame. The protective frame prohibits the wings from colliding with the plates and ensures that only a planar motion between the plates is possible.

Evaluating pitch and roll stability separately allows to study both motions separately, which is necessary to set the control parameters. Both the roll and the pitch motion could be stabilized actively. These tests showed that the control algorithm worked and that the speed of the control loop is sufficiently high. However between stable periods of a couple of seconds, the flight motion got disturbed. A possible explanation is that the flight frame collides with the plates during flight.

6.8.5 ACTIVELY STABILIZED 3D FREE FLIGHT

The final step in the step-by-step trial and error approach is testing the actively stabilised free flight. The first successfully stabilised free flight was obtained in May 2015. This flight lasted about 10 seconds before the Kulibrie started to wobble and crash. At that time the stability of the flight was unpredictable. Sometimes the flight was stable enough to stay aloft for a couple of seconds, other days no successful take-off was possible. Furthermore almost always something broke when the robotic hummingbird crashed.

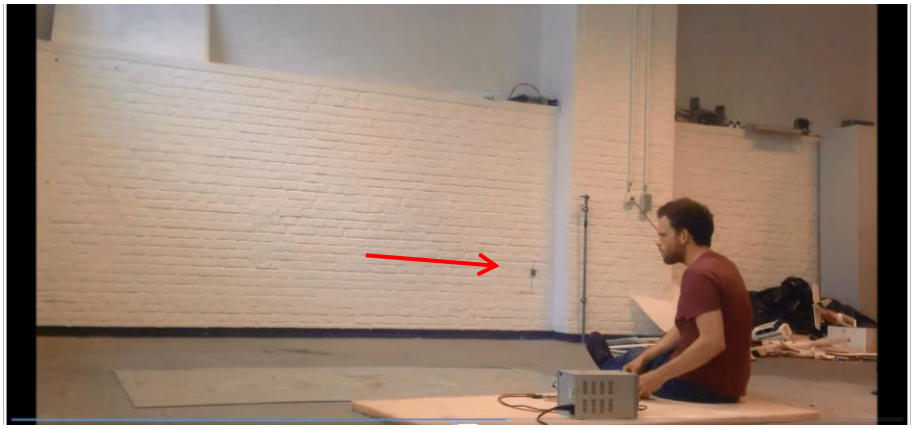

Fig. 84 First actively stabilized free flight of the Kulibrie. The Kulibrie (indicated by the red arrow) flew stable for about 10 seconds.

These tests pointed out the importance of increasing the robustness of the robotic hummingbird such that it would not break as easily when crashing. After improving the design as described in sections 6.5 to 6.17. The prototype is robust enough. The latest prototypes have crashed over a hundred times without the need of repairements. Some crashes involved a fall from over 4 meters.

Improvements to the control algorithm and the production process have resulted in a predictable flight about 60seconds. However the flight is still wobbly.

6.9 CONCLUSIONS

Two different flapping mechanisms have been implemented in the Kulibrie: the stroke-cam mechanism (2011-2013) and the resonant flapping mechanism (2014-present). The resonant flapping mechanism is driven by a brushed coreless DC motor of which the speed is reduced by a simple gearbox that consists of two gears. Further research is required to optimise the gear ratio. Custom made wire wound torsional springs of stainless steel are used as elastic elements. Two helical springs which are wound in opposite senses are implemented to double the spring stiffness without decreasing the maximum deflection and to keep the system stiffness constant during forward and backward stroke.

The Kulibrie has a wingspan of 186mm and weights 14.1g. The wing motion is characterized by a flapping frequency of 25Hz and a stroke amplitude up to 180°.

To achieve stable flight a series of flight tests is performed that systematically increased the flight complexity. Currently this approach results in a stable flight of about a minute but the flight is still wobbly, which complicates the flight control.

7 CONCLUSION

7.1 OVERVIEW

A robotic hummingbird is developed with a wingspan of 186mm and a weight of 14.1g (Fig. 85). It is able to perform stable flight. The longest flight recorded so far lasted 55 seconds. Its hummingbird-like wing motion is characterized by a flapping frequency of 25Hz and a stroke amplitude up to 180°. The wings are driven by a resonant flapping mechanism.

With a stroke amplitude of 160°, a flapping frequency of 25Hz, and an angle of attack of 50°, an 80mm long wing generates 7.1cN thrust. To generate this amount of thrust the resonant flapping mechanism consumes 0.87W of power, which results in a performance of 8.38cN/W. This is 40% more than the performance of the Nano Hummingbird (5.8cN/W), which is considered as the state of art of robotic hummingbirds.

The resonant flapping mechanism can generate roll and pitch torques merely by adjusting the current through the motor and without the need of extra actuators or other mechanical components that would increase the weight and the complexity of the mechanism. An independent roll torque is generated by increasing the stroke amplitude of one wing while decreasing the stroke amplitude of the other wing. This requires that each wing is driven by a separate resonant mechanism. An independent pitch torque is generated by modifying the average stroke amplitude of both wings symmetrically.

In order to actively control flight, an on-board flight controller is developed and implemented that consists of a microprocessor, a motor driver, a wireless transceiver, two magnetic encoders to measure the stroke amplitude and mean stroke angle of each wing and several MEMS motion sensors that measure the angular velocity.

A feedback control algorithm is programmed on the microcontroller. This algorithm, which comprises several PID algorithms, controls the attitude and the altitude of the Kulibrie by adjusting the wing motion based on the data from the motion sensors, encoders and manual input from the pilot.

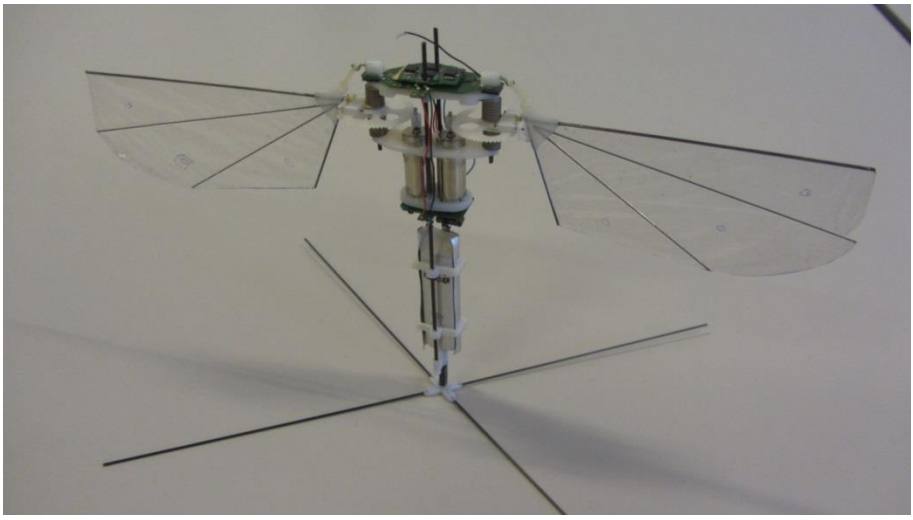

Fig. 85: **The Kulibrie**

7.2 FUTURE RESEARCH

Some improvements to the robotic hummingbird developed in the framework of this research are necessary to make it a fully controlled free flying robotic hummingbird.

Active control of wing rotation to enable yaw manoeuvres

A big disadvantage of the resonant flapping mechanism as used in the latest prototypes of the Kulibrie is that it does not control the wing rotation actively. As a consequence the Kulibrie cannot perform adequate yaw manoeuvres. The implementation of an actively controlled wing rotation would not only allow the generation of yaw torques but would offer an additional method of generating roll and pitch torques, effectively increasing the flight envelope.

With an actively controlled wing rotation, there is no need any more of two separate motors, because roll torques could be generated by adjusting the angle of attack. As a consequence, the weight of the Kulibrie could be decreases and the performance increased by replacing the two motors by one slightly bigger motor.
We assume that active wing rotation could increase the flight stability and control.

Improving the flight control and stability of the Kulibrie
Additional research is necessary to increase the flight stability and control. The nature of the currently wobbly flight is not fully understood. Possible improvements can be made on the control of the wing motion, the choice of the motion sensors and the control algorithm.

Developing a numerical model of the stroke-cam flapping mechanism
At this moment the motors have to be tested to know if they are powerful enough to generate the appropriate wing motion with a wing of a certain wing length. A numerical model could be useful to predict the required motor specifications (and allow to design a custom motor) instead of having to test many of them.
A numerical model could also be used to better understand the influence that the stiffness of a wing has on its performance.

Far future
The long term goal of this research is to reduce the size of the Kulibrie in order to better utilize the advantages of flapping wing propulsion. In order to facilitate the minimization of the Kulibrie other types flapping mechanisms should be studied that do not use the small coreless dc-motors that are currently used. These motors are difficult to downscale to the size that would be implemented in a robotic insect with a wingspan of just a few centimetres.

8 REFERENCES

[Altshuler et al, 2009]
Altshuler, D. L., Princevac, M., Pan, H., & Lozano, J. (2009). Wake patterns of the wings and tail of hovering hummingbirds. Experiments in fluids, 46(5), 835-846.

[Altartouri et al, 2017]
H. Altartouri, A. Roshanbin, A. Preumont: Robotic Hummingbird of ULB URL: https://www.youtube.com/watch?v=aWeUPiz2pt4 [cited 11/03/2017].

[Altshuler et al, 2010]
H Altshuler, D. L., Dudley, R., Heredia, S. M., & McGuire, J. A.(2010). Allometry of hummingbird lifting performance. Journal of Experimental Biology, 213(5), 725-734.

[Altshuler et al, 2012]
Altshuler, D. L., Quicazán-Rubio, E. M., Segre, P. S., & Middleton, K. M. (2012). Wingbeat kinematics and motor control of yaw turns in Anna's hummingbirds (Calypte anna). Journal of experimental biology, 215(23), 4070-4084.

[Anderson & John 2010]
Anderson Jr, John David. Fundamentals of aerodynamics. Tata McGraw-Hill Education, 2010.

[Aono et al, 2008]
Aono, H., Liang, F., & Liu, H. (2008). Near-and far-field aerodynamics in insect hovering flight: an integrated computational study. Journal of Experimental Biology, 211(2), 239-257.

[Benedict & Coleman, 1997]
Benedict, M., Coleman, D., "Experiments on rigid wing undergoing hover-capable flapping kinematics at micro-air-vehicle-scale Reynolds numbers," AIAA Journal, Vol. 54, No.4, 2016, pp. 1145-1157. Doi: 10.2514/1.J052947

[Berg & Biewener, 2008]
Berg, A. M., & Biewener, A. A. (2008). Kinematics and power requirements of ascending and descending flight in the pigeon (Columba livia). Journal of Experimental Biology, 211(7), 1120-1130.

[Berman & Wang, 2007]
Berman, G. J., & Wang, Z. J. (2007). Energy-minimizing kinematics in hovering insect flight. Journal of Fluid Mechanics, 582, 153-168.

[Beun & Jans, 2014]

Visualisatie van 3D-stromingen rond een flappende vleugel op basis van 2D-PIV metingen , masterthesis, 2014, KULeuven

[Birch et al, 2004]
Birch, J.M., Dickson, W.B., and Dickinson, M.H., "Force production and flow structure of the leading edge vortex on flapping wings at high and low reynolds numbers,". J. Exp. Biol.,Vol. 207, 2004, pp. 1063-1072

[Black Hornet, 2017]
picture of a small military surveillance drone, URL:https://upload.wikimedia.org/wikipedia/commons/thumb/e/ed/Black_Hornet_Nano_Helicopter_UAV.jpg/1920px-Black_Hornet_Nano_Helicopter_UAV.jpg, , [cited 11/03/2017].

[Boniecki, 2017]
Tad Boniecki, Image of Collared Inca hummingbird, URL: https://www.beautyofbirds.com/collaredincahummingbirds.html, [cited 11/03/2017].

[Campolo et al, 2014]
Campolo, D., Azhar, M., Lau, G. K., & Sitti, M. (2014). Can DC motors directly drive flapping wings at high frequency and large wing strokes?. IEEE/ASME Transactions on Mechatronics, 19(1), 109-120.

[Campolo, 2010]
Campolo, D. (2010). Motor selection via impedance-matching for driving nonlinearly damped, resonant loads. Mechatronics, 20(5), 566-573.

[Chai & Millard, 1997]
Chai, P., & Millard, D. (1997). Flight and size constraints: hovering performance of large hummingbirds under maximal loading. Journal of Experimental Biology, 200(21), 2757-2763.

[Chirarattananon et al, 2014]
Chirarattananon, P., Ma, K. Y., & Wood, R. J. (2014). Adaptive control of a millimeter-scale flapping-wing robot. Bioinspiration & biomimetics, 9(2), 025004.

[Coleman et al, 2015]
Coleman, D., Benedict, M., Hrishikeshavan, V., & Chopra, I. (2015, May). Design, Development and Flight-Testing of a Robotic Hummingbird. In AHS 71st Annual Forum, Virginia Beach, Virginia, edited by AH Society.

[Darpa, 2017]
DARPA, URL: https://en.wikipedia.org/wiki/DARPA, [cited 11/03/2017].

[Delfly, 2017]
The Delfly, URL: www.DelFly.nl, [cited 11/03/2017].

[Deng et al, 2016]
Deng, S., Percin, M., van Oudheusden, B., "Experimental investigation of aerodynamics of flapping-wing micro-air-vehicle by force and flow-field measurements," AIAA Journal, Vol. 54, No.2, 2016, pp. 588-602.

[Dickinson, 1999]
Dickinson, M. H. "Wing Rotation and the Aerodynamic Basis of Insect Flight," Science, Vol. 284 (5422), 1999, pp. 1954–60. doi:10.1126/science.284.5422.1954.

[Driver, 2017]
E. Driver, http://www.nature.com/news/hummingbird-flight-has-a-clever-twist-1.9639 [cited 11/03/2017].

[Ellington, 1984]
Ellington, C. P. (1984). The aerodynamics of insect flight. II. Morphological parameters. Phil. Trans. R. Soc. Lond. B, 305, 17-40.

[Ellington, 1997]
Ellington, C. P. "The three-dimensional leading-edge vortex of a 'Hovering' Model Hawkmoth," Philos. Trans. R. Soc. B Biol. Sci., Vol. 352, 1997, pp. 329-340.

[Ellington, 1999]
Ellington, C. P. (1999). The novel aerodynamics of insect flight: applications to micro-air vehicles. Journal of Experimental Biology, 202(23), 3439-3448.

[Fry et al, 2003]
Fry, S. N., Sayaman, R., & Dickinson, M. H. (2003). The aerodynamics of free-flight maneuvers in Drosophila. Science, 300(5618), 495-498.

[Fuller et al, 2015]
Fuller, S. B., Whitney, J. P., & Wood, R. J. (2015, September). Rotating the heading angle of underactuated flapping-wing flyers by wriggle-steering. In Intelligent Robots and Systems (IROS), 2015 IEEE/RSJ International Conference on (pp. 1292-1299). IEEE.

[Genera, 2017]
List of hummingbird genera, URL: https://en.wikipedia.org/wiki/List_of_hummingbird genera [cited 11/03/2017].

[Goetze, 2017]

J. Goetze; propeller thrust tests, URL: https://community.micro-motor-warehouse.com/t/thrust-tests/1492, [cited 11/03/2017].

[Greenewalt, 1960]
Greenewalt, C. H. (1960). Hummingbirds. Courier Corporation.

[Hedrick et al, 2009]
Hedrick, T. L., Cheng, B., & Deng, X. (2009). Wingbeat time and the scaling of passive rotational damping in flapping flight. Science, 324(5924), 252-255.

[Hengstenberg et al, 1986]
Hengstenberg, R., Sandeman, D. C., & Hengstenberg, B. (1986). Compensatory head roll in the blowfly Calliphora during flight. Proceedings of the Royal Society of London B: Biological Sciences, 227(1249), 455-482.

[Ho et al, 2003]
Ho, S., Nassef, H., Pornsinsirirak, N., Tai, Y.-C., and Ho., C.-M., 'Unsteady aerodynamics and flow control for flapping wing flyers," Progress in Aerospace Sciences, Vol. 39, 2003, pp. 635–681.

[Jongerius & Lentink, 2010]
Jongerius, S. R., & Lentink, D. (2010). Structural analysis of a dragonfly wing. Experimental Mechanics, 50(9), 1323-1334.

[Karasek & Preumont, 2014]
Karasek, M., & Preumont, A. (2014). Robotic hummingbird: Design of a control mechanism for a hovering flapping wing micro air vehicle (Doctoral dissertation, Doctoral thesis, Universite Libre de Bruxelles).

[Keennon et al, 2012]
Keennon, M., Klingebiel, K., & Won, H. (2012, January). Development of the nano hummingbird: A tailless flapping wing micro air vehicle. In 50th AIAA Aerospace Sciences Meeting including the New Horizons Forum and Aerospace Exposition (p. 588).

[Kii, 2017]
Picture of a toy quadcopter, URL: http://bestdroneswithcameras.com/drones/kii-toys-nano-drone , [cited 11/03/2017].

[Kruyt et al, 2014]
Kruyt, J. W., Quicazán-Rubio, E. M., van Heijst, G. F., Altshuler, D. L., & Lentink, D. (2014). Hummingbird wing efficacy depends on aspect ratio and compares with helicopter rotors. Journal of The Royal Society Interface, 11(99), 20140585.

[Lentink & Dickinson, 2009]
Lentink, D., & Dickinson, M. H. (2009). Rotational accelerations stabilize leading edge vortices on revolving fly wings. Journal of Experimental Biology, 212(16), 2705-2719.

[Leys et al, 2015]
Leys, F., Vandepitte, D., & Reynaerts, D. (2015, December). Design of a flapping wing micro air vehicle, based on the Rufous Hummingbird. In Robotics and Biomimetics (ROBIO), 2015 IEEE International Conference on (pp. 1266-1271). IEEE.

[Leys, 2011]
Ontwikkeling van een microvliegtuig met flappende vleugels gebasseerd op de Rosse kolibrie, masterthesis 2011, KULeuven

[Leys, nov 2015]
The flight of the Kulibrie, URL: https://www.youtube.com/watch?v=CExDZieQFXk, [cited 11/03/2017].

[Liu & Aono, 2009]
Liu, H., & Aono, H. (2009). Size effects on insect hovering aerodynamics: an integrated computational study. Bioinspiration & Biomimetics, 4(1), 015002.

[Liu et al, 1998]
Liu, H., Ellington, C. P., Kawachi, K., Van Den Berg, C., & Willmott, A. P. (1998). A computational fluid dynamic study of hawkmoth hovering. Journal of Experimental Biology, 201(4), 461-477.

[Lok et al, 2015]
Lok, M., Zhang, X., Helbling, E. F., Wood, R., Brooks, D., & Wei, G. Y. (2015, September). A power electronics unit to drive piezoelectric actuators for flying microrobots. In Custom Integrated Circuits Conference (CICC), 2015 IEEE (pp. 1-4). IEEE.

[Ma Kevin et al, 2013]
Ma, Kevin Y., et al. "Controlled flight of a biologically inspired, insect-scale robot." Science 340.6132 (2013): 603-607.

[MathWorks, 2017]
R2014a, The MathWorks Inc., Natick, MA, 2000).

[Meert & Note, 2013]
Bewegings-en stromingsanalyse van de vleugel van de Kulibrie, masterthesis, 2013, KULeuven

[Melling, 1997]
Melling, A., "Tracer particles and seeding for particle image velocimetry," Meas. Sci. Technol., Vol. 8, No12, 1997, pp.1406.

[Microbat, 2017]
The Micro Bat, URL: http://touch.caltech.edu/research/bat/bat.htm [cited 11/03/2017].

[Orlowski, 2011]
Orlowski, C. T. (2011). Flapping Wing Micro Air Vehicles: An Analysis of the Importance of the Mass of the Wings to Flight Dynamics, Stability, and Control (Doctoral dissertation, The University of Michigan).

[Phan & Park, 2015]
Phan, H. V., & Park, H. C. (2015, October). Remotely controlled flight of an insect-like tailless Flapping-wing Micro Air Vehicle. In Ubiquitous Robots and Ambient Intelligence (URAI), 2015 12th International Conference on (pp. 315-317). IEEE.

[Phantom, 2017]
picture of a camera drone, URL: http://www.rc-quadrocopter.de/wp-content/uploads/dji-phantom-3-17.jpg , [cited 11/03/2017].

[Phillips & Knowles, 2011]
Phillips, N., & Knowles, K. (2011). Effect of flapping kinematics on the mean lift of an insect-like flapping wing. Proceedings of the Institution of Mechanical Engineers, Part G: Journal of Aerospace Engineering, 225(7), 723-736.

[Pornsin-Sirirak et al, 2001]
Pornsin-Sirirak, T. N., Tai, Y. C., Ho, C. M., & Keennon, M. (2001, August). Microbat: A palm-sized electrically powered ornithopter. In Proceedings of NASA/JPL Workshop on Biomorphic Robotics (pp. 14-17).

[Predator, 2017]
image of a military drone, URL: https://upload.wikimedia.org/wikipedia/commons/0/08/MQ-1_Predator_unmanned_aircraft.jpg, [cited 11/03/2017].

[Ristroph & Childres, 2014]
Ristroph, L., & Childress, S. (2014). Stable hovering of a jellyfish-like flying machine. Journal of The Royal Society Interface, 11(92), 20130992.

[Ristroph et al, 2010]

Ristroph, L., Bergou, A. J., Ristroph, G., Coumes, K., Berman, G. J., Guckenheimer, J., ... & Cohen, I. (2010). Discovering the flight autostabilizer of fruit flies by inducing aerial stumbles. Proceedings of the National Academy of Sciences, 107(11), 4820-4824.

[Ristroph et al, 2013]
Ristroph, L., Ristroph, G., Morozova, S., Bergou, A. J., Chang, S., Guckenheimer, J. & Cohen, I. (2013). Active and passive stabilization of body pitch in insect flight. Journal of The Royal Society Interface, 10(85), 20130237.

[Robobee, 2017]
The Robobee, URL: https://wyss.harvard.edu/technology/autonomous-flying-microrobots-robobees/ [cited 11/03/2017].

[Rowling, 1997]
J.K. Rowling, The Philosopher's Stone. Bloomsburry Publishing, 1997

[Sane & Dickinson, 2002]
Sane, S. P., & Dickinson, M. H. (2002). The aerodynamic effects of wing rotation and a revised quasi-steady model of flapping flight. Journal of experimental biology, 205(8), 1087-1096.

[Sane, 2003]
Sane, S. P., "Review the aerodynamics of insect flight," The Journal of Experimental Biology, Vol. 206, 2003, pp. 4191-4208.

[Sapir & Dudley, 2012]
Sapir, N., & Dudley, R. (2012). Backward flight in hummingbirds employs unique kinematic adjustments and entails low metabolic cost. Journal of Experimental Biology, 215(20), 3603-3611.

[Schenato, 2003]
Schenato, L. (2003). Analysis and Control of Flapping Flight: from Biological to Robotic Insects1 (Doctoral dissertation, University of California at Berkeley).

[Sedov, 1965]
Sedov, L. I. (1965). Two-Dimensional Problems in Hydrodynamics and Aerodynamics (ed. C. Chu, H. Cohen and B. Seckler), pp. 20-30. New York: Interscience Publishers.

[Shyy et al, 2007]
Shyy, W., Lian, Y., Tang, J., Viieru, D., & Liu, H. (2007). Aerodynamics of low Reynolds number flyers (Vol. 22). Cambridge University Press.

[Shyy et al, 2008]
W. Shyy, Y. Lian, J. Tang, H. Liu, P. Trizila, B. Stanford, L. Bernal, C. Cesnik,P. Friedmann, and P. Ifju. Computational aerodynamics of low reynolds number plunging, pitching and flexible wings for mav applications. In 46th AIAA Aerospace Sciences Meeting and Exhibit, 2008.

[Shyy et al, 2010]
W. Shyy, H. Aono, S.K. Chimakurthi, P. Trizila, C.-K. Kang, C.E.S. Cesnik, and H. Liu. Recent progress in flapping wing aerodynamics and aeroelasticity. Progress in Aerospace Sciences, 46:284–327, February 2010.

[Smartbird, 2017]
The Festo Smartbird https://www.festo.com/group/en/cms/10238.htm [cited 11/03/2017].

[Smartbird, 2017]
Image of the Festo Smartbird, URL: http://www.festo.com/cms/en_corp/11369.htm, [cited 11/03/2017].

[Snitch, 2017]
Image of the Snitch of Harry potter, URL: http://harrypotter.wikia.com/wiki/File:Snitch_2.jpg, [cited 11/03/2017].

[Stiles et al, 2005]
Stiles, F. G., Altshuler, D. L., & Dudley, R. (2005). Wing morphology and flight behavior of some North American hummingbird species. The Auk, 122(3), 872-886.

[Tanaka & Wood, 2010]
Tanaka, H., & Wood, R. J. (2010). Fabrication of corrugated artificial insect wings using laser micromachined molds. Journal of Micromechanics and Microengineering, 20(7), 075008.

[Timmermans, 2016]
Quasi statisch model voor de identificatie van krachten en momenten op nano vliegtuig met flapperende vleugels, masterthesis 2016, KULeuven

[T-motor, 2017]
T-motor, URL: http://www.rctigermotor.com/, [cited 11/03/2017].

[Tobalske et al, 2007]
Tobalske, B. W., Warrick, D. R., Clark, C. J., Powers, D. R., Hedrick, T. L., Hyder, G. A., & Biewener, A. A. (2007). Three-dimensional kinematics of hummingbird flight. Journal of Experimental Biology, 210(13), 2368-2382.

[Ulrich et al, 2010]
Ulrich, E. R., Pines, D. J., & Humbert, J. S. (2010). From falling to flying: the path to powered flight of a robotic samara nano air vehicle. Bioinspiration & biomimetics, 5(4), 045009.

[Vanierschot & Van den Bulck, 2010]
Maarten Vanierschot and Eric Van den Bulck. Experimental study of low precessing frequencies in the wake of a turbulent annular jet. 2010.

[Wakeling & Ellington, 1997]
Wakeling, J., Ellington, C., "Dragonfly flight 2. velocities, accelerations and kinematics of flapping flight," The Journal of Experimental Biology, Vol. 200, 1997, pp.557–582.

[Warrick et al, 2005]
Warrick, D. R., Tobalske, B. W., & Powers, D. R. (2005). Aerodynamics of the hovering hummingbird. Nature, 435(7045), 1094-1097.

[Wasp, 2017]
picture of the smallest flying animal, URL: http://blogs.bu.edu/biolocomotion/2011/10/12/the-worlds-smallest-flying-creature/ , [cited 11/03/2017].

[Weis-Fogh, 1973]
Weis-Fogh, T. (1973). Quick estimates of flight fitness in hovering animals, including novel mechanisms for lift production. Journal of experimental Biology, 59(1), 169-230.

[Whitney & Wood, 2010]
Whitney, J. P., & Wood, R. J. (2010). Aeromechanics of passive rotation in flapping flight. Journal of Fluid Mechanics, 660, 197-220.

[Wood et al, 2003]
Wood, R. J., Avadhanula, S., Menon, M., & Fearing, R. S. (2003, September). Microrobotics using composite materials: The micromechanical flying insect thorax. In Robotics and Automation, 2003. Proceedings. ICRA'03. IEEE International Conference on (Vol. 2, pp. 1842-1849). IEEE.

[Wu et al, 2009]
Wu, P., Stanford, B., Bowman, W., Schwartz, A., & Ifju, P. (2009).

[Yan et al, 2001]

Yan, J., Wood, R. J., Avadhanula, S., Sitti, M., & Fearing, R. S. (2001). Towards flapping wing control for a micromechanical flying insect. In Robotics and Automation, 2001. Proceedings 2001 ICRA. IEEE International Conference on (Vol. 4, pp. 3901-3908). IEEE.

[Yang et al, 2009]
Yang, L. J., Hsu, C. K., Hsiao, F. Y., Feng, C. K., & Shen, Y. K. (2009, January). A micro-aerial-vehicle (MAV) with figure-of-eight flapping induced by flexible wing frames. In 47th AIAA Aerospace Sciences Meeting including The New Horizons Forum and Aerospace Exposition (p. 875).

[Zdunich et al, 2007]
Zdunich, P., Bilyk, D., MacMaster, M., Loewen, D., DeLaurier, J., Kornbluh, R., ... & Holeman, D. (2007). Development and testing of the mentor flapping-wing micro air vehicle. Journal of Aircraft, 44(5), 1701-1711.

[Zelazny, 1980]
Roger Zelazny, Changeling. Ace Books, 1980.

[Zhang et al, 2013]
Zhang, J., Cheng, B., Roll, J. A., Deng, X., & Yao, B. (2013, May). Direct drive of flapping wings under resonance with instantaneous wing trajectory control. In Robotics and Automation (ICRA), 2013 IEEE International Conference on (pp. 4029-4034). IEEE.

9 PUBLICATIONS

[Leys et al, 2015]
Leys, F., Vandepitte, D., & Reynaerts, D. (2015, December). Design of a flapping wing micro air vehicle, based on the Rufous Hummingbird. In Robotics and Biomimetics (ROBIO), 2015 IEEE International Conference on (pp. 1266-1271). IEEE.

[Leys et al, 2016]
Leys, F., Reynaerts, D., & Vandepitte, D. (2016). Outperforming hummingbirds' load-lifting capability with a lightweight hummingbird-like flapping-wing mechanism. Biology Open, 5(8), 1052-1060.

[Leys et al, 2016B]
Leys, Frederik, Dirk Vandepitte, and Dominiek Reynaerts. "Resonance supported reduction of peak actuator torques on a flapping wing driveline" ISMA proceedings. International Conference on Noise and Vibration Engineering. Leuven, Belgium, September 2016

[Timmermans et al., 2017]
Siemen Timmermans, Frederik Leys, Dirk Vandepitte. "Model-Based Evaluation of Control Roll, Pitch and Yaw Moments for a Robotic Hummingbird" AIAA Journal of Guidance, Control and Dynamics

[Leys et al, 2017]
Frederik Leys, Maarten Vanierschot, Julien Meert, Pieter-Jan Note, Eric Van den Bulck, and Dirk Vandepitte "Force and flow analysis of a high-frequency, high-amplitude flapping wing" AIAA Journal

Status: in review

10 APPENDIX: THE STROKE-CAM MECHANISM

The first version of the drive mechanism, as it was developed in the timeframe 2011-2013.Reciprocal motions like the hummingbird's wing motion are often generated by four-bar linkage mechanisms. These mechanisms however are unable to generate the large stroke amplitude required by the hummingbird's wing motion.

Another challenge in developing a lightweight hummingbird-like flapping mechanism is the high flapping frequency that is required, which demands low inertia of all accelerating parts and minimum friction losses in all articulations.

At the start of this research in 2010 none of the flapping mechanisms listed in Table 1 were published. The stroke-cam mechanism described below was the first flapping mechanism that was able to lift its own weight by generating a hummingbird-like wing motion with both a large stroke amplitude (up to 180°) and a high flapping frequency (up to 42Hz).

10.1 THE DESIGN

The stroke-cam mechanism (illustrated in Fig. 86) **[Leys, 2015]** converts the motion of a rotating axis of a small electric motor to the reciprocating stroke motion of a wing. The stroke-cam mechanism consists of a stroke-cam (red) which rotates around C, two cables (green) which are fixed at both extreme ends and which slip over the stroke cam and a wing wheel (black) which rotates around its centre. At one side of the stroke cam the cables are fixed at points F1 and F2 and on the other side of the stroke cam the cables are guided through openings G1 and G2 and fixed to the wing wheel. The wings are attached to this wing wheel by means of a joint which allows for the wing rotation. The cables are pre-tensioned. When the stroke cam rotates around C it moves the cables in such a way that they pull alternatingly at the wing wheel resulting in the stroke motion of the wing. The cables are pre-tensioned such that compressive forces can be transmitted during the whole flapping cycle.

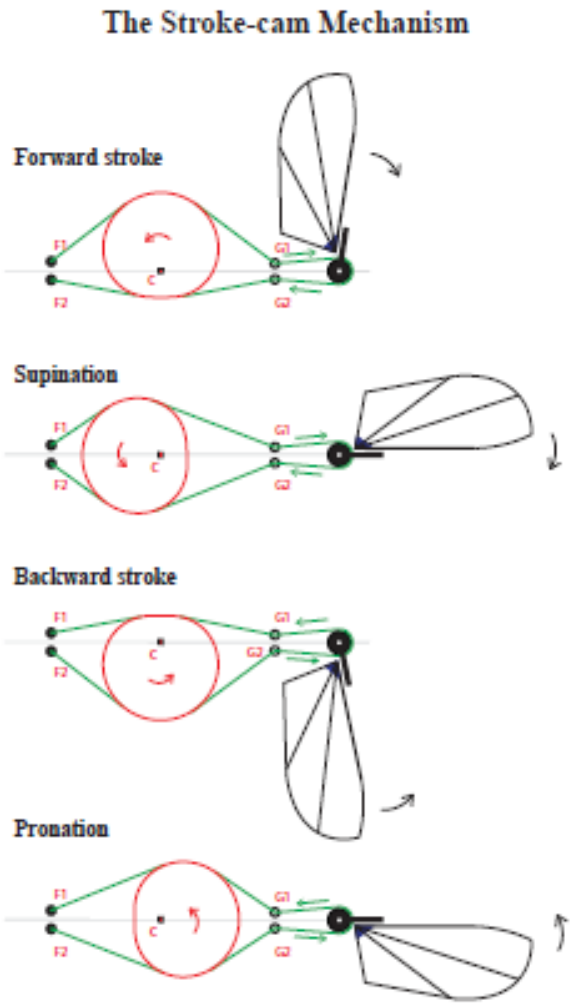

Fig. 86 The stroke-cam flapping mechanism: the stroke-cam (red) rotates around C and it pushes the cables (green) in such a way that they pull at the wing wheel (black) in an alternating way, resulting in the stroke motion of the wing.

Both the shape of the stroke-cam and the relative coordinates of F1, F2, G1 and G2 with respect to C have an influence on the course of stroke. The detailed description of these parameters can be found in **[Leys, 2015]**.

The stroke-cam mechanism generates a stroke motion that closely approximates a harmonic evolution of the stroke angle θ with time. Theoretically the course of the stroke

is symmetric. However, as shown by Fig. 86, during backward stroke and supination the cables move in the same direction as the stroke cam whereas during forward stroke and pronation the cables move in the opposite direction of the stroke cam resulting in a variation in friction between cables and stroke cam which may theoretically result in a slightly asymmetric driving effect on the wing wheel. Measurements on the mechanism indeed reveal some degree of asymmetry. The stroke amplitude generated with the stroke-cam mechanism is proportional to the radius of the wing wheel. This mechanism drives one degree of freedom, the stroke angle θ.

The second degree of freedom is the inclination angle, which is not actively controlled. The wing is attached to the wing wheel by means of a rotational joint. This enables the wing to pitch passively around its leading edge under the influence of the aerodynamic forces acting on the wing and the inertia of the wing. To obtain a desired inclination angle during forward and backward stroke we constrain the rotation motion with two pitch blocking elements (black), shown in Fig. 87. The advantage of this concept is its simplicity, the disadvantage is that the instant of time when rotation takes place cannot be controlled. Precise repetitivity of wing motion is not guaranteed.

10.2 VARYING THE KINEMATIC PARAMETERS

The kinematic parameters that can be modified to alter the flapping motion are the flapping frequency, stroke amplitude and the pitch angle during forward and backward stroke. The flapping frequency can be continuously varied during operation by changing the input voltage to the motor. Changing the flapping amplitude requires the replacement of the stroke cam with one of a different size. A modification of the maximum inclination angle during forward and backward stroke requires a new position for the pitching blocking elements.

10.3 PRACTICAL IMPLEMENTATION

Fig. 87 shows the practical implementation of the stroke-cam mechanism. The flapping mechanism is driven by a coreless brushed DC motor with a diameter of 6mm through a 3 gear transmission with a total gear ratio of 14.75. The stroke cam material is ABS and it is printed with an SST 1200ES printer. Nylon cables have a diameter of 0.1 mm. The tension in the cable can be adjusted with two small screws. The frame is assembled from several elements cut out of a 0.5mm carbon composite plate which are consecutively glued together. The total mass of this setup is 3.39g of which the wing constitutes 0.048g and the motor constitutes 1.64g.

Fig. 1.

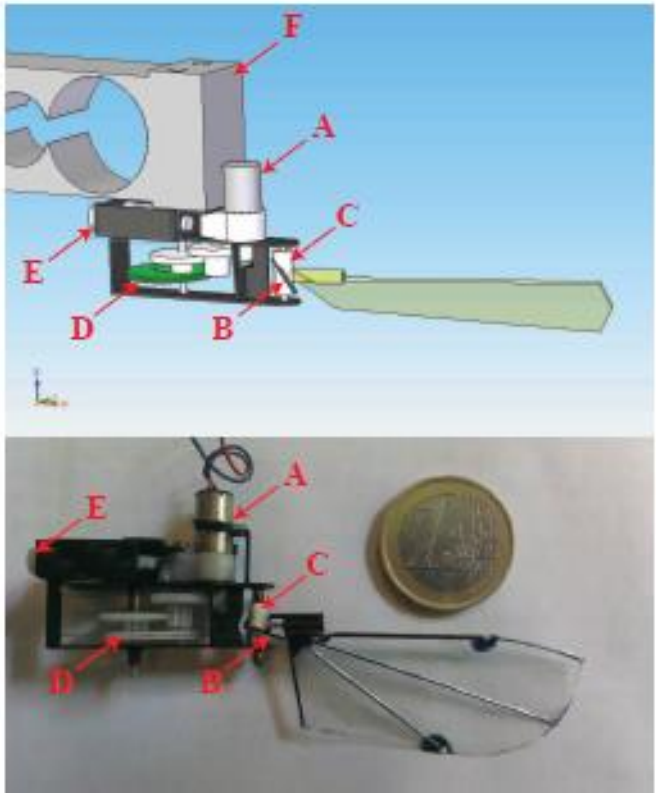

Fig. 87 The practical implementation of the stroke-cam flapping mechanism: DC motor (A), pitch blocking elements (B): black rods mounted on the wing wheel (C), stroke-cam (D), screws to adjust tension in the cable and a type 1668S load cell from BCM (F)

10.4 Abandoning the stroke-cam mechanism

After three years of experiments and improvements to the stroke-cam concept it was decided not to elaborate the stroke-cam mechanism any further and to replace it with a resonance supported mechanism. The stroke-cam mechanism has some shortcomings that make it difficult to implement it successfully in a robotic hummingbird:

- The stroke-cam flapping mechanism is too fragile. Due to friction, the cable brakes after about 5 minutes of flapping and it is difficult to replace.

- The stroke amplitude is not sufficiently predictable. A small change in the tension of the cable has a significant influence on the stroke amplitude.
- The generation of asymmetric wing motions in order to enable flight manoeuvers and maintain stability during flight would demand the addition of several extra actuators and other mechanical components, making the design considerably more complex and fragile.
- The concept of resonance support cannot be implemented with the stroke-cam driven flapping mechanism.